Dissertation

submitted to the
Combined Faculty of Natural Sciences and Mathematics
of Heidelberg University, Germany
for the degree of
Doctor of Natural Sciences

Put forward by
Paul Birk, MSc.
born in Odinzovo (Russia)

Oral examination: December 9th, 2020

The Dipole Response of an Ionization Threshold within Ultrashort and Strong Fields

Referees: **Prof. Dr. Thomas Pfeifer**
Prof. Dr. Selim Jochim

Die Dipolantwort einer Ionisationsschwelle innerhalb von ultrakurzen und starken Feldern – In dieser Arbeit wird die starkfeld-modifizierte Dipolantwort an der Ionisationsschwelle von Helium untersucht. Die Dipolantwort wird durch einen Attosekundenpuls im extrem ultravioletten Spektralbereich induziert und durch einen ultrakurzen und starken Femtosekundenpuls im nahen Infrarot manipuliert. Um diese Dipolantwort zu untersuchen, wird das transiente Absorptionsspektrum von Helium für unterschiedliche Zeitverzögerungen zwischen beiden Pulsen und unterschiedlichen Intensitäten des Femtosekundenpulses aufgenommen. Aus den Spektren wird die Dipolantwort an der Ionisationsschwelle rekonstruiert, die auf die Dynamik angeregter Elektronen mit Energien im Übergangsbereich von gebundenen zu freien Zuständen zurückzuführen ist. Um die zugrundeliegenden Prozesse der Wechselwirkung zwischen Licht und Materie zu identifizieren, die zu den beobachteten Strukturen im Zeit- und Spektralbereich führen, werden verschiedene quantenmechanische Modellsimulationen durchgeführt. Als Ergebnis offenbart die gemessene Dipolantwort lichtinduzierte Energieverschiebungen der kinetischen Energie eines Photoelektrons in der Nähe des Ions, Signaturen für feldgetriebene Rekollisionen des Photoelektrons in das Ion sowie einen zeitlichen Amplituden- und Phasensteuermechanismus. Mit letzterem wird die Aufbaudynamik von komplexen Spektralstrukturen aufgelöst. Diese sind die zeitabhängige Trennung und Linienformmodifikation der doppelt angeregten Rydberg-Serie und der zeitliche Aufbau der Ionisationsschwelle.

The Dipole Response of an Ionization Threshold within Ultrashort and Strong Fields – In this work, the strong-field-modified dipole response at the ionization threshold of helium is studied. The dipole response is induced by an attosecond pulse in the extreme ultraviolet spectral range and is manipulated by an ultrashort and strong femtosecond pulse in the near-infrared. To probe the response, the transient absorption spectrum of helium is recorded for different time delays between both pulses and different intensities of the femtosecond pulse. From the spectra, the dipole response of the ionization threshold is reconstructed, which is linked to the dynamics of excited electrons with energies in the transition region from bound to free. To identify the underlying processes of light-matter interaction leading to the observed structures in the time and spectral domain, different quantum-mechanical model simulations are conducted. As a result, the measured dipole response reveals light-induced energy shifts of the photoelectron's kinetic energy close to the parent ion, signatures for field-driven recollisions of a photoelectron into the parent ion, and a temporal amplitude and phase gating mechanism. With the latter, the build-up dynamics of complex spectral structures are temporally resolved, which are the time-dependent separation and line-shape modification of the doubly excited Rydberg series as well as the temporal build-up of the ionization threshold.

List of Publications

Parts of this work have been published in the following references:

P. Birk, V. Stooß, M. Hartmann, G. D. Borisova, A. Blättermann, T. Heldt, K. Bartschat, C. Ott, and T. Pfeifer
Attosecond transient absorption of a continuum threshold
J. Phys. B: At. Mol. Opt. Phys. **53**, 124002 (2020).
(For additional information see [1])

V. Stooß*, P. Birk*, A. Blättermann, M. Hartmann , G. D. Borisova , C. Ott, and T. Pfeifer
Strong-field-gated buildup of a Rydberg series
Phys. Rev. Res. **2**, 032041(R) (2020)
(*These authors contributed equally to this work. For additional information see [2])

Further publications with own contributions:

T. Ding, C. Ott, A. Kaldun, A. Blättermann, K. Meyer, V. Stooß, M. Rebholz, P. Birk, M. Hartmann, A. Brown, H. Van Der Hart, and T. Pfeifer
Time-resolved four-wave-mixing spectroscopy for inner-valence transitions
Opt. Lett. **41**, 709-712 (2016)

V. Stooß, S. M. Cavaletto, S. Donsa, A. Blättermann, P. Birk, C. H. Keitel, I. Březinová, J. Burgdörfer, C. Ott, and T. Pfeifer
Real-Time Reconstruction of the Strong-Field-Driven Dipole Response
Phys. Rev. Lett. **121**, 173005 (2018)

V. Stooß, M. Hartmann, P. Birk, G. D. Borisova, T. Ding, A. Blättermann, C. Ott, and T. Pfeifer
XUV-beamline for attosecond transient absorption measurements featuring a broadband common beam-path time-delay unit and in situ reference spectrometer for high stability and sensitivity
Rev. Sci. Instrum. **90**, 053108 (2019)

C. Ott, L. Aufleger, T. Ding, M. Rebholz, A. Magunia, M. Hartmann ,V. Stooß, D. Wachs, P. Birk, G. D. Borisova, K. Meyer, P. Rupprecht, C. da Costa Castanheira, R. Moshammer, A. R. Attar, T. Gaumnitz , Z. Loh, S. Düsterer, R. Treusch , J. Ullrich, Y. Jiang , M. Meyer, P. Lambropoulos, and T. Pfeifer
Strong-Field Extreme-Ultraviolet Dressing of Atomic Double Excitation
Phys. Rev. Lett. **123**, 163201 (2019)

M. Hartmann, V. Stooß, P. Birk, G. D. Borisova, C. Ott, and T. Pfeifer
Attosecond precision in delay measurements using transient absorption spectroscopy
Opt. Lett. **44**, 4749-4752 (2019)

T. Ding, M. Rebholz, L. Aufleger, M. Hartmann, K. Meyer,V. Stooß, A. Magunia, D. Wachs, P. Birk, Y. Mi, G. D. Borisova, C. da Costa Castanheira, P. Rupprecht, Z. Loh, A. R. Attar, T. Gaumnitz, S. Roling, M. Butz, H. Zacharias, S. Düsterer, R. Treusch, S. M. Cavaletto, C. Ott, and T. Pfeifer
Nonlinear Coherence Effects in Transient-Absorption Ion Spectroscopy with Stochastic Extreme-Ultraviolet Free-Electron Laser Pulses
Phys. Rev. Lett. **123**, 103001 (2019)

G. D. Borisova, V. Stooß, A. Dingeldey, A. Kaldun, T. Ding, P. Birk, M. Hartmann, T. Heldt, C. Ott, and T. Pfeifer
Strong-field-induced single and double ionization dynamics from single and double excitations in a two-electron atom
J. Phys. Commun. **4,** 055012 (2020)

M. Rebholz, T. Ding, V. Despré, L. Aufleger, M. Hartmann, K. Meyer, V. Stooß, A. Magunia, D. Wachs, P. Birk, Y. Mi, G. D. Borisova, C. da Costa Castanheira, P. Rupprecht, G. Schmid, K. Schnorr, C. D. Schröter, R. Moshammer, Z. Loh, A. R. Attar, S. R. Leone, T. Gaumnitz, H. J. Wörner, S. Roling, M. Butz, H. Zacharias, S. Düsterer, R. Treusch, G. Brenner, J. Vester, A. I. Kuleff, C. Ott, and T. Pfeifer
All-XUV pump-probe transient absorption spectroscopy of the structural molecular dynamics of diiodomethane
submitted to Phys. Rev. X (2020)

T. Ding, M. Rebholz, L. Aufleger, M. Hartmann, V. Stooß, A. Magunia, P. Birk, G. D. Borisova, D. Wachs, K. Meyer, C. da Costa Castanheira, P. Rupprecht, Y. Mi, A. R. Attar, T. Gaumnitz, Z. Loh, S. Roling, M. Butz, H. Zacharias, S. Düsterer, R. Treusch, S. M. Cavaletto, C. Ott, and T. Pfeifer
Measuring the frequency chirp of extreme-ultraviolet free-electron laser pulses by transient absorption spectroscopy
submitted to Nat. Commun. (2020)

T. Ding, M. Rebholz, L. Aufleger, M. Hartmann, V. Stooß, A. Magunia, P. Birk, G. D. Borisova, D. Wachs, C. da Costa Castanheira, P. Rupprecht, Y. Mi, A. R. Attar, T. Gaumnitz, Z. Loh, S. Roling, M. Butz, H. Zacharias, S. Düsterer, R. Treusch, C. Ott, and T. Pfeifer
XUV-pump XUV-probe transient absorption spectroscopy at FELs
submitted to Faraday Discuss. (2021)

Contents

1. Introduction

What happens with the constituents of an atom or a molecule during a chemical reaction? How do electrons or nuclei within a molecule rearrange in time when a molecular bond breaks, forms, or a molecular configuration changes? These questions motivate many physicists to study the dynamics of atoms and molecules in a time-resolved manner [3,4]. Here, one ultimate objective of this field is to track in time and space the trajectories of electrons and nuclei during molecular dynamics and, in addition to that, to even control the dynamics in order to, for instance, favor certain chemical reactions. To resolve in time dynamics happening in nature, one needs tools that occur on the same timescale or even shorter. An example to illustrate this is given by looking at the wing beat of a hummingbird. This movement cannot be time-resolved by the naked human eye since the hummingbird moves its wings with a frequency of up to 50 beats per second [5]. In contrast, the visual perception of a human only starts to detect visual gaps in movements at this frequency [6]. The wing beat thus appears as a blurred movement. Only with cameras that have an exposure time shorter than the period of the wing beat it is possible to revolve in time the trajectory of the wings.

The hummingbird wing beat is a macroscopic example, while the physics of atoms and molecules takes place at the microscopic scale. Their dynamics obey the laws of quantum mechanics, where the properties of atoms or molecules can be described by their quantized states. By putting energy in or taking energy from an atomic or molecular quantum system, its state can change, or the system ends up in a superposition of quantum states, which is a common phenomenon in quantum mechanics. This superposition principle results in the formation of so-called wave packets, which exhibit an evolution in time. The timescale of these dynamics is governed by the inverse of the energy differences of the wave packet's energy states. In the case of molecules, typical energy differences are on the order of several meV (1 electronvolt $\approx 1.6 \times 10^{-19}$ Joule), leading to timescales of picoseconds (10^{-12} s) down to femtoseconds (10^{-15} s). Typical energy differences in atoms are on the order of several eV, which corresponds to evolution times reaching the attosecond (10^{-18} s) timescale. Compared to everyday life, this is an incredibly short scale. To classify it, one should note that the age of the universe is ~13.8 Gyr, which is ~4.35×10^{17} s [7]. Thus, the relation between a second and the age of the universe is similar to the relation between the evolution time of an electron wave packet within an atom and a second.

Aside from the short timescale of its dynamics, the atom is also small. The typical length scale involved here is the Bohr radius. This is the mean distance between the

electron and the nucleus in the hydrogen atom in its ground state, and it amounts to ~0.53 Å (1 Å = 10^{-10} m). Thus, the experiments with which one wants to probe the dynamics of atoms or molecules have to make use of processes that are short in time and additionally are sensitive to small length changes. With the advent of ultrashort laser pulses, it became possible to perform experiments that fulfill these requirements. Typically such pulses are illuminated onto and interact with the target material under study. By measuring, e.g., the properties of the material after laser illumination, the fragments after its laser-induced destruction, or the properties of the laser pulses like their spectra before and after hitting the target, one can reconstruct the dynamics in the material that is induced by the light-matter interaction. Furthermore, using an interferometric geometry, one can probe the dynamics in a time-resolved manner via a pump-probe scheme. Here, one laser pulse pumps, for instance, an atom into a desired state, inducing electron dynamics, and a time-delayed laser pulse subsequently probes the state. The time resolution is then achieved by precisely controlling the delay between the two pulses. An additional advantage of an interferometric experiment is its high sensitivity to length differences. As an impressive recent example, such experiments can be sensitive enough to observe space-time changes generated by gravitational waves, which result from the merger of black holes that are about a billion light-years (1 ly ≈ 9.46×10^{15} m) away [8].

Using femtosecond pulses in pump-probe types of experiments, one can resolve in time and space chemical reactions with sub-angstrom resolution [9]. The production of femtosecond pulses became possible with the invention of mode-locking, together with the Kerr-lensing technique [10,11]. Over the last decades, many advances to further shorten the laser pulse duration and increase the peak intensity were made. Nowadays, such pulses are routinely available with durations that support only a few cycles of the carrier electromagnetic wave and intensities excessing ~10^{14} W/cm^2 [12–15]. The duration of laser pulses was further reduced with the generation of high harmonics of these ultrashort laser pulses [16,17]. Using this technique, it became possible to generate pulse trains or isolated pulses on the attosecond time scale [18,19]. These pulses are, to date, the shortest controllable tools (the current record of pulse duration is 43 as [20]) that are used to perform time-resolved measurements on the natural timescale of electronic excitations in atomic [21–24], molecular [25–27] and solid-state systems [28].

One of the fundamental light-matter interactions is the transfer of energy from the light field into the atom or molecule via the absorption of photons. This happens at laser frequencies (or photon energies) that are characteristic for the target and results in absorption lines, i.e., spectral gaps that are observable in the frequency spectrum of the light field. The absorption spectra for different target materials have been extensively studied throughout the last two centuries from its first systematic observation in the pioneering work by Fraunhofer [29], the identification of new elements by the development of the spectroscopy technique by Kirchhoff and Bunsen

[30], to a recent measurement of the time-resolved build-up of an absorption line shape [31]. In the latter, the absorption spectrum of an attosecond pulse through a helium target was measured in the presence of another ultrashort, strong, and time-delayed laser pulse, which transiently changes the absorption. In order to interpret the experimental results, one has to realize that the appearance of absorption lines is, in first order, the result of the destructive (or constructive) interference of the incoming light field with the light-induced time-dependent dipole response of the material [32–34]. In the experiment, the additional strong laser pulse temporally gates the evolution of the dipole response in the time domain and thereby changes the emergence of the interference resulting in the build-up of the absorption line. With this understanding of the origin and the modification mechanism of absorption, it becomes possible to control the line shape of absorption resonances such that naturally symmetric line shapes become asymmetric and vice versa [35], or even to turn absorption into gain using nuclear resonances in the x-ray spectral region [36].

All these mentioned experiments were focused on the observation or modification of the absorption of resonant atomic, molecular, or nuclear transitions. However, a non-resonant absorption spectrum resulting from a transition to a continuous energy state also has a certain spectral shape, which can be observed and modified. In the atomic or molecular case, non-resonant absorption is given by the photoionization of electrons from the atom or the molecule. For solid-state systems, it can be the transition from an occupied to an unoccupied energy band. Both cases have in common that the absorption increases at a certain photon energy threshold. Due to this threshold, the spectral absorption shape of a non-resonant transition is asymmetric. It is low below the threshold, increases typically step-like across the threshold, and is flat above the threshold. Similar to the interpretation for the origin of the resonant spectral line shapes, an absorption threshold results from the interference of an induced time-dependent dipole response of the material and the incident light. This thesis aims to study the dipole response of an ionization threshold and modify it in a controlled time-resolved manner using an ultrashort and strong laser pulse.

For this purpose, attosecond transient absorption spectroscopy (ATAS) is performed on the first and second ionization threshold of the prototype spectroscopy target helium. In ATAS, an attosecond pulse in the extreme ultraviolet (XUV) spectral range is produced by means of high harmonic generation of a near-infrared (NIR) femtosecond laser pulse. Both pulses are focused onto a gas cloud (here helium) with a controlled time-delay between the pulses, and the laser-modified XUV transmission spectrum of the attosecond pulse is recorded by a high-resolution XUV spectrometer. In the second chapter of this thesis, the theoretical framework will be given, allowing one to understand the underlying physics in this type of experiment. In the following chapters, the experimental setup to perform ATAS and the data processing and calibration steps are described. The transient absorption spectrum of

the first ionization threshold in helium will be presented in the fifth chapter. Here the laser-induced effects visible in the absorption will be interpreted by comparing them with results from a quantum mechanical model simulation. As will be further pointed out over the course of this thesis, the absorption spectrum at the ionization threshold is generated by the dipole response of slow photoelectrons in the vicinity of the residual ion. Therefore, with the interferometric method of ATAS, one can locally probe these slow electrons within the non-negligible Coulomb potential of the ion. In the sixth chapter, the above-mentioned response-gating mechanism by a strong laser pulse is investigated and applied onto the first ionization threshold and the doubly excited Rydberg resonance, converging to the second ionization threshold of helium. Finally, the results of this thesis are summarized and concluded, and an outlook for future studies will be provided.

2. Fundamentals

In order to understand and interpret the physical processes during the interaction of ultrashort and strong laser pulses with matter, one first needs to know the underlying fundamental concepts and their mathematical descriptions. Since the research field of attosecond science is multifaceted and even intersects many other disciplines, a comprehensive overview cannot be given in the scope of this thesis. Therefore, this chapter focuses on the definitions, the physical laws, and derivations used to describe the physics of light-matter interaction studied in this thesis. For the sake of clarity, many also interesting phenomena in attosecond science are omitted, but the interested reader can find further details aside from this chapter, for instance, in references [37–41].

In this thesis, the light-matter interaction between pulsed laser fields and the helium atom is studied. For its mathematical treatment, the semi-classical approach is well-established. Here, the laser fields are described classically by using the well-known Maxwell equations, and the atoms are treated fully quantum mechanically by atomic states and the transitions between these states. Since the spatial dimension of the helium atom is much smaller ($\sim 10^{-10}$ m) than all here treated wavelengths of the field (down to $\sim 10^{-8}$ m), the spatial dependency of the fields can be neglected; or, considering a macroscopic target, all studied interactions are confined within the Rayleigh range, and thus it is sufficient to consider only the propagation direction of the fields. With this spatial independence in the light-matter interaction, the electric dipole approximation can be applied, which is a central approximation of the presented work. With this, the interaction Hamiltonian between the laser and the atoms will be purely given by the electric dipole operator times the electric field. Furthermore, the used laser field strength is such that the non-relativistic equations of motion are applicable.

The chapter starts with the definitions and the properties of ultrashort and strong laser pulses. Then the quantum dynamics of an atomic system are described together with its perturbative and non-perturbative interaction with laser pulses. Here, in particular, the electric dipole response of the atom is the key observable to probe the dynamics in the spectral and in the time domain. At the end of this chapter, the properties of the helium atom are introduced as a benchmark system with two correlated electrons, and the production of attosecond pulses via high harmonic generation is outlined, which are used to investigate this two-electron system.

Ultrashort Laser Pulses

Laser pulses are coherent electromagnetic fields that are concentrated in space and nonzero only for a short time. Their dynamics are mathematically well described by Maxwell's equations using time- and space-dependent electric field and magnetic field vectors. From Maxwell's equations, one can arrive at the wave equation describing the propagation of the field vectors as electromagnetic waves in time and space. In general, the solution of this equation can become very complex, but one can often make some valid approximations to simplify the treatment. Here, the electric dipole approximation is made, which allows one only to consider the electric fields. The magnetic field vanishes since the vector potential $\vec{A}$ which generates the magnetic field $\vec{B}$ via $\vec{B} = \vec{\nabla} \times \vec{A}$ is independent of space in this approximation.

It is mathematically convenient to use a complex-valued representation, whereby the real part gives the physical fields. With this, the laser pulse's time-dependent electric field vector at a certain point in space can be written as

$$\vec{F}(t) = \vec{\epsilon}(t) f(t)\, e^{-i\phi(t)}. \qquad (2.1)$$

Here, $f(t)$ is the time-dependent slowly varying envelope, $\vec{\epsilon}(t)$ is the unit vector representing the time-dependent polarization and $\phi(t)$ is the time-dependent phase, which represents the fast oscillation of the carrier wave. Most electric fields considered here are linearly polarized, and thus in the polarization-unit-vector, one element is unity, and the others are zero. Therefore the vector notation is omitted, and scalars are used in the following unless stated otherwise.

The envelope can, in general, have an arbitrary shape in time, but a good estimation is often a Gaussian function given by

$$f_{\mathrm{Gauss}}(t) = f_0 e^{-2\ln(2)\left(\frac{t}{\tau_{\mathrm{FWHM}}}\right)^2}, \qquad (2.2)$$

where f_0 is the peak field amplitude and τ_{FWHM} is the characteristic pulse duration known as the full width at half maximum (FWHM) of the peak intensity of the pulse. Further commonly used pulse envelopes are the squared hyperbolic secant (sech) function

$$f_{\mathrm{sech}}(t) = f_0 \,\mathrm{sech}^2\left(\frac{t}{\tau_{\mathrm{sech}}}\right) = f_0 \cosh^{-2}\left(\frac{t}{\tau_{\mathrm{sech}}}\right), \qquad (2.3)$$

where $\tau_{\mathrm{FWHM}} \approx 1.76 \cdot \tau_{\mathrm{sech}}$, or the squared cosine function

$$f_{\cos}(t) = \begin{cases} f_0 \cos^2\left(\frac{t}{\tau_{\cos}}\right) & \text{for } -\frac{\pi}{2}\tau_{\cos} \le t \le \frac{\pi}{2}\tau_{\cos} \\ 0 & \text{otherwise} \end{cases} \qquad (2.4)$$

with

$$\tau_{\cos} = \frac{\tau_{\mathrm{FWHM}}}{2\arccos(2^{-1/4})}. \qquad (2.5)$$

With a detector, the intensity of the fields is commonly measured rather than their amplitudes. It is given by the absolute square of the field

$$I(t) = \frac{1}{2}\,\varepsilon_0 c\,|F(t)|^2, \tag{2.6}$$

where ε_0 is the electric vacuum permittivity and c the speed of light. Thus, the field intensity depends on time, and in the case of the Gaussian field envelope, it reads:

$$I(t) = I_{\mathrm{peak}} e^{-4\ln(2)\left(\frac{t}{\tau_{\mathrm{FWHM}}}\right)^2} \tag{2.7}$$

with the peak intensity

$$I_{\mathrm{peak}} = \frac{1}{2}\,\varepsilon_0 c f_0^2. \tag{2.8}$$

In order to measure the peak intensity of a laser pulse, one has to consider that the laser pulse always has a spatial beam profile, which is the intensity across the transverse section of the laser beam. It can often be approximated by a Gaussian beam profile with beam waist w. With this, the peak intensity can be related to the pulse energy ε via

$$I_{\mathrm{peak}} = \frac{1.88}{\pi}\frac{\varepsilon}{\tau_{\mathrm{FWHM}} w^2}. \tag{2.9}$$

The pulse energy is the experimentally measurable averaged power of the laser P divided by the repetition rate of the laser pulses f_{rep}

$$\varepsilon = P/f_{\mathrm{rep}}. \tag{2.10}$$

The time-dependent phase $\phi(t)$ in equation 2.1 is expandable in terms of a power series

$$\phi(t) = \phi_{\mathrm{CEP}} + \omega_c t + a t^2 + b t^3 + \cdots \tag{2.11}$$

The first term is the so-called carrier-envelope phase (CEP). That is the offset between the maximum of the carrier wave and the pulse envelope. The parameter ω_{c} in the linear term is the central frequency of the carrier, and a and b represent the linear and quadratic chirp. Figure 2.1 depicts the electric field of the pulse for different parameter values. As shown here, for pulses with only a few field cycles, the CEP determines the waveform and, in particular, the maximum field amplitude. The influence of the chirp term can be readily revealed by defining the instantaneous frequency

$$\omega(t) = \frac{d\phi(t)}{dt} = \omega_c + 2at + 3bt^2 + \cdots \tag{2.12}$$

This equation states that if the chirp parameters, i.e., a or b or higher orders, are positive, the frequency will increase over time, and if they are negative, the frequency will decrease, as shown in figure 2.1. The pulse is accordingly called up- or down-chirped, respectively.

The description of the pulses so far is given in the time domain, but it can be transformed into an equivalent description in the frequency domain, also called the spectral domain, using the Fourier transformation

$$\tilde{F}(\omega) = \mathcal{F}[F(t)] = \frac{1}{\sqrt{2\pi}} \int_{-\infty}^{+\infty} F(t) e^{i\omega t} dt. \qquad (2.13)$$

The backward transformation is accordingly

$$F(t) = \mathcal{F}^{-1}[\tilde{F}(\omega)] = \frac{1}{\sqrt{2\pi}} \int_{-\infty}^{+\infty} \tilde{F}(\omega) e^{-i\omega t} d\omega. \qquad (2.14)$$

Here and in the following, the variables are indicated by a tilde if they are defined in the frequency domain unless the domain is clear. This relation between the time and the spectral domain states that the shorter the pulse in time, the broader it has to be in the spectral domain and vice versa. Thus, in order to generate an ultrashort pulse, it must consist of many different spectral components. This can also be understood in terms of the uncertainty principle given by

$$\Delta\omega \Delta t \geq \frac{1}{2}, \qquad (2.15)$$

where $\Delta\omega$ and Δt are the spectral bandwidth and pulse duration, respectively. Here the factor $1/2$ is only a lower bound, and this value depends on the exact temporal shape of the intensity.

According to the Fourier transformation, the phase in the spectral domain becomes

$$\tilde{\phi}(\omega) = \tilde{\phi}_{\mathrm{CEP}} + \tau_{\mathrm{GD}}(\omega - \omega_c) + \frac{\mathrm{GDD}}{2}(\omega - \omega_c)^2 + \frac{\mathrm{TOD}}{6}(\omega - \omega_c)^3 + \cdots \qquad (2.16)$$

Here the factor τ_{GD} in the term linear in ω describes the mean delay, which is the global temporal shift of all frequency components of the pulse. Similar to the instantaneous frequency, one can further define the group delay by taking the derivative of the spectral phase with respect to the frequency

$$\tilde{\tau}(\omega) = \frac{d\tilde{\phi}(\omega)}{d\omega} = \tau_{\mathrm{GD}} + \mathrm{GDD}(\omega - \omega_c) + \frac{\mathrm{TOD}}{2}(\omega - \omega_c)^2 + \cdots \qquad (2.17)$$

Here the factor for the linear term (quadratic in equation 2.16) is called the group delay dispersion (GDD) and for the quadratic term (cubic in equation 2.16) third-order dispersion (TOD). Equation 2.17 intuitively shows the impacts of the dispersion terms similar to equation 2.12. For non-vanishing dispersion, the group delay of the pulse becomes frequency-dependent. Figure 2.1 depicts the electric field for different values of dispersion. In the case of all chirp parameters being zero, subfigure b), e), and h), the pulse is called transform-limited. That means it has the shortest time duration supported by the spectral bandwidth and envelope shape. By changing the GDD, in subfigure d) and f), the pulse duration becomes longer, and the carrier

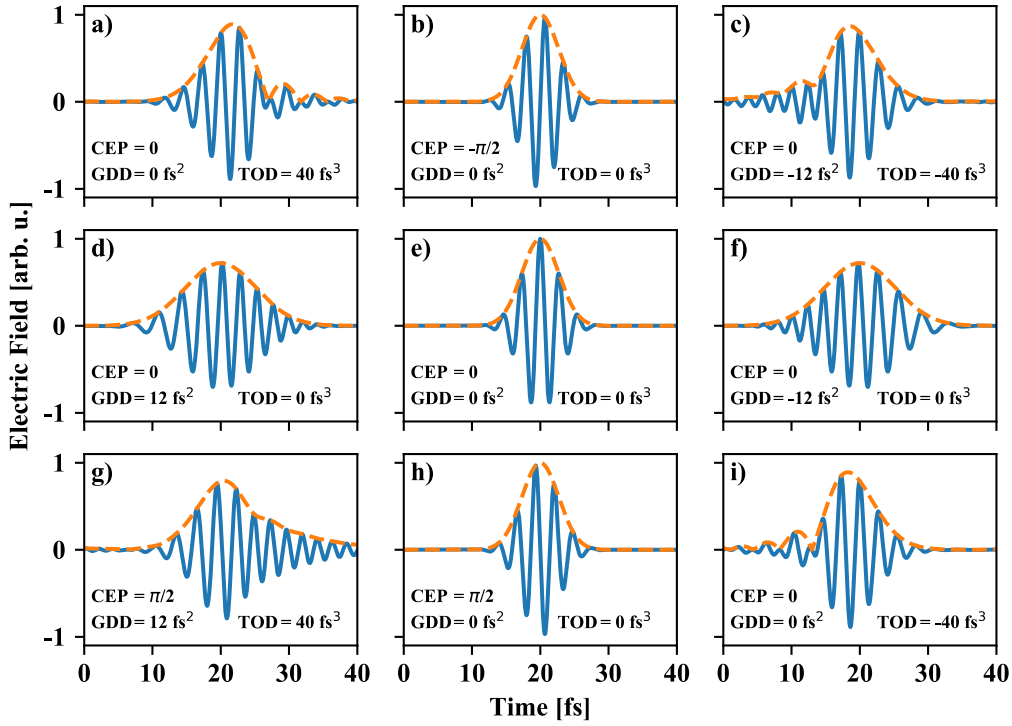

Figure 2.1: The pulse's electric field for different carrier-envelope phase (CEP), group delay dispersion (GDD) and third-order dispersion (TOD). The respective pulse envelope is depicted by a dashed orange line. The unchirped pulse in e) has a Gaussian shaped envelope with a pulse duration of 4.5 fs, and a central photon energy of 1.5 eV. These specifications are similar for the pulses used in the experiment. While the CEP changes the phase slippage between the carrier wave and the envelope, the GDD and TOD change the pulse duration and determine the existence of pre- or post-pulses. The definition of CEP, GDD, and TOD is given by equation 2.16.

frequency sweeps under the pulse envelope. Introducing a nonzero TOD, subfigure a) and i) pre- or post-pulses next to the main pulse appear. In combination with a nonzero GDD, the pulse exhibits a long tail at one side of the pulse; see subfigure c) and g).

Dispersions are accumulated in the pulse during its propagation through an optical material with length z. This can be described by the Helmholtz equation

$$\left[\frac{\partial^2}{\partial z^2} + k(\omega)^2\right]\tilde{F}(\omega, z) = 0, \qquad (2.18)$$

where $k(\omega)$ is the frequency-dependent wavenumber. The general solution to this equation is the z-dependent field

$$\tilde{F}(\omega, z) = \tilde{F}(\omega, 0)e^{ik(\omega)z}. \qquad (2.19)$$

The wavenumber is related to the frequency-dependent refractive index $n(\omega)$ of the material via

$$k(\omega) = \frac{\omega}{c}n(\omega). \qquad (2.20)$$

For most materials, the refractive index is not constant with respect to the field frequencies. Thus, they introduce a frequency-dependent phase shift onto the pulse. The connection to the dispersion mentioned above can be revealed by a Taylor expansion of the wavenumber around the pulse's central frequency ω_c

$$\begin{aligned} k(\omega) &= k_c + \left.\frac{dk(\omega)}{d\omega}\right|_{\omega_c} (\omega-\omega_c) + \frac{1}{2}\left.\frac{d^2k(\omega)}{d\omega^2}\right|_{\omega_c} (\omega-\omega_c)^2 + \cdots \\ &= \frac{\omega_c}{c} n(\omega_c) + \left[\frac{n(\omega_c)}{c} + \frac{\omega_c}{c}\left.\frac{\partial n(\omega)}{\partial \omega}\right|_{\omega_c}\right](\omega-\omega_c) \\ &+ \frac{1}{2}\left[\frac{2}{c}\left.\frac{\partial n(\omega)}{\partial \omega}\right|_{\omega_c} + \frac{\omega_c}{c}\left.\frac{\partial^2 n(\omega)}{\partial \omega^2}\right|_{\omega_c}\right](\omega-\omega_c)^2 + \cdots \end{aligned} \qquad (2.21)$$

The first-order coefficient in equation 2.21 is identified by the inverse of the group velocity evaluated at the central frequency. It is given by

$$v_{\mathrm{g}}(\omega) = \left(\frac{dk(\omega)}{d\omega}\right)^{-1} = \left(\frac{n(\omega)}{c} + \frac{\omega_c}{c}\frac{\partial n(\omega)}{\partial \omega}\right)^{-1}. \qquad (2.22)$$

The second-order coefficient is linked to the group velocity dispersion (GVD)

$$\mathrm{GVD}(\omega) = -\frac{1}{v_{\mathrm{g}}^2}\frac{\partial v_{\mathrm{g}}}{\partial \omega} = \frac{d^2k}{d\omega^2} = \left[\frac{2}{c}\frac{\partial n(\omega)}{\partial \omega} + \frac{\omega_c}{c}\frac{\partial^2 n(\omega)}{\partial \omega^2}\right]. \qquad (2.23)$$

Considering equation 2.16, one can finally relate the mean delay and the group delay dispersion with the material's refractive index using $\tilde{\phi}(\omega) = k(\omega)z$

$$\tau_{\mathrm{GD}} = \frac{1}{v_{\mathrm{g}}(\omega_c)}\, z, \qquad (2.24)$$

$$\mathrm{GDD} = \mathrm{GVD}(\omega_c)\, z. \qquad (2.25)$$

Thus, any optical material with a non-vanishing GVD, i.e., with a frequency-dependent refractive index, will add GDD to the spectral phase and thereby introduce a chirp onto the pulse, which leads to a modification of the pulse duration.

Furthermore, a non-constant refractive index results in a phase shift between the carrier of the field and the pulse envelope, i.e., a change in the CEP. Since the delay of the carrier is given by

$$\tau_c = \frac{z}{v_c} = \frac{n(\omega)}{c} z \qquad (2.26)$$

the phase slippage φ after propagation through the material will become

$$\varphi = \omega_c \Delta\tau = \omega_c(\tau_c - \tau_{\mathrm{GD}}) = -\frac{\omega_c^2}{c}\frac{\partial n(\omega)}{\partial \omega} z. \qquad (2.27)$$

Strong Laser Pulses

In the previous section, the duration and the dispersion of ultrashort laser pulses were introduced. The present section addresses the question: What is a strong laser pulse? The term “strong” is relative, and therefore it is good practice to compare the strength of the laser electric field with other field scales observed in nature. An example is the electric field strength $F(r)$ that an electron experiences in the vicinity of an atomic core at distance r. It can be derived from Coulomb's law and reads

$$F(r) = \frac{1}{4\pi\varepsilon_0}\frac{q}{r^2}, \qquad (2.28)$$

where q is the charge of the atomic core. In the case of a hydrogen atom, the most probable distance of a bound electron in the atomic ground state to the singly charged core is given by one Bohr radius $a_0 \approx 5.3{\cdot}10^{-11}$ m. With this, the field strength becomes

$$F_{\mathrm{H}}(r = a_0) = \frac{1}{4\pi\varepsilon_0}\frac{e}{a_0^2} \approx 5.14 \cdot 10^9 \frac{\mathrm{V}}{\mathrm{cm}}. \qquad (2.29)$$

Therewith, one can define a pulse to be strong if it has a field strength comparable to this Coulomb field. Using equation 2.8, this corresponds to a peak intensity of $I_{\mathrm{peak}} \approx 3.5 \cdot 10^{16}\,\mathrm{W/cm^2}$, which, from an experimental point of view, is a very high intensity, but it is needed to enter the strong-field regime for a hydrogen atom. However, in different atomic species, the outermost electron of the neutral atom feels lower Coulomb fields since first, it has a greater mean distance to the core, and second, the core’s charge is screened by the other electrons within the atom. Therefore, peak intensities of the pulses on the order of 10^{14}, 10^{13}, or even down to $10^{12}\,\mathrm{W/cm^2}$ can often be regarded as strong.

Another well-established method to define a strong field is the comparison of characteristic energies of the atom and the field. For the atom, one characteristic energy is the ionization energy or also called the ionization potential I_{p}. For the field, it is the so-called ponderomotive potential, which is derived as follows. If an electron is exposed to an electric field, it gets accelerated by the field, which can be described by the equation of motion

$$\frac{d^2}{dt^2}x(t) = -\frac{eF(t)}{m_{\mathrm{e}}}, \qquad (2.30)$$

where e is the elementary charge and m_{e} is the electron mass. In an ultrashort pulse, the field carrier oscillates around zero, and thus the solution of the trajectory of the electron will be a quivering motion. Due to this motion, the electron exhibits certain kinetic energy, which is transferred to the electron by the oscillating field. On average, this kinetic energy is not zero. This can be seen by calculating the electron’s time-dependent velocity $v_x(t)$. Using a plane wave to approximate the carrier of the

pulse with the field equation $F(t) = F_0 \cos(\omega_c t + \phi)$ equation 2.30 can be integrated analytically in time

$$v_x(t) = \int_0^t \frac{d^2}{dt'^2} x(t)\, dt' = -\frac{eF_0}{m_e \omega_c} [\sin(\omega_c t + \phi) - \sin(\phi)]. \quad (2.31)$$

The first term of the velocity is oscillating in time, and the second term yields a constant drift of the electron. Its magnitude and direction depend on the initial phase ϕ of the field at $t = 0$. This is the time when the electron starts to experience the electric force due to, e.g., being ionized from an atom. Thus, the initial electric field phase determines the long-term trajectory of the electron.

With the time-dependent velocity at hand, one can readily show that the mean kinetic energy during one electric field cycle has a non-zero value

$$\begin{aligned} \langle E_{\text{kin}} \rangle &= \frac{m_e}{2} \langle v_x(t)^2 \rangle = \frac{m_e}{2} \left\langle \left[-\frac{eF_0}{m_e \omega_c} [\sin(\omega_c t + \phi) - \sin(\phi)] \right]^2 \right\rangle \\ &= \frac{e^2 F_0^2}{4 m_e \omega_c^2} \neq 0. \end{aligned} \quad (2.32)$$

Thus, on time-average, the electron gains energy added to the energy it would have without the oscillating field. Therewith the field acts for the electron as a potential, which is called the ponderomotive potential U_p. Using equation 2.8, one can further relate this potential to the peak intensity of the field

$$U_p = \langle E_{\text{kin}} \rangle = \frac{e^2}{2 m_e \varepsilon_0 c \omega_c^2} I_{\text{peak}} = \frac{e^2}{8\pi^2 m_e \varepsilon_0 c^3} \lambda_c^2 I_{\text{peak}}, \quad (2.33)$$

where λ_c is the central wavelength of the carrier field. Since U_p is proportional to the intensity and to the square of the wavelength, one can experimentally control this potential. Although only a free electron is considered in the derivation of the ponderomotive potential, it is also partly applicable to electrons bound to an atomic system. Here, the ponderomotive potential shifts the energy of the quantum state the electron occupies. This energy shift is small for deeply bound states, and it is almost equal to the ponderomotive energy if the electron is excited to a high-lying state, where it is only loosely bound.

Finally, the relation of the ionization potential and the ponderomotive potential defines the Keldysh parameter γ (named after Leonid V. Keldysh [42])

$$\gamma = \sqrt{\frac{I_p}{2U_p}}. \quad (2.34)$$

With this, an electric field can be defined as strong if the Keldysh parameter is small, i.e., if $\gamma < 1$ holds. On the other hand, if the parameter is large, i.e., $\gamma > 1$ or even $\gamma \gg 1$, the interaction of the field with a target under investigation can often be treated perturbatively. An example of a perturbative treatment is the laser-induced

single or multiphoton excitation or ionization of atoms, while an example of a non-perturbative treatment is tunnel ionization, which, in turn, is a prerequisite for the high harmonic generation that will be introduced below.

Quantum Dynamics

In this dissertation, the subject under study is the helium atom and its laser-induced dynamics. One can mathematically formulate the dynamics of atoms well by using a quantum mechanical treatment. Here an atom can be described by quantum states, and by using a certain basis set, the state is a superposition of the so-called basis states

$$|\psi\rangle = \sum_i c_i |\psi_i\rangle \qquad (2.35)$$

with c_i being the complex-valued amplitude of the basis state $|\psi_i\rangle$. Here the Dirac notation, also called bra-ket notation, is used for the quantum states [43,44], and due to the superposition, the state is formally a vector, which is defined on a state space given by the basis set. The dynamics of the state, i.e., its evolution in time, is governed by the unitary time translation operator $\hat{U}(t', t)$ from time point t to time point t', which is generated by the Hamilton operator $\hat{H}$, also called Hamiltonian. This evolution results from the equation of motion for the state, which can be given in the non-relativistic case by the Schrödinger equation

$$i\hbar \frac{\partial}{\partial t} |\psi\rangle = \hat{H}|\psi\rangle, \qquad (2.36)$$

where $\hbar$ is the Planck constant. The equation intrinsically assumes that the time dependence of the quantum mechanical system is carried by the state, i.e., $|\psi\rangle = |\psi(t)\rangle$, which is called the Schrödinger picture. Equivalent pictures are the Heisenberg or the interaction picture, where the time dependence is completely or partly put in the operators. The interested reader may consult the reference [43,45] for more information about the derivation of the quantum-mechanical equation of motion in the different pictures. If the Hamilton operator is independent of time, meaning $\frac{\partial}{\partial t}\hat{H} = 0$ (Schrödinger picture), the time translation operator becomes

$$\hat{U}(t', t) = e^{-\frac{i}{\hbar}\hat{H}(t'-t)}. \qquad (2.37)$$

In general, the Hamiltonian describes the energy of the system, which are its eigenvalues. With this, the state that is given by equation 2.35 can be rewritten to

$$|\psi(t)\rangle = \sum_i c_i \, e^{-\frac{i}{\hbar}\varepsilon_i t} |\psi_i\rangle \qquad (2.38)$$

where ε_i are the energies of the time-independent basis states $|\psi_i\rangle$ that are eigenstates of the time-independent Hamilton operator.

The treatment of the atom by its quantum states is quite abstract. For an adequate description of the studied physics, the so-called Hilbert space, or state space, has to be defined. In this work, the interaction between electromagnetic fields and atoms is studied with the semi-classical treatment. Thus, the here considered states space is given by the energy eigenstates of the electron in the Coulomb potential of the atom. In order to find these eigenstates, one can extent the Hamiltonian and therewith the state space. First, one can assume the Coulomb potential is generated from a point-like and infinite massive atomic nucleus. Then one considers its finite mass, the fein structure, the hyperfine structure, etc. The discussion of these extensions can be found in the references [46,47]. In this work, the considered state space will always be given.

Furthermore, in quantum mechanics, the electron can be described by a complex-valued wave function, which is defined in, for instance, the spatial or the momentum space. The equations describing the wave function's evolution are then similar to the equations above, where the operators are transformed to adhere to the respective space. As an example, the Schrödinger equation of the spatial wave function $\psi(\vec{r}_1, \vec{r}_2, t)$ of two electrons in the Coulomb field of the helium nucleus with the nuclear charge number $Z = 2$ and approximately infinite mass is given by

$$i\hbar \frac{\partial}{\partial t}\psi(\vec{r}_1, \vec{r}_2, t) = \left[\frac{\hat{p}_1^2 + \hat{p}_2^2}{2m_e} - \frac{Ze^2}{4\pi\varepsilon_0}\left[\frac{1}{|\hat{r}_1|} + \frac{1}{|\hat{r}_2|}\right] + \frac{e^2}{4\pi\varepsilon_0}\frac{1}{|\hat{r}_1 - \hat{r}_2|}\right]\psi(\vec{r}_1, \vec{r}_2, t), \quad (2.39)$$

where $\hat{r}_1$, $\hat{r}_2$, $\hat{p}_1$and $\hat{p}_2$ are the relative coordinate operators of the electrons with respect to the nucleus and the momentum operator of the two electrons, respectively.

Introducing now an electric field pulse in the system, it is convenient to let the Hamiltonian become explicitly time-dependent. Strictly speaking, due to this time-dependency, the system cannot be described within the Schrödinger picture. Therefore, in the following, the interaction picture is used, which nevertheless leads to similar equations. With the time-dependent Hamiltonian, the solution for the state's time evolution can become very complex, where one has to find the eigenstates of the Hamiltonian at every moment in time. Since this is very demanding, one often uses computer programs to solve the time-dependent Schrödinger equation on a discretized time grid. For this purpose, assumptions for the description of the system are made in order to simplify the calculations or relax the computational costs.

One prominent example is time-dependent perturbation theory, which can be used if the field strength is weak, meaning the characteristic energies due to the field are small compared to the energies given by the field-free Hamiltonian [45]. Here a small time-dependent perturbation $\hat{V}(t)$, e.g., a weak oscillating field is added to the free time-independent Hamiltonian $\hat{H}_0$

$$\hat{H}(t) = \hat{H}_0 + \lambda\hat{V}(t) \quad (2.40)$$

with λ being a small scalar parameter. Assuming the eigenstates $|\psi_i\rangle$ and eigenvalues ε_i of the free Hamiltonian are known, the time-dependent perturbation theory aims to approximately solve the Schrödinger equation for the Hamiltonian given by equation 2.40. As mentioned above, the solution can be written as a time-dependent state $|\psi(t)\rangle$ in terms of the basis set of the free Hamiltonian

$$|\psi(t)\rangle = \sum_i c_i(t)\, e^{-i\frac{\varepsilon_i}{\hbar}t}\, |\psi_i\rangle \qquad (2.41)$$

Here the state amplitudes $c_i(t)$ explicitly depend on time due to the addition of the time-dependent perturbation in the Hamiltonian. Using this description, the problem is reduced to find an expression for the amplitudes. This can be done by putting the Ansatz given by equation 2.41 in the Schrödinger equation and projecting the whole equation to a bra state $\langle\psi_j|$, which yields

$$i\hbar \frac{dc_j(t)}{dt} = \lambda \sum_i c_i(t)\, e^{i\omega_{ij}t}\, \langle\psi_j|\hat{V}(t)|\psi_i\rangle \qquad (2.42)$$

with $\omega_{ij} = (\varepsilon_j - \varepsilon_i)/\hbar$ being the transition angular frequency from state $|\psi_i\rangle$ to $|\psi_j\rangle$.

One can see from equation 2.42 that the trajectory of the amplitude $c_j(t)$ will depend on all amplitudes of the other states and vice versa. In order to solve this equation, despite its complexity, one can make some assumptions about the system. First, in most treated cases, the atom is in its ground state $|\psi_g\rangle$ at the beginning of the perturbation, i.e.,

$$c_g(t=0) = 1 \quad \text{and} \quad c_i = 0 \;\; \forall\, i \neq g \qquad (2.43)$$

holds. Second, since the perturbation is small, determined by the small parameter λ, one can make the Ansatz that the solution for the time-dependent state amplitudes can be expressed in a power series of λ

$$c_i(t) = c_i^{(0)}(t) + \lambda\, c_i^{(1)}(t) + \lambda^2\, c_i^{(2)}(t) + \cdots \qquad (2.44)$$

Putting this Ansatz in equation 2.42 leads to the differential equations

$$\begin{aligned} &i\hbar \frac{dc_j^{(0)}(t)}{dt} + \lambda\, i\hbar \frac{dc_j^{(1)}(t)}{dt} + \mathcal{O}(\lambda^2) \\ &= \lambda \sum_{i=0}^{\infty} c_i^{(0)}(t)\, e^{i\omega_{ij}t}\, \langle\psi_j|\hat{V}(t)|\psi_i\rangle + \mathcal{O}(\lambda^2). \end{aligned} \qquad (2.45)$$

This equation is now separable into equations for the different orders of λ, and since λ is small, the first orders will dominate. The zeroth-order results in

$$i\hbar \frac{dc_j^{(0)}(t)}{dt} = 0, \qquad (2.46)$$

which means that there is no change in time for the amplitude of the zeroth order, and due to the initial condition given by 2.43, the amplitudes vanish except for the ground state amplitude, which remains unity.

Using the result for the zeroth-order, the equation for the first order in λ becomes

$$i\hbar \frac{dc_j^{(1)}(t)}{dt} = e^{i\omega_{ij}t} \langle \psi_j | \hat{V}(t) | \psi_i \rangle, \quad (2.47)$$

which can be solved directly by integration and using the initial conditions

$$c_j^{(1)}(t) = -\frac{i}{\hbar} \int_0^t e^{i\omega_{ij}t'} \langle \psi_j | \hat{V}(t') | \psi_i \rangle \, dt'. \quad (2.48)$$

Within the perturbation theory, the first order amplitudes stay small. The population ρ_j of the state is given by the absolute square of the state amplitudes

$$\rho_j(t) \approx \left| c_j^{(0)} + c_j^{(1)}(t) \right|^2, \quad (2.49)$$

which is approximately unity for the ground state or which is a small number for the other states.

Considering the case for the light-matter interaction in the dipole approximation, the time-dependent perturbation becomes

$$\hat{V}(t) = \hat{\mu} \, F(t), \quad (2.50)$$

where $\hat{\mu}$ is the dipole operator that will be described in more detail in the next section. Using a plane wave for the electric field, i.e., $F(t) = f_0 \cos(\omega t) = \frac{f_0}{2}\left(e^{i\omega t} + e^{-i\omega t}\right)$, and putting this field into equation 2.48, one obtains imaginary exponents of the form

$$i(\omega + \omega_{ij})t \quad \text{and} \quad i(\omega - \omega_{ij})t. \quad (2.51)$$

Thus, one gets oscillations of the state amplitude, i.e., transitions between the states, which lead to excitation or de-excitation of the states. If the natural lifetimes of the states are long compared to these oscillations, one can often neglect one term in 2.51, which is known as the rotation-wave approximation.

The perturbation theory can be applied if the field strength is weak. However, if the strength increases, the field-induced couplings between the states can become strong. This results in a considerable transfer of population, an oscillation of population, which is known as Rabi oscillations [48], and shifts in the energy of the states. These energy shifts can easily be derived for a system with only two states $|\psi_1\rangle$ and $|\psi_2\rangle$, a so-called two-level system. Here, a general state can be represented by a vector with the entries given by the state amplitudes

$$|\psi\rangle = \begin{pmatrix} c_1 \\ c_2 \end{pmatrix}. \quad (2.52)$$

In this representation, the Hamiltonian becomes a matrix

$$\hat{H}(t) = \begin{pmatrix} \varepsilon_1 & \mu_{12} \, F(t) \\ \mu_{21} \, F(t) & \varepsilon_2 \end{pmatrix}, \quad (2.53)$$

where $\mu_{ij} = \langle\psi_i|\hat{\mu}|\psi_j\rangle$. The off-diagonal elements of the Hamiltonian lead to a laser-induced coupling of the states $|\psi_1\rangle$ and $|\psi_2\rangle$, and the static solution of the Schrödinger equation will become a mixture of these states. One can find this solution by diagonalizing the Hamiltonian. It is often obtained in a rotating frame, where the time dependence is removed from the Hamiltonian, and the rotating wave approximation is applied. Assuming that the first state has lower energy than the second, the energies of the static states, i.e., the eigenvalues of the Hamiltonian, become

$$\begin{aligned}\varepsilon_1'(\Delta,\Omega) &= \varepsilon_1 + \frac{\hbar}{2}\left(\mathrm{sign}(\Delta)\sqrt{\Delta^2+\Omega^2} - \Delta\right)\\ \varepsilon_2'(\Delta,\Omega) &= \varepsilon_2 - \frac{\hbar}{2}\left(\mathrm{sign}(\Delta)\sqrt{\Delta^2+\Omega^2} - \Delta\right),\end{aligned} \qquad (2.54)$$

where $\Delta = \omega - (\varepsilon_2 - \varepsilon_1)$ is the detuning of the laser frequency from the transition resonance and $\Omega = \frac{\mu_{12} f_0}{\hbar}$ is the so-called Rabi frequency. One can see from equation 2.54 that for a negative detuning, the energies of the states shift such that the energy difference increases. For a small detuning, the shift is approximately given by the Rabi frequency, which is linear to the field strength. The shifting of the energies is also known as the Autler–Townes effect [49] or AC Stark effect, and it is depicted in figure 2.2 for different Rabi frequencies.

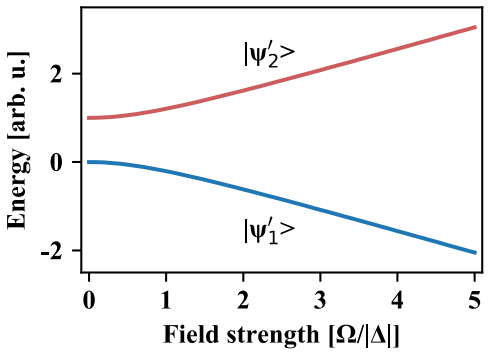

Figure 2.2: The AC Stark effect of a two-level system. For a negative laser detuning, the energies repel each other with increasing Rabi frequency, i.e., for higher field strength. For a positive detuning the state's energy comes closer (not shown).

From the Dipole Response to Linear Absorption and Back

If laser pulses are focused onto a material, they will induce a time-dependent response of the material. By studying this response, one can reconstruct the time-dependent dynamics in the material during its stimulation. In general, the response can be a nonlinear function of the driving field and may depend on the evolution history of the pulse. However, most often and also here, the treatment of instantaneous responses is sufficient. An example of this is the change in the polarization $P(t)$ of a material induced by a time-dependent electric field $F(t)$

$$P(t) = \varepsilon_0\chi(t)F(t) = \varepsilon_0\left(\chi^{(1)}(t)F(t) + \chi^{(2)}(t)F^2(t) + \cdots\right), \qquad (2.55)$$

where $\chi^{(1)}$ and $\chi^{(2)}$ are the linear and quadratic electric susceptibilities. They are natural properties of the material, and more generally, they are described by polarization-dependent tensors, which would result in polarization-modified responses. For simplicity, in the following, this polarization dependence is omitted since most target materials discussed in this thesis have only scalar susceptibilities.

The material's polarization can be ascribed to the averaged dipole moment $\langle\mu\rangle$ of the material's constituents

$$P = \langle\mu\rangle\rho_N \qquad (2.56)$$

with ρ_N being the number density in a certain spatial volume. The dipole moment is defined as the distance between positive and negative electric charges times the value of the charge. Thus, equation 2.56 states that the macroscopic electric field response, the polarization of the material, is generated by a coherent sum of many individual dipole responses on the microscopic scale. Therefore one can connect the results in the measurements probing the macroscopic polarization to the induced dynamics of the dipole response of the material's constituents on the microscopic scale. Using a gas target as the material under investigation, the microscopic constituents are the gas atoms, and the dipole response is generated by the time-dependent dipole moment in the atom.

If the atom is in its ground state and subjected to an electric field pulse, which has a spectrum covering the energies of resonant transition in the atom, the pulse will induce a certain superposition of excited energy states. This superposition leads to a non-vanishing time-dependent dipole moment, which is defined by

$$\vec{\mu}(t) = -e\,\langle\psi(t)|\vec{r}_{\mathrm{e}}|\psi(t)\rangle. \qquad (2.57)$$

Here $\vec{r}_{\mathrm{e}}$ is the sum vector position of all electrons with respect to the atomic nucleus. If the expression of the state is given by an electron wave function in the spatial dimension, the dipole moment will read

$$\vec{\mu}(t) = -e\int_{-\infty}^{\infty}\psi^*(\vec{r},t)\,\vec{r}_{\mathrm{e}}\,\psi(\vec{r},t)\,d\vec{r}. \qquad (2.58)$$

Note that the state $\psi(\vec{r},t)$ is a superposition of energy states, and thus, the dipole moment depends on the spatial overlap integral of these energy states. Since, in the measurement, the laser pulse will only perturbatively excite the helium atom, the state amplitude of the atomic ground state will remain close to unity. In this case, the dipole moment will be dominated by the overlap between the ground state and the excited states. It is worth pointing out that the spatial wave function of the ground state is mostly located close to the atomic nucleus. Therefore, the dipole moment will become a measure for the localization of the electron wave packet with respect to the nucleus.

The field-induced polarization that was introduced above enters in Maxwell‘s equations. Using these equations, one can derive the fundamental wave equation for the propagation of a linearly polarized electric field through media

$$\left[\frac{\partial^2}{\partial z^2} - \frac{1}{c^2}\frac{\partial^2}{\partial t^2}\right] F(t,z) = \mu_0 \frac{\partial^2}{\partial t^2} P(t,z), \qquad (2.59)$$

where μ_0 is the vacuum permittivity and z is the propagation direction. In this equation, the polarization acts as a source for the electric field. The incident field and the field generated by the polarization interfere, leading to a modified total field. If the interference is destructive, it will lead to an attenuation of the field, which is the origin of what is called absorption. For constructive interference, the field amplitude can be enhanced, leading to a net gain. In the experiments presented in this thesis, only dilute gas targets are treated, and thus no propagation effects are considered. This means the polarization is instantaneously induced, and the generated field from the polarization will, in first order, not be disturbed by the medium.

The polarization given by equation 2.55 can also be formulated in the frequency domain using the Fourier transform. It is given in the linear order by

$$\tilde{P}(\omega) = \varepsilon_0 \tilde{\chi}(\omega) \tilde{F}(\omega). \qquad (2.60)$$

The frequency-dependent susceptibility here is the characteristic response function of the material. It can be obtained by rearranging equation 2.60

$$\tilde{\chi}(\omega) = \frac{1}{\varepsilon_0}\frac{\tilde{P}(\omega)}{\tilde{F}(\omega)}, \qquad (2.61)$$

and it is conventionally written as a complex-valued function

$$\tilde{\chi}(\omega) = \tilde{\chi}'(\omega) + i\tilde{\chi}''(\omega), \qquad (2.62)$$

which is linked to the refractive index of the medium via

$$n(\omega) = \sqrt{1 + \tilde{\chi}(\omega)}. \qquad (2.63)$$

Its effect on the incident laser field can be seen by solving the wave equation written in the frequency domain. The well-known plane wave gives one of its solutions

$$\tilde{F}(\omega, z) = \tilde{F}(\omega, 0) e^{ik(\omega)z}. \qquad (2.64)$$

The frequency-dependent wave number $k(\omega)$, which enters in the exponent of the plane wave, can be approximated using a Taylor series, similar to equation 2.21, but here in terms of the susceptibility

$$k(\omega) = \frac{\omega}{c} n(\omega) = \frac{\omega}{c}\sqrt{1 + \chi'(\omega) + i\chi''(\omega)} \approx \frac{\omega}{c}\left(1 + \frac{\chi'(\omega)}{2} + i\frac{\chi''(\omega)}{2}\right), \qquad (2.65)$$

where only the first terms of the series are important since dilute target gases are considered, and thereby the susceptibility is small. Entering this complex-valued wave number into equation 2.64 results in

$$\tilde{F}(\omega,z) = \tilde{F}(\omega,0)\, e^{i\frac{\omega}{c}\left(1+\frac{\chi'(\omega)}{2}\right)z}\, e^{-\frac{\omega}{c}\frac{\chi''(\omega)}{2}z}. \quad (2.66)$$

In this solution, one can see that the real part of the susceptibility is responsible for the dispersion of the wave by adding a phase when it passes through the medium. The imaginary part of the susceptibility, however, induces an attenuation of the field amplitude, which can be observed in terms of absorption. In an experiment, instead of the laser electric field, its intensity can be measured, which is now z-dependent:

$$\tilde{I}(\omega,z) = \frac{1}{2}\varepsilon_0 c \left|\tilde{F}(\omega,z)\right|^2 = \tilde{I}_0(\omega) e^{-\frac{\omega}{c}\tilde{\chi}''(\omega)z}. \quad (2.67)$$

This function is the well-known Lambert-Beer's law, and it can be linked to the frequency-dependent cross-section $\sigma(\omega)$ of the medium with length l and number density ρ

$$\tilde{I}(\omega,z) = \tilde{I}_0(\omega) e^{-\sigma(\omega)\rho\, l}. \quad (2.68)$$

By comparing the exponents of the decaying function in equation 2.67 and 2.68 and using equation 2.56 and 2.61, one obtains

$$\sigma(\omega) = \frac{1}{\rho}\frac{\omega}{c}\,\tilde{\chi}''(\omega) = \frac{1}{\rho}\frac{\omega}{\varepsilon_0 c}\,\mathbb{Im}\left(\frac{\tilde{P}(\omega)}{\tilde{F}(\omega)}\right) = \frac{\omega}{\varepsilon_0 c}\,\mathbb{Im}\left(\frac{\langle\tilde{\mu}(\omega)\rangle}{\tilde{F}(\omega)}\right). \quad (2.69)$$

Thus, the macroscopic cross-section of a dilute atomic gas cloud is directly linked to the imaginary part of the mean frequency-dependent dipole moment of the atoms on the microscopic scale.

In an experiment, instead of the cross-section, the transmitted intensity spectrum $\tilde{I}(\omega)$ can be measured. However, by additionally measuring a reference intensity spectrum $\tilde{I}_0(\omega)$ without a target medium and knowing the target's density and length, one can directly calculate the cross-section using equation 2.68. In the presentation of the measurement results and also often in the literature, the absorbance of the medium is given in units of the optical density. It is defined as the attenuation of the intensity on a decadic logarithmic scale:

$$A(\omega) = -\log_{10}\left(\frac{I(\omega)}{I_0(\omega)}\right) = \frac{\sigma(\omega)}{\ln 10}\,\rho\, l. \quad (2.70)$$

With this definition, one can directly link the absorption spectrum to the time-dependent dipole moment

$$A(\omega) \propto \omega\,\mathbb{Im}\left(\frac{\tilde{\mu}(\omega)}{\tilde{F}(\omega)}\right) = \omega\,\mathbb{Im}\left(\frac{\mathcal{F}[\mu(t)]}{\mathcal{F}[F(t)]}\right). \quad (2.71)$$

It has been shown in the references [50,51] that from this proportionality, one can fully reconstruct the time-dependent dipole moment in amplitude and phase directly from the absorption spectrum. Using linear and ultrashort probing events, the principle of causality implies that in a generally complex response, the imaginary part (absorption) is linked to the real part (dispersion) of the response. This link is known as the Kramers–Kronig relations [52,53]. In this thesis, the dipole response will be

triggered by a weak attosecond pulse, whereby the light-matter interaction is linear and can be described via first-order perturbation theory. This short trigger pulse can be approximated by a Dirac delta function at time zero, $F(t) = F_0 \cdot \delta(t)$, and the causality is given by stating that the dipole moment is zero before the trigger pulse arrives, i.e., $\mu(t < 0) = 0$. The spectrum of the δ-like pulse is flat, and thereby for certain limited spectral range, equation 2.71 can be approximated by

$$A(\omega) \propto \omega \, \mathbb{Im}\left(\frac{\mathcal{F}[\mu(t)]}{\mathcal{F}[F(t)]}\right) \approx \omega_0 \, \frac{\mathbb{Im}(\mathcal{F}[\mu(t)])}{F_0}, \qquad (2.72)$$

where ω_0 is a constant frequency. Using the Kramers–Kronig relations and discarding the moment at negative times due to causality, one can solve equation 2.72 for the complex-valued dipole moment at positive times, which reads

$$\mu(t) \propto \mathcal{F}^{-1}[iA(\omega)](t) = \frac{1}{\sqrt{2\pi}} \int_{-\infty}^{+\infty} iA(\omega) e^{-i\omega t} d\omega \quad \text{for } t > 0. \qquad (2.73)$$

The physical quantity of this time-dependent dipole response can then be retrieved by taking the real part of this expression.

The crucial point about equation 2.73 is that it holds even if the response obey complex time dependence, which, for instance, can be caused by the interaction of the atoms with a second (strong) time-delayed laser pulse. The whole manipulation of the dipole response due to this additional interaction will be imprinted in the absorption spectrum, and the dipole moment can still be reconstructed in amplitude and phase by using equation 2.73. The only condition is that the excitation pulse (the trigger) is instantaneous, and the dipole moment is zero before the excitation.

As was discussed in reference [51], the instantaneous-trigger requirement can even be softened. Realistic attosecond pulses are not δ-like, but they have certain pulse durations T_{atto}, which would contradict the instantaneous condition. However, one can show that equation 2.73 still holds if the trigger pulse duration is shorter than any other timescales of the system, which are, here, the decay time of the dipole response T_μ and the duration of the interaction T_{int}, i.e., $T_{\text{atto}} \ll T_\mu, T_{\text{int}}$. The finite pulse duration of the attosecond pulse will, however, lead to a temporal smoothing of the results for the dipole moment, which is given by the convolution with the function of the pulse of finite width.

Owing to the descriptive illustration of the ongoing physics, when looking at the time-dependent dipole moment, the method for its reconstruction will be extensively used throughout the thesis. By doing so, the absorption spectrum will always be filtered for different energy regions of interest, which helps to select and compare different dynamics involving different excited atomic states.

The Helium Atom

In its neutral form, helium has a doubly charged nucleus and two electrons. The equation of motion for the wave function of both electrons is given by the Schrödinger equation 2.39. The Coulomb repulsion term in this equation and the indistinguishability of the fermionic electrons lead to correlations of the electrons in their dynamics. Due to the relative simplicity and the electron correlation, helium became a benchmark system for many time-resolved absorption spectroscopy experiments [54–58]. In this work, the strong-field-disturbed electron dynamics at the ionization threshold will be investigated. Therefore, the properties of the helium system will be briefly introduced in this section, where further details can, for instance, be found in the references [46,47].

As a result of the electron correlation, the wave function that is the solution of the Schrödinger equation 2.39 cannot be separated into individual wave functions for each electron, i.e.,

$$\psi(\vec{r}_1, \vec{r}_2, t) \neq \psi^{(1)}(\vec{r}_1, t) \cdot \psi^{(2)}(\vec{r}_2, t). \qquad (2.74)$$

Furthermore, an analytical solution of this three-body system is not known or at least was not published (yet). Therefore, the quantitative results of the helium atom's properties, like the energies of its bound states, rely on measurements or predictions using numerical calculations [59–63].

When both electrons occupy the 1s shell, helium is in its ground state, which means both electrons have the principle quantum number $n = 1$ and no angular momentum, i.e., angular quantum number $l = 0$. Considering the spin of the electrons and the Pauli exclusion principle [64], the total electron wave function has to be antisymmetric under the simultaneous exchange of electron spin and coordinates. Therefore, helium has two state series belonging to the parahelium, where the spatial wave function is symmetric under exchange, and to the orthohelium, where the spatial wave function is antisymmetric. In the following, only parahelium will be considered since orthohelium is metastable and decays to the parahelium ground state, and within the dipole approximation, no excitation to the ortho states will happen.

If one electron is excited from the ground state, it will—considering the dipole transition rules—occupy the $n > 1$, $l = 1$ shells, which is the 1snp Rydberg series that converges to the first ionization continuum denoted by $N = 1$. The states that are accessed by dipole allowed transitions are often called bright states, and the states, which are dipole forbidden from the ground state, are called dark states. Therefore, the bright states are the 1snp states, and the dark states are the 1sns, 1snd states, etc. Often the notation for the states follows the Russell-Saunders term symbol given by ${}^{2S+1}L^{\pi}$. Here L is the total angular momentum quantum number, S is the total spin quantum number, and π denotes the parity of the state, which can be even (e or +1)

or odd (o or -1). The ground state of the helium atom within this notation is $^1S^e$. The transition rules from the initial state i to the final state f are $\Delta L = \pm 1$, $\pi_i \pi_f = -1$ and $\Delta S = 0$.

The two-electron structure of the helium atom has a variety of consequences. Aside from the single-electron excitations, both electrons can be excited by a single photon. These accessed doubly excited states form a Rydberg series converging to the $N = 2$ threshold at ~65.40 eV. They lie energetically above the first ionization threshold $N = 1$ and are thus degenerate with the ionization continuum, in which one electron is ionized, and the other occupies the ground state of the ion. This degeneracy and the Coulomb repulsion between the electrons lead to a coupling between the doubly excited states and the ionized state known as configuration interaction. Due to this interaction, the doubly excited states autoionize, and therefore these states possess much shorter lifetimes than the singly excited states. Three different doubly excited state manifolds are dipole allowed from the ground state, namely the 2snp, the 2pns, and the 2pnd series. Transitions to the latter are unfavored, leading to a low photoabsorption cross-section, and they have not been observed in the measurements presented here. Since the electrons are indistinguishable, the 2snp and 2pns states couple, and the observed transitions are linear combinations of these states denoted by

$$\mathrm{sp}_{2,n\pm} = \frac{1}{\sqrt{2}}(2sn\mathrm{p} \pm 2\mathrm{p}ns), \qquad (2.75)$$

where the '+'-series appears stronger. The singly excited and the doubly excited states relevant in this thesis are depicted in the level diagram shown in figure 2.3.

The process of autoionization of the doubly excited states gives rise to asymmetries in the cross-sections at the transition resonances. Beutler has observed these asymmetries first [65], and later they were theoretically explained by Fano [66], wherefore, these resonances are called Fano resonances. Fano has shown that the asymmetric line shapes result from the interference between different transition paths to the same final states. In the case of helium, the transition from the ground state to the ionization continuum has two contributions. One transition is directly into the continuum, and the other is via the autoionizing states. These contributions interfere with an opposite sign on each energetic side of the resonances leading to the asymmetric line shapes.

More formally, due to the coupling of the doubly excited state with the ionization continuum, the stationary eigenstate of the Hamiltonian $|\psi_E\rangle$ becomes a superposition of the discrete unperturbed bound state $|\psi\rangle$ and the continuum state $|\xi_E\rangle$. Fano related the transition amplitude from the ground state $|\psi_g\rangle$ to this energy eigenstate and to the continuum state and showed that it can be parameterized by the so-called q-parameter

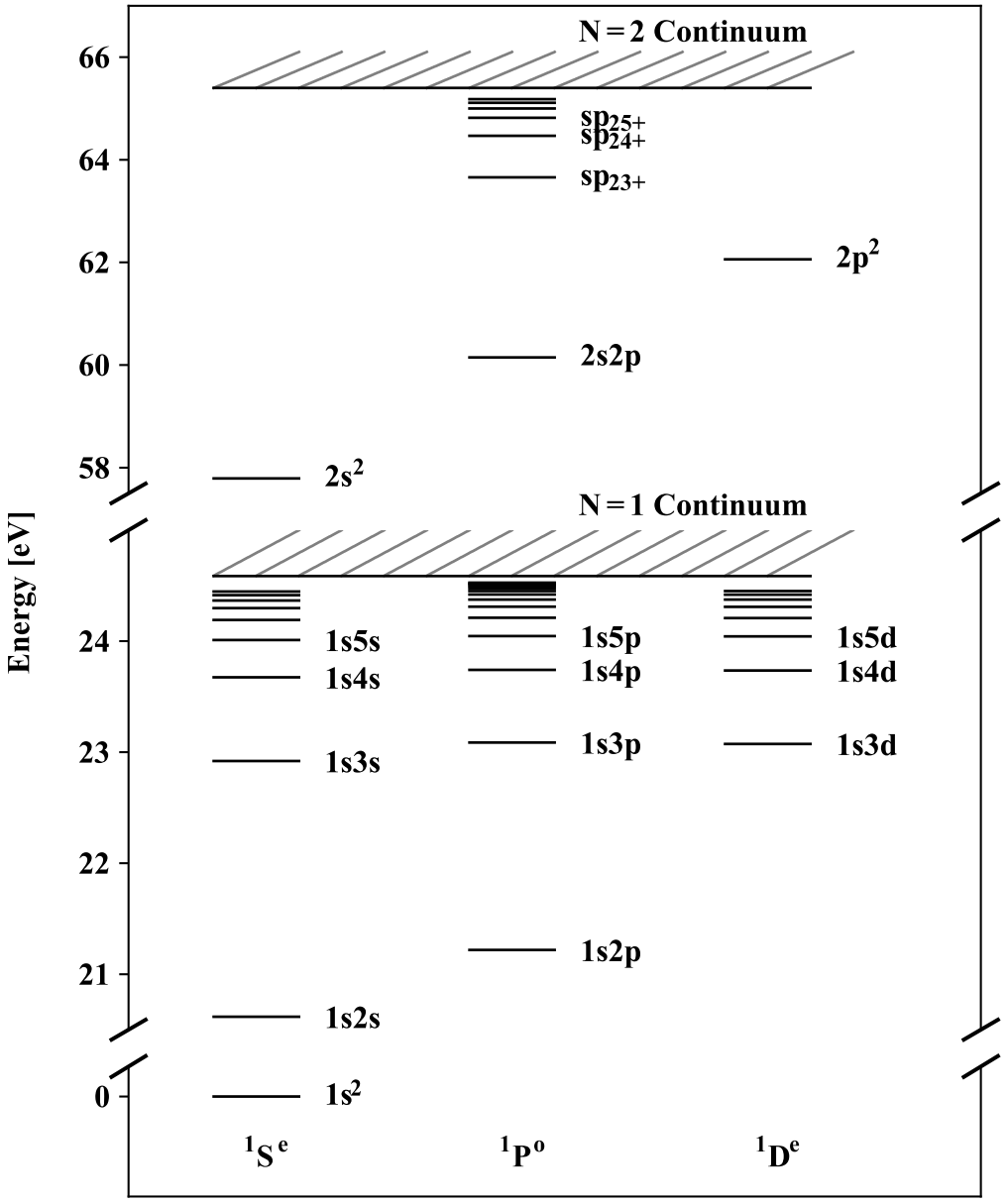

Figure 2.3: Level diagram of the helium atom for the levels converging to the thresholds of the two continua $N = 1$ and $N = 2$ relevant for this work. The levels are grouped to the $^1S^e$, $^1P^o$, and $^1D^e$ manifolds. Note that the energy axis is broken two times. The values are taken from [61, 62].

$$\frac{\left|\langle\psi_E|\hat{T}|\psi_g\rangle\right|^2}{\left|\langle\xi_E|\hat{T}|\psi_g\rangle\right|^2} = \frac{|q+\varepsilon|^2}{1+\varepsilon^2} \qquad (2.76)$$

with $\hat{T}$ being the transition operator and ε the reduced energy

$$\varepsilon = \frac{E - E_{\phi_E}}{\Gamma/2}. \qquad (2.77)$$

Here E_{ϕ_E} and Γ are the energy and linewidth of the transition resonance to the discrete bound state $|\phi_E\rangle$ that is the original discrete state $|\psi\rangle$ modified by the continuum states.

The q-parameter relates the strength of the different interfering contributions

$$q = \frac{\langle \phi_E | \hat{T} | \psi_g \rangle}{\pi V_E^* \langle \xi_E | \hat{T} | \psi_g \rangle}, \qquad (2.78)$$

where $V_E = \langle \xi_E | \hat{H} | \psi \rangle$ is the strength of the configuration interaction.

In the end, the observed cross-section across a resonance to a doubly excited state will be directly proportional to the transition ratio given in equation 2.76

$$\sigma = A \frac{|q + \varepsilon|^2}{1 + \varepsilon^2} + \sigma_{\mathrm{NR}}, \qquad (2.79)$$

where A is the strength of the resonance and σ_{NR} denotes the non-resonant background absorption, which can result from different ionization channels.

The cross-sections for different q-parameters are shown in figure 2.4. For small negative or positive values of q, the cross-section is asymmetric across the resonance, and for $q = 0$, only a drop of the cross-section is obtained, which is known as window resonance. For very large negative or positive values, equation 2.78 states that the configuration interaction is negligible, or the amplitude of the direct transition to the continuum is low. This leads to a cross-section with the well-known Lorentzian line shape.

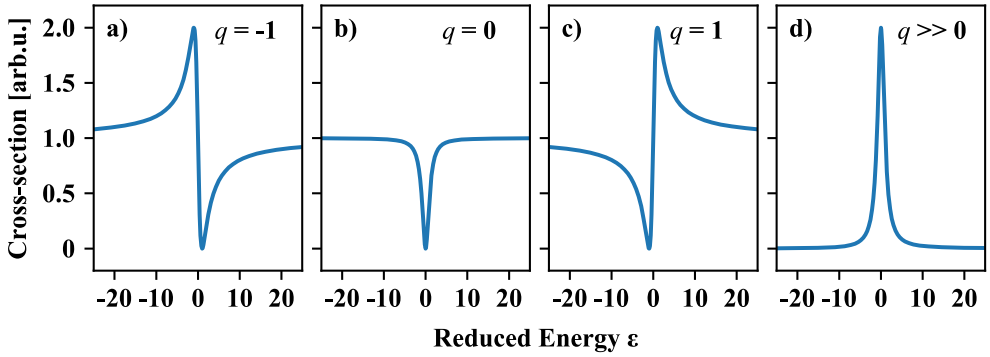

Figure 2.4: The cross-section of the asymmetric Fano resonance for different q-paramters versus the reduced energy defined by equation 2.77. a) For q = -1, coming from lower energies across the resonance the cross-section increases first, drops fast to low values and recovers to 1. b) For q = 0 the cross-section only drops at the resonance revealing a window resonance. c) The cross-section for q = 1 is inverted to the cross-section for q = -1 in a). d) For very large positive and negative values for q, the resonance has the well-known Lorentzian line shape.

The Dipole Control Model

As introduced in a previous section, the photoabsorption cross-section is linked to the imaginary part of the dipole moment; see equation 2.69. Thus, the asymmetric Fano-shaped absorption lines of the helium doubly excited resonances should have an explicit correspondence in the time-dependent dipole moment. It was shown in reference [35] that this is given by linking the Fano asymmetry parameter q to the initial phase of the dipole moment after its excitation by a delta-like pulse at $t = 0$. It is then given by

$$\mu(t) \propto i\, e^{-\frac{\Gamma}{2\hbar}t - i\frac{E}{\hbar}t + i\phi_{\mathrm{Fano}}(q)} \qquad (2.80)$$

with the relation

$$\phi_{\mathrm{Fano}}(q) = 2\arg(q - i) \qquad (2.81)$$

and the back transformation

$$q(\phi_{\mathrm{Fano}}) = -\cot\left(\frac{\phi_{\mathrm{Fano}}(q)}{2}\right). \qquad (2.82)$$

Assuming a flat excitation spectrum, this dipole response leads to an absorption cross-section that reads

$$\sigma(\omega) \propto \mathbb{Im}[\tilde{\mu}(\omega)] \propto \mathbb{Im}\left[\int_{-\infty}^{\infty} \mu(t) e^{i\omega t} dt\right] \propto \mathbb{Im}\left[\frac{e^{i\phi_{\mathrm{Fano}}(q)}}{(E - \hbar\omega) - i\,\Gamma/2}\right]. \qquad (2.83)$$

For a zero Fano phase, the dipole moment results again in the well-known Lorentzian-shaped absorption line corresponding to $q = \pm\infty$.

In reference [35], it was possible to control this initial phase by dressing the excited state with a strong near-infrared (NIR) pulse immediately after its excitation. This dressing leads to a phase shift in the dipole moment given by the product of the pulse duration and the NIR-induced energy shift and thereby changes the absorption line shape from Lorentzian to Fano and vice versa. Here, the phase shift on the dipole moment was at the instant of the excitation. In a more recent work [33], this picture was extended, where the phase shift happens with a controllable time delay. Similarly, it was induced by an NIR pulse, but now with a certain delay with respect to the excitation. The phase shift was still approximated to happen impulsively since the pulse durations were short compared to the lifetimes of the excited states. Furthermore, the strong pulse could deplete the excited states by means of ionization or resonant coupling to other states, which impulsively reduces the response amplitude after a certain time delay.

The laser-induced manipulations of the dipole response were described in the time domain by the so-called dipole control model (DCM). In this model, the response is split into two sequential parts. The first describes the freely decaying dipole moment

starting at time $t = 0$, and at the time delay τ, the phase and amplitude of the moment are impulsively changed by the laser:

$$\mu(t,\tau) \propto \begin{cases} i\, e^{-\frac{\Gamma}{2\hbar}t - i\frac{E}{\hbar}t + i\phi_{\mathrm{Fano}}(q)} & \text{for } 0 < t < \tau \\ i\, e^{-\frac{\Gamma}{2\hbar}t - i\frac{E}{\hbar}t + i\phi_{\mathrm{Fano}}(q)} \cdot A_{\mathrm{DCM}}(\tau) e^{i\phi_{\mathrm{DCM}}(\tau)} & \text{for } t > \tau \end{cases} \qquad (2.84)$$

The resulting cross-section can even be found analytically by means of the Fourier transformation and results in

$$\sigma(\omega) \propto \mathbb{Im}\left[\frac{1 - e^{-\frac{\Gamma}{2\hbar}\tau - i\left(\frac{E}{\hbar}-\omega\right)\tau}\left(1 - A_{\mathrm{DCM}}(\tau)e^{i\phi_{\mathrm{DCM}}(\tau)}\right)}{(E - \hbar\omega) - i\,\Gamma/2}\; e^{i\phi_{\mathrm{Fano}}(q)}\right]. \qquad (2.85)$$

This equation will later be used to fit the absorption line shapes of resonances from bound-bound transitions. More details of the DCM will be discussed in the sixth chapter of this thesis, where a model will be introduced that describes the manipulation of the dipole moment in time beyond the impulsive approximation.

The Attosecond Pulse via High Harmonic Generation

The goal of this thesis is to study the electron dynamics in the helium atom within strong fields. For this purpose, the quantum dynamics shall be initiated by a transition to a superposition of coherently excited states. As presented in the section about the helium atom, the transition energies from the ground to the excited states are on the order of tens of eV. To be able to drive these transitions with single photons, one needs laser pulses with a frequency bandwidth that covers the vacuum ultraviolet or extreme ultraviolet (XUV) spectral region. Furthermore, the speed of the dynamics is governed by the energy differences of the excited states, which is on the order of a few femtoseconds. The excitation step should ideally be instantaneous, defining time zero. Thus, pulses below the femtosecond, approaching the attosecond regime are beneficial.

For the production of such pulses in a tabletop system, high harmonic generation (HHG) became the method of choice [39,67]. This is a highly nonlinear coherent light-matter interaction process, where a strong laser pulse with a duration of several femtoseconds and peak intensities of more than 10^{14} W/cm^2 is partly converted into a single or a train of pulses with durations on the attosecond timescale. The photon energies of these pulses are multiples of the central photon energies of the fundamental pulse up to few hundreds of eV [68]. The generation process can be formulated quantum mechanically or more intuitively by a quasi-classical three-step model [69,70]. Both will be briefly introduced in the following, whereas more detailed descriptions can be found in the references [40,71].

In the classical model, an atom is exposed to an oscillating electric field of a strong laser pulse, as depicted in figure 2.5. In the first step of the model, the strong electric

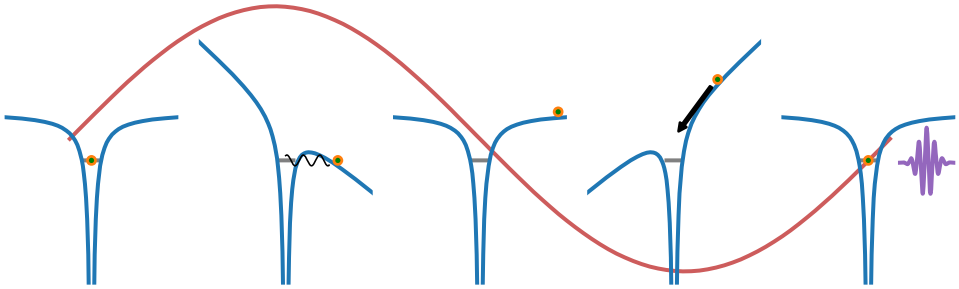

Figure 2.5: Sketch of the three-step model to explain the generation of high harmonics. From left to right: An electron (green orange) occupies a bound state (grey line) in the Coulomb potential of an atom (blue). If the laser field (red curve) increases, the potential, to which the electron is subjected to, gets deformed, and the electron may tunnel through the Coulomb potential (black wavy line). As the field cycle evolves, the liberated electron gains kinetic energy and can be forced back to the parent ion when the field flips sign. The electron can then recombine into its initial state and release its energy in the form of a high-energy photon, which is represented by a violet pulse.

field deforms the Coulomb potential of the atom to which an electron is subjected. As a result, the electron may tunnel through the Coulomb barrier. The field forces the electron away from the residual ion, whereby it gets accelerated and gains kinetic energy E_{kin}, the second step. In the next half-cycle of the oscillatory field, the free electron gets driven back into the ion, which can lead to the recombination of the electron, the last and third step. The recombination energy can be ejected by a high-energy photon with the energy

$$\hbar\omega_{\mathrm{HHG}} = E_{\mathrm{kin}} + I_{\mathrm{p}}. \qquad (2.86)$$

Within this classical treatment, one can show that the electron can follow two different trajectories that lead to the same kinetic energy. They depend on the time when the ionization step happens within the electric field cycle, and they are known as the short and the long trajectory. The time window for the tunnel ionization for each trajectory covering a broad recombination energy spectrum is below a quarter of the fundamental electric field cycle. This leads to the emittance of a broad photon energy spectrum, known as the plateau region, which, in turn, leads to a pulse on the attosecond timescale. When the electron is accelerated in the laser field, it can acquire the maximal kinetic energies of 3.17 U_{p}. Therefore, the emitted photon energy spectrum is limited to a certain cut-off that is given by

$$\hbar\omega_{\mathrm{HHG,cut-off}} = 3.17\, U_{\mathrm{p}} + I_{\mathrm{p}}. \qquad (2.87)$$

In the quantum-mechanical description, the electron is treated as a wave packet consisting of the ground state wave function and an ionized wave function. The ionized part is accelerated in the laser field, and it is driven back to the vicinity of the parent ion. This leads to an interference of the ionized and ground-state wave function and results in a fast oscillating dipole moment. This dipole moment, in turn, is the source that generates the high harmonic field. Due to the sub-cycle nature of the

production of the harmonics, the attosecond pulses are directly locked in phase and time to the electric field of the fundamental laser pulse.

In the described models for the underlying process in HHG, only a single atom is considered. However, the harmonics are typically produced in an atomic cloud, and the microscopic responses of each individual atom are coherently added up into a macroscopic signal. In order to increase the harmonic yield, one has thus to optimize the phase matching between the individual atomic emitters. Experimentally this can be done by placing the atomic cloud at a different position within the Rayleigh range of the spatially focused fundamental laser beam or by adjusting a certain atomic density [72]. Even in the best phase-matching conditions, the overall conversion efficiency will be 10^{-6} to 10^{-4}. Thus, the field strength of the attosecond pulses is weak, and the interaction between these pulses and target media can often be treated perturbatively.

In HHG, the ionization and recombination of the electrons happen every half-cycle of the fundamental field, leading to a train of attosecond pulses with half-cycle repetition. In the spectral domain, their interference gives rise to a discrete harmonic comb spectrum with an energy spacing of two fundamental photons $2\hbar\omega_{\mathrm{Fund}}$. Furthermore, using an isotropic conversion medium as an atomic cloud, for symmetry reasons, only harmonics with an odd number of the fundamental photon energy are produced. If the generation process is limited to only one half-cycle of the fundamental oscillation, a single attosecond pulse will be produced, which corresponds to an almost flat broadband energy spectrum. This isolation of an attosecond pulse can be achieved by using a gating mechanism. Different gating mechanisms have been developed, e.g., polarization gating [73,74], ionization gating [75,76], or lighthouse gating [77].

For the conversion medium, most often, rare gases are used due to their relative high ionization potentials. This increases the obtainable photon energies (see equation 2.86) and reduces the generation of plasma, which would lead to spatial and temporal distortion of the fundamental laser pulse and therewith perturb the phase matching. Besides the atomic conversion media, nowadays, attosecond pulses are produced using conversion media in the condensed [78] or in the liquid phase [79,80].

As seen by equation 2.86, the highest achievable photon energy depends on the ponderomotive potential U_{p}. It is proportional to the laser intensity and the wavelength squared; see equation 2.33. Thus, for longer wavelengths of the fundamental laser, higher photon energies are obtainable. However, the recombination efficiency scales with $\lambda_{\mathrm{Fund}}^{-6} - \lambda_{\mathrm{Fund}}^{-7}$ [81]. Since the photon yield strongly decreases for high wavelengths, driving laser pulses in the NIR or visible spectral region are typically used for HHG.

3. Experimental setup

For the observation of quantum mechanical dynamics in atoms by absorption spectroscopy on the electrons' natural timescale of an attosecond, an experimental setup with a high temporal and spectral resolution is needed. For this purpose, attosecond transient absorption spectroscopy (ATAS) is a suitable method. In this chapter, this experimental method is described, together with its implementation by an all-optical attosecond beamline at the Max Planck Institute for Nuclear Physics, which has already been treated in several other theses, e.g., [51,82–85]. The description here emphasizes in more detail the experimental components that were developed within this doctoral dissertation and provides, in addition to that, a reference for the future.

In ATAS, a laser pulse with a pulse duration on the attosecond timescale is produced and delayed in time with respect to an (intense) femtosecond laser pulse in the near-infrared (NIR) spectral region. The attosecond pulse, which is in the extreme ultraviolet (XUV) spectral region, propagates through a target of interest, and its transmission spectrum is recoded by an XUV spectrometer afterwards. Spectral absorption signatures such as sharp absorption lines or continuous spectral absorption, which are characteristics of the target, are then embedded in the XUV transmission spectrum. The NIR pulse manipulates these spectral signatures, and their changes are recorded for different time delays between the XUV and NIR pulse, which is the basic concept of ATAS, or for different NIR intensities.

As discussed in the previous chapter, in order to produce attosecond light pulses on a tabletop system, one uses high harmonic generation (HHG) of a laser pulse preferentially in the NIR spectral region, which is converted using (often) an atomic gas ensemble within an evacuated environment. For HHG, high peak intensities on the order of 10^{14} W/cm^2 are needed that are achievable by combining high pulse energies with ultrashort pulse durations and small focal spot sizes. To reach these pulse specifications, one needs several pulse amplification and pulse-duration compression stages in a single laser system.

In this chapter, first, the technical aspects of a laser system for the production of a few-cycle NIR pulse are described. Second, the measurement of the pulse durations, their optimization, and stabilization are treated. The discussion follows the experimental realization of the HHG and thereby the production of attosecond pulses. The two pulses are then used to realize a time-delay and intensity-dependent transient absorption spectroscopy experiment in a, here called, attosecond beamline. The chapter ends with two upgrades of the beamline: an external interferometer for the NIR beam in order to realize an NIR-polarization-dependent experiment and the

spectral measurement of the blue-shift of the fundamental NIR accumulated in the process of HHG.

Generation of Ultrashort Near-Infrared Pulses

The laser setup starts with a commercial system, the FEMTOPOWER^{TM} HE/HR CEP4, by FEMTOLASERS (now Spectra-Physics), which consists of a carrier-envelope-phase-stabilized oscillator and a multi-pass chirped-pulse amplifier (CPA). A sketch of the laser system's components is shown in figure 3.1. In the following, the components of this specific system used to obtain the results presented in this thesis are described. However, the optical techniques used by the system, the mode-locking and the CPA are standard techniques of many ultrashort laser systems in different areas also outside physics, wherefore, the inventors of the CPA have even been honored by the Nobel prize recently [11,86,87].

The oscillator has a titanium-doped sapphire (Ti:Sa) crystal as a gain medium in a mode-locking cavity and a CEP-stabilization module. The Ti:Sa is pumped by a pump laser (Millenia by Spectra-Physics) at ~3.5 W. The output laser pulse of the oscillator cavity has a continuous octave-spanning spectrum centered at 800 nm central wavelength, and it supports sub-10 fs pulse duration with a pulse energy of 6 nJ. After leaving the oscillator cavity by leaking through an output mirror at a repetition rate of 75 MHz, the pulse train is steered into the CEP-stabilization module (CEP4). In this module, the carrier-envelope offset frequency f_{CEO} of the pulse train is determined. For this purpose, a difference frequency signal is produced by focusing

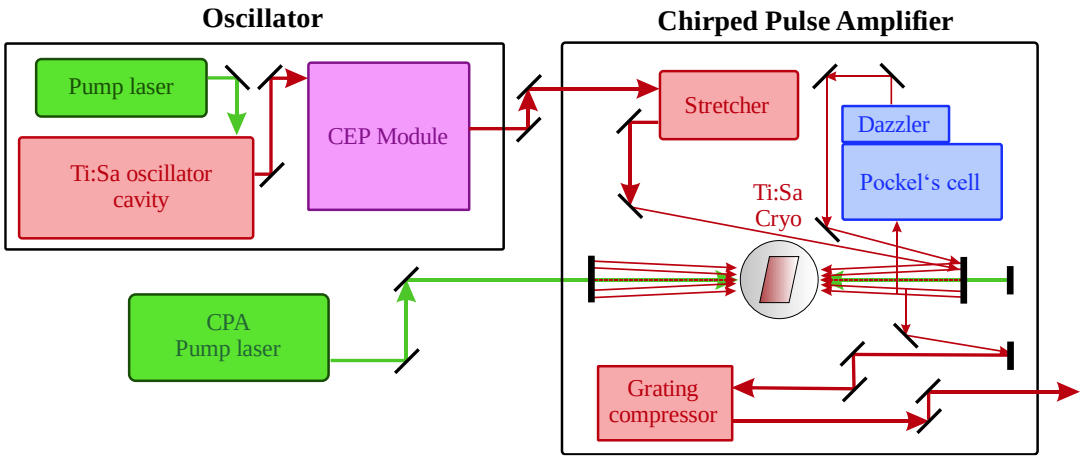

Figure 3.1: Sketch of the commercial laser system for the generation of near-infrared pulses, which is split into two parts, an oscillator and a chirped pulse amplifier. The arrows indicate the propagation of the laser pulse steered by optical mirrors (black bars) through the several pulse manipulation stages (colored boxes). The abbreviation Ti:Sa stands for titanium-doped sapphire crystal, Cryo for cryogenic cooler, CEP for carrier-envelop phase, and CPA for chirped-pulse amplification. The functionality of the individual components is described in the main text.

the oscillator's output pulses into a periodically poled lithium niobate crystal. The difference frequency then beats with a low-frequency line of the fundamental one-optical-octave-spanning spectrum. See reference [88] for more information about this difference frequency generation scheme. Using the deviation from a set point (~10 MHz) of this beat signal as an error signal, long term drifts of the frequency offset are compensated by thermal stabilization of the Ti:Sa crystal in the oscillator (slow loop) and by the automatically controlled moving of dispersive glass wedges inside the oscillator's cavity geometry (CEP-O'clock). The short term drifts of the offset frequency are compensated by an acousto-optic frequency shifter (AOFS) inside the CEP module. It is triggered by the offset frequency plus the repetition rate of the oscillator. This shifter diffracts the laser beam by an acoustic wave into different spatial beam orders and thereby subtracts the frequency offset from the frequency comb spectrum. This corresponds to no pulse-to-pulse phase change in the time domain. With this feed-forward technique, a CEP stabilization with a standard deviation of a few mrad is achievable [89].

After coupling-out from the CEP module, the pulsed laser beam is used to seed another Ti:Sa laser leading to its amplification. Here, the seed pulse passes the same gain medium ten times in total. In order to prevent damage in the crystal by the peak power of the seed pulse, first, the pulse is stretched into the picosecond timescale to lower the peak intensity below the damage threshold. For this purpose, the pulse propagates through fused-silica that adds a positive group delay dispersion (GDD) onto the temporal phase of the pulse, which results in a positive chirp in time. The introduction of a chirp on the pulse before its amplification triggered the naming of the chirped pulse amplification laser system. The gain medium is pumped by a Q-switched pump laser (DM-50 by Photonics Industries) at a repetition rate of 3 kHz and high average power of around 40 W [90]. The Ti:Sa-crystal absorbs this power, and for further heat compensation and stabilization purpose (reducing thermal lensing), it is cryogenically cooled to ~102 K under high vacuum conditions of 10^{-7} mbar total pressure.

After the 4th pass through the gain crystal, the laser beam is directed into a Pockels cell and a Dazzler crystal. The fast-switching Pockels cell selects one pulse of the pulse train synchronized with the pump laser, which leads to a lowering of the repetition rate of the whole laser to 3 kHz. The selection is achieved by rotating the polarization of a single pulse by $\pi/2$ with an electronically triggered birefringent material in the Pockels cell. A cubic beam splitter after the cell lets the polarization-rotated pulse pass while the other polarization is dumped. The Dazzler module consists of a birefringent para-tellurite crystal as an acousto-optic modulator with the option to tune the spectral phase and amplitude of the acoustic wave in the crystal. During the diffraction of the pulse, the acoustic wave imprints a controllable phase onto the time phase of the pulse and changes its spectral amplitude. Shaping the spectral amplitude helps to reduce gain-narrowing in the amplifier. With the help of

the Dazzler, one can thus control the total temporal shape of the pulse at the output of the laser system, and therewith one can tune the time duration of the pulse even at the entrance of the experimental attosecond beamline, which will be shown below. The timings between the Pockels cell, the amplifier pump laser, and the Dazzler are crucial for an efficient and stable laser pulse amplification. Therefore, they are controlled by a timing unit, which can delay the different electric trigger signals of the components with respect to each other.

After passing the Dazzler, the selected pulse passes another six times the Ti:Sa crystal and gets amplified in total to a single pulse energy of about 3.5 mJ. This energy is distributed on the picosecond timescale. In order to increase the peak intensity and lower the pulse duration, the pulse is guided into a grating compressor. In this compressor, the laser beam is diffracted by two transmission gratings into all the different colors it consists of. Each color propagates a different path length through the compressor and is back-reflected into the gratings, which synthesize the parts back into a single pulsed beam. The net effect of the grating compressor is the introduction of a negative GDD, i.e., a negative frequency chirp, on the pulse. It thereby compresses it down to about 20 to 25 fs. This pulse duration is longer than the initial seed pulse due to gain narrowing of the pulse spectrum centered at 780-790 nm with a bandwidth of about 100 nm. The pulse loses some energy during propagation through the compressor. The final pulse energy is 3 mJ, such that at 3 kHz repetition rate, it leads to the average output power of 9 W.

Since the amplification efficiency crucially depends on the beam pointing of the seed, it is stabilized by a beam alignment system. Here, two four-quadratic photodiodes record the intensity across the transverse section of the laser beam at two different points. They are positioned in front of the amplification stage and thereby creating an error signal if the beam-pointing moves, which can be caused, for instance, by temperature or humidity fluctuations inside the laboratory. The error signal is used to steer two Piezo-actuated mirrors, which compensate for the beam movement. With the help of two sensors and mirrors, one can correct both shifts of the position of the beam pointing and the propagation angle with respect to the optical components. Another beam alignment system is implemented to stabilize the pointing of the focus into the hollow-core fiber, the utilization of which will be discussed in the next section.

Compression of the Pulse Duration to the Few-Cycle Regime

As mentioned above, the time resolution of a transient absorption measurement is linked to the duration of the pulses used for the experiment. In order to observe changes of the absorption within femtoseconds (typical evolution timescale for wave packets in helium), ultrashort pulses with a duration of at most a few femtoseconds

are needed. Thus, one has to further compress the output pulse of the NIR laser, delivering pulses of 20 to 25 fs, down in time.

In addition, ultrashort NIR pule durations facilitate the generation of high harmonics used for the experiment. Since the NIR pulse central wavelength λ_c is about 780 nm, one laser electric field cycle at a particular position of the laser beam's propagation path takes $t = \lambda_c/c \approx 2.6$ fs, where c is the speed of light. Thus, by compressing the NIR pulse to a few femtoseconds, the whole pulse mainly consists of only a few electric field cycles. In this case, the pulse energy is concentrated in these cycles leading to high peak intensities. Since high harmonic generation is a nonlinear process in peak intensity, its efficiency increases [91,92]. Furthermore, if only a few intense cycles exist, the attosecond pulse train will consist of only a few pulses or even of only one isolated pulse with only some weak satellites. If the leading NIR cycle is even strong enough to almost fully ionize the conversion medium, the phase matching for the following cycles will be destroyed. Forcing this NIR-cycle-intensity-dependent isolation of an attosecond pulse is known as ionization gating [75,76]. The ionization gating technique is used in this work to obtain almost a single attosecond pulse and/or to obtain a broad and continuous harmonics spectrum.

For the time compression of the NIR pulse to only a few cycles, the laser beam is guided through a doubly differently pumped hollow-core fiber and a chirped mirror compressor. Figure 3.2 sketches the experimental setup for the compression stages. In general, due to the Fourier limit, one has to broaden the spectrum of the pulse in order to decrease its time duration. In the setup, the broadening is achieved by the generation of additional frequencies induced by self-phase modulation during the propagation through helium in the hollow-core fiber. Self-phase modulation is a

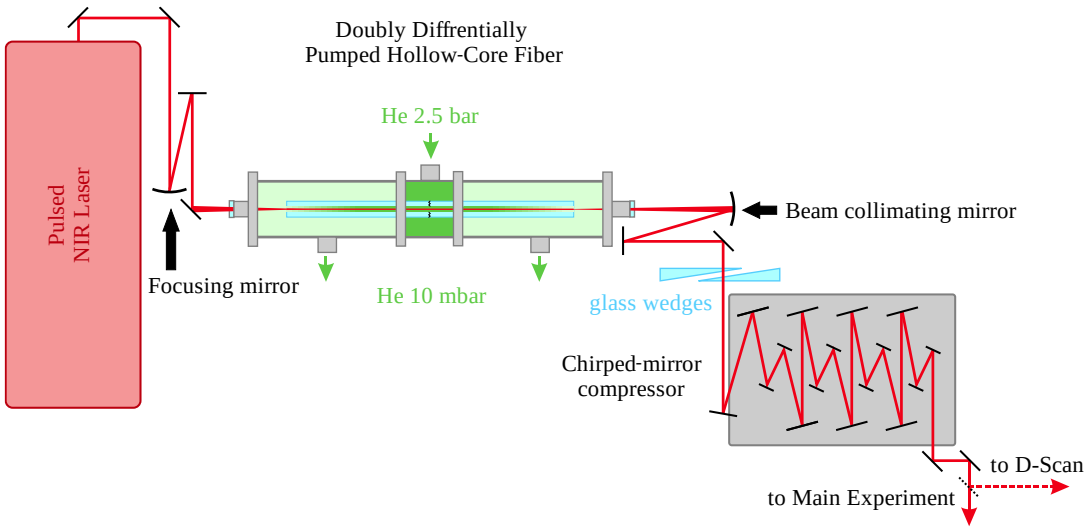

Figure 3.2: The experimental setup for the time compression of the 20 fs NIR Laser output pulses to the few-cycle time regime with pulse durations below 5 fs. The spectrum of the pulse is broadened by a doubly differentially pumped hollow-core fiber and the introduced positive chirp is compensated by an array of chirped mirrors. The dispersion is fine-tuned by fused-silica glass wedges. The details of the components can be found in the main text.

strong-field process based on light-matter interaction and can intuitively be explained as follows. The refractive index n of a laser propagation medium depends in second-order on the laser peak intensity I. Since for a pulsed laser the peak intensity is time-dependent, this time dependency will be imprinted on the refractive index, i.e., $n = n(t) = n_0 + n_2 I(t)$. As described in the theory chapter, this index enters in the phase term of the pulse's electric field and changes the wave vector $k = k_0 n(t) = k(t)$. All time dependencies in the phase can be attributed to the frequencies of the pulse. Thus, in the rising and falling edge of the laser pulse, when the refractive index is strongly time-dependent, new frequency components are added spectrally to the left and to the right of the incident spectrum. Self-phase modulation contributes mainly to the frequency adding. However, effects like HHG, multi-wave mixing, or cross-phase modulation can also take place. The reader can consult the reference [93] for more details about these different processes.

Self-phase modulation is efficient for intense pulses. To increase the intensity of the output pulse of the NIR laser, it is focused into the helium gas medium by a focusing mirror. In order to avoid possible beam astigmatism due to the focusing optics, the beam is folded before entering the fiber setup. The purpose of the hollow-core fiber is to guide the laser beam on a small beam waist, i.e., with high intensity, and avoid its divergence after the focus. Thereby, it increases the interaction length for the self-phase modulation. The fiber is a glass capillary, which is a 1.5 m long and has a 310 µm inner diameter core, where the laser beam is reflected inside at the cladding. It is put on a stiff but lightweight construction rail to prevent any bending of the fiber, which would lead to losses of beam energy. Furthermore, it is mounted inside vacuum tubes to guarantee an only rare-gas-filled environment. The laser beam enters and exits the tubes through Brewster-angled glass windows. The laser focus position in propagation direction and possible residual astigmatism can be fine-tuned by a remotely controlled slightly biconvex lens located in front of the grating compressor inside the NIR laser.

For the conversion medium in the fiber, the rare gas helium is used. Helium has a high ionization potential, which makes it robust against ionization. However, if using a static helium pressure inside the system, the high intensities at the laser focus could still lead to high plasma creation at the entrance and at the output of the fiber. The plasma could either destroy the laser focus, which would lead to less efficiency for the fiber coupling, or could lead to sputtering by charged helium fragments and thereby degradation of the fiber cladding. In order to reduce the plasma, the vacuum tubes are pumped from both sides below 10 mbar, while a constant gas pressure of about 2.5 bar is supplied in the middle of the fiber. With this, the gas medium enters the fiber core through a small crack in the cladding of the fiber and flows towards the ends of the fiber, where the gas is pumped out so that a static pressure gradient to both sides is formed. In order to prevent any other gas flows except through the fiber core, the vacuum tube system is split into three sealed segments. The fiber is threaded

through small holes in the vacuum flanges and glued onto them by a sealing paste (Torr Seal).

The benefit of this doubly differentially pumped hollow-core fiber system is the spectral broadening of the pulse to an optical octave-spanning spectrum combined with high output power while avoiding distortions of the laser beam profile. With proper spatial alignment of the system, a power output efficiency of more than 55 % is reachable, meaning by using 9 W input laser power, 5 W output power can be expected. Some beam energy is lost at the transient points, i.e., at the input and output of the fiber and at the crack in the middle. To minimize the loss, one has, in particular, to take care of the production of the crack. It is realized by cutting the fiber into two halves with a glass cutter and stacking them back together without a visible gap.

The attainable output beam profile depends on the batch in the fiber production process. In an ideal case, the fiber supports only the transverse electromagnetic mode of the lowest order (TEM_{00}) when the laser propagates through it while suppressing all higher orders. However, the output mode is always a mixture of different modes, whereby the lowest order should dominate. In order to achieve this, one has to slightly tilt the fiber with respect to the laser propagation direction in the alignment procedure. Furthermore, while stringing together the two fiber parts, one has to take care that a desirable output beam mode is supported after cutting. Figure 3.3 shows an example of the far-field beam profile for an uncut fiber in a) and after cutting and aligning the same fiber in subfigure b). Both profile images show an almost round intensity profile except for some slight changes. Figure 3.4 a) shows a photographic picture of the

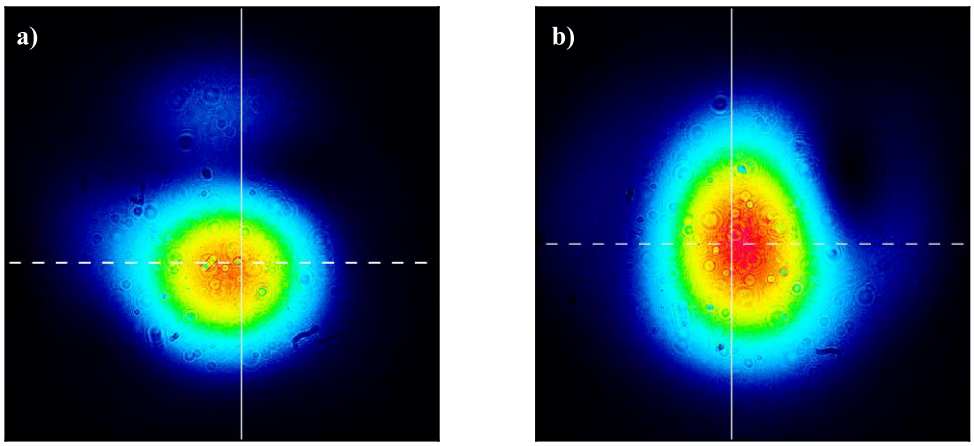

Figure 3.3: Camera pictures of the beam profile in the far field of the hollow-core fiber output, where the color-coding shows the beam intensity in arbitrary units. The white solid and dashed line marks the position with the highest intensity for the vertical and horizontal direction, respectively, which are calculated by the camera software. The round interference pattern are dirt on the camera objective. a) The beam profile before fiber cutting. b) The beam profile after cutting. Despite some small deviation an almost round mode is achievable before and after cutting.

laser beam propagating through the cut point of the fiber. The red light is caused by scattering of the laser beam in the fiber resulting in a loss of the output power.

The achievable broadening of the spectrum depends on the gas pressure applied in the middle of the hollow-core fiber system. Figure 3.5 shows obtainable spectra for different incident helium pressures, which are recorded at the far-field of the fiber output by a flexible visible light spectrometer (USB2000+ by Ocean Optics). The higher the helium pressure, the broader is the spectrum, and the greater is the shift of the central wavelength towards lower values. Higher pressures than 2.6 bar would lead to even broader spectra. However, then the output power efficiency rapidly decreases, the beam mode starts to become distorted, or the focus shifts due to changes in the refractive index caused by the helium. For an optimal fiber setup, one has to make a tradeoff between the helium pressure and the spatial alignment of the system in order to simultaneously achieve high output power, broad spectrum, and an acceptable output beam profile. In the end, the divergent output laser beam is collimated by a convex mirror that is again in a folding geometry in order to avoid possible astigmatism. The collimating mirror is mounted on a micrometer translation stage and therewith provides access to fine-tune the divergence of the beam at the entrance of the attosecond beamline, where the beam is focused again.

The self-phase modulation process and the propagation in air imprint a positive chirp onto the spectral phase of the laser pulse. For a rule of thumb, one meter of air results in GDD of about 35 fs^2 at a wavelength of 800 nm. To compensate for this

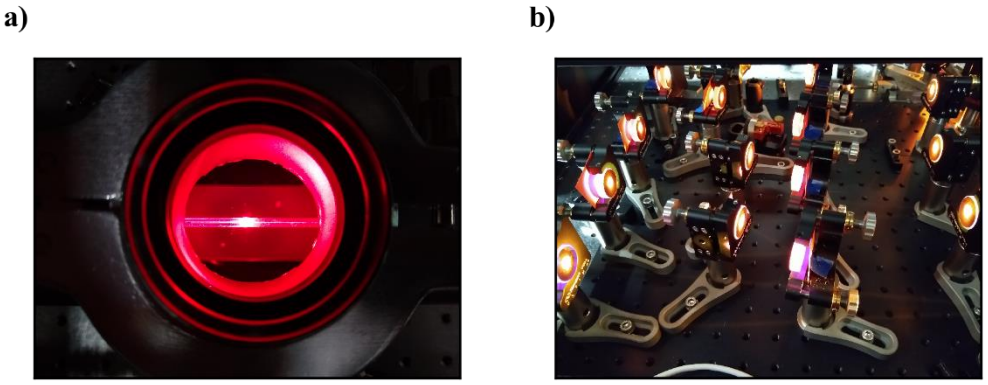

Figure 3.4: Photographic picture of the experimental setup for the pulse compression to the few-cycle of the electric field carrier. a) The cut of the hollow-core fiber with the laser pulse propagating through, which is observed through an optical view port. The red light is present due to the scattering of the pulse on the cladding of the fiber and at the cut position. b) The array of chirped mirrors with the laser beam hitting each mirror in its center. The faint trace of the beam propagation path is visible due to scattering at air molecules.

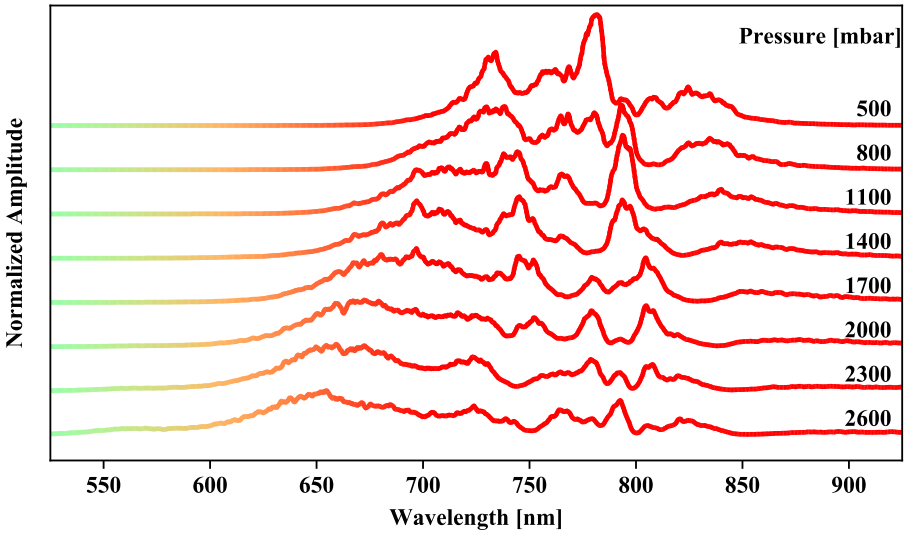

Figure 3.5: Example of normalized spectra of the near-infrared laser pulse after spectral broadening in the doubly differentially pumped hollow-core fiber for different incident helium pressures. The higher the pressure the broader the spectrum and the lower is the central wavelength.

chirp and therewith compress the spectrally broadened pulse in time, the beam is directed through a chirped mirror compressor. It consists of an array of five or seven pairs of broad-band dispersive mirrors (PC70 by UltraFast Innovations). During the reflection of the beam by the mirrors, different wavelengths of the pulse have different penetration depth into the mirror's multi-layer coating resulting in a wavelength-dependent propagation path length. With this, each pair of mirrors introduces a net GDD of -40 fs^2. Figure 3.4 b) shows a photographic picture of the chirped mirror compressor while the laser beam is reflected back and forth. The mirror coating is designed for a certain angle of incidence of 5° and 19° for a pair, respectively. Thus, in the alignment procedure, one has to take care that the beam propagation direction adheres to this angle; otherwise, the compressor could add higher orders of spectral dispersion onto the pulse. Furthermore, depending on the exact experimental condition and therewith the additional dispersive components needed further downstream for a specific experiment, one can guide the beam either through five or seven pairs of chirped mirrors. By doing so, the compressor provides flexibility for several demands of negative dispersion.

In front of the compressor, the laser beam passes a pair of fused silica glass wedges with a 4° apex angle. The wedges are mounted on remotely controlled translation stages. With the help of the wedges, one can fine-tune the total spectral dispersion such that the shortest pulses are generated at the target position of the attosecond beamline. The positioning of the wedges before the compressor helps to avoid laser-induced damages in the glass, since here, the pulse is still stretched in time due to the dispersion that is accumulated in the fiber. After the whole broadening and

compressor stages, the typical pulse specification is a pulse duration below 5 fs, i.e., a few-cycle pulse, with a pulse energy greater than 1 mJ at 3 kHz repetition rate.

Measuring and Controlling the Time Shape of the Pulse

For the measurement of pulse duration on the order of femtoseconds, usual electronic devices like light sensors are unsuitable because their response time is in the nanosecond timescale, and therewith they are six orders of magnitude slower. Instead, a process is needed, which is on the same timescale or even faster. Since nothing shorter than the pulses themselves are commonly available in a laser laboratory, they are used to measure their own duration. However, a straightforward light-light interaction does not exist, and therefore the common measurement technique for ultrashort pulses uses a nonlinear medium. Here, the pulse is often split into two or more copies and focused onto the medium producing an electromagnetic wave signal with new mixed frequencies. A workhorse realization of this kind of measurement technique is the optical autocorrelator. Here, the new wave signal is recorded while scanning an introduced time delay between two copies of the incident pulse. In doing so, one can retrieve the incident pulse in the time domain by the time trace of the new signal.

Although the autocorrelator method produces reliable results for optical pulses with relatively long durations, it fails for few-cycle pulses because then the autocorrelation trace becomes ambiguous [94]. As discussed in the fundamentals chapter, an ultrashort pulse can be expressed by its amplitude and phase in the time or in the frequency domain, whereby the Fourier transformation links both domains. Thus, by measuring the spectral amplitude and phase, one can completely retrieve the time shape of the pulse. Several optical techniques using measurements in the spectral domain have been developed in the last decades like frequency-resolved optical gating (FROG) [95], spectral-phase interferometry for direct electric-field reconstruction (SPIDER) [96], or dispersion-scan (D-Scan) [97,98]. For the characterization of the pulses used in this thesis, the D-Scan method is used.

In the D-scan setup, a second harmonic (SH) signal of the broadband pulse is generated in a beta-barium borate (BBO) crystal while scanning the GDD of the pulse. The dispersion of the pulse is controlled by moving the glass wedges introduced in the previous section and thereby changing the thickness of glass material the pulse has to propagate through. The spectrum of the SH is then recoded by a flexible high-resolution UV fiber spectrometer (HR4000+ by Ocean Optics) for different glass insertions. Figure 3.6 c) shows an example of a spectral trace of the SH signal. Here, for a certain wedge position (around 0 mm in the relative scale), the spectrum of the SH becomes broad and narrows again for more or less glass insertion,

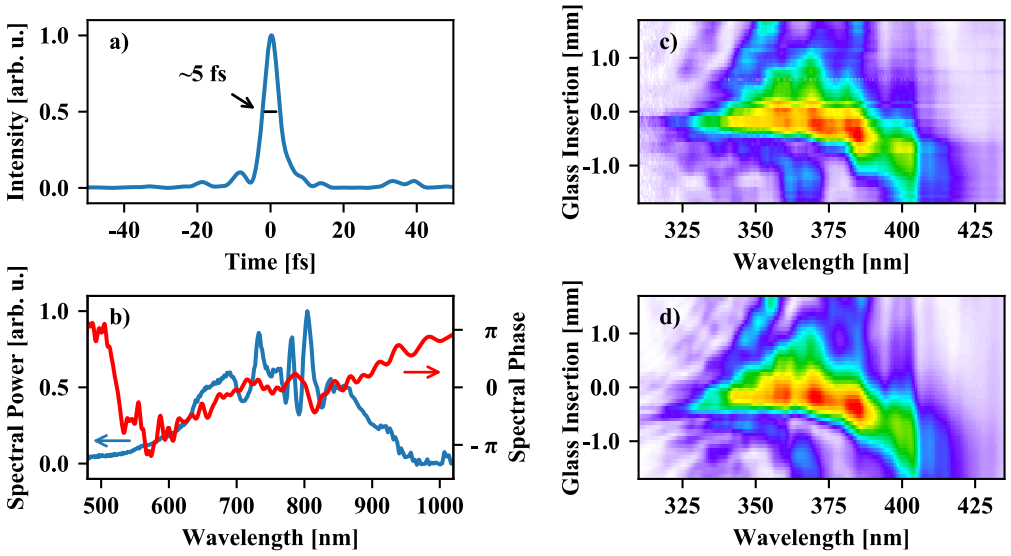

Figure 3.6: Measurement of the pulse duration of the few-cycle near-infrared laser pulse by the dispersion scan (D-Scan) method. a) The shortest retrieved temporal shape of the pulse intensity achievable for the best glass wedge position. The full width at half maximum results in 5 fs. b) The measured intensity spectrum of the laser pulse and the retrieved spectral phase for the best wedge position. c) The measured D-Scan trace, which is the intensity spectrum of the second harmonic of the laser produced in an nonlinear beta-barium borate (BBO) crystal for different glass insertion of the wedge and therefore different dispersion on the laser pulse. d) The retrieved D-Scan trace from a iterative algorithm that tried to recover the measured trace. The trace is obtained after 15000 iterations and by this the spectral phase together with the time shape of the pulse is calculated, which are shown in a) and b).

i.e., more or less dispersion. At the position where the broadest spectrum is obtained, the introduced GDD is such that the shortest pulse is generated at the BBO-crystal.

The expected result of the D-Scan trace can be expressed by an analytical formula that incorporates the intensity spectrum and the spectral phase of the fundamental NIR pulse given by [97]

$$\tilde{S}(\omega, z) \propto \left| \int_{-\infty}^{+\infty} \left[\int_{-\infty}^{+\infty} \tilde{F}(\omega') e^{ik(\omega')z} e^{i\omega' t} \, d\omega' \right]^2 e^{-i\omega t} \, dt \right|^2 . \qquad (3.1)$$

By using a measured fundamental spectrum, see figure 3.6 b) and the analytical formula, the spectral phase of the NIR pulse can be retrieved by an iterative algorithm. Hereby, a randomized spectral phase is initialized, and an expected D-Scan trace is calculated. This simulated D-Scan trace is then compared to the measured one, and an error signal is produced, whereby the initial spectral phase is iteratively adapted. More details about this iterative retrieval algorithm can be found in the references [99–101]. Figure 3.6 d) presents the retrieved D-Scan trace after 15000 iterations, which fits well with the measured trace in c), and in b), the corresponding spectral phase of the fundamental light pulse is shown in red. Using this phase and the previously recorded fundamental spectrum, the time shape of the

pulse can be calculated. Figure 3.6 a) shows the pulse intensity in time for the dispersion setting, the wedge position, which generates the shortest pulse. A main peak with a full width at half maximum (FWHM) around 5 fs is observed.

In the retrieved temporal shape of the pulse, some small satellite pulses next to the central peak are visible. In order to realize good experimental conditions, high contrast between these pulses is most often desired. The appearance of the satellites results from orders of the spectral phase higher than the GDD, which is accumulated in the pulse during its propagation through air, the laser setup, the fiber, and the chirped mirror compressor. Since the glass wedges introduce only minor third or fourth-order dispersion, they are unsuitable for minimizing the strength of the satellites. However, with the Dazzler mentioned above, one can control these spectral phase orders that cause the satellite pulses [102].

This is realized by controlling either the GDD, the third-order dispersion (TOD), or the fourth-order dispersion of the sound wave applied to the acoustic optical crystal of the Dazzler. Figure 3.7 shows the retrieved pulse temporal shape from separate D-Scan traces for different Dazzler settings. In subfigure a) a small satellite pulse next to the main pulse for negative times and a second satellite around 30 fs is visible. The pulse contrast here is 7.7, which is the ratio between the intensity of the main and satellite pulse, and the retrieved pulse duration is 5 fs FWHM. By changing the applied TOD in the Dazzler settings from -361×10^3 fs^3 to -358×10^3 fs^3, the contrast can be enhanced to 13.0, and the pulse duration can be suppressed down to 4.7 fs

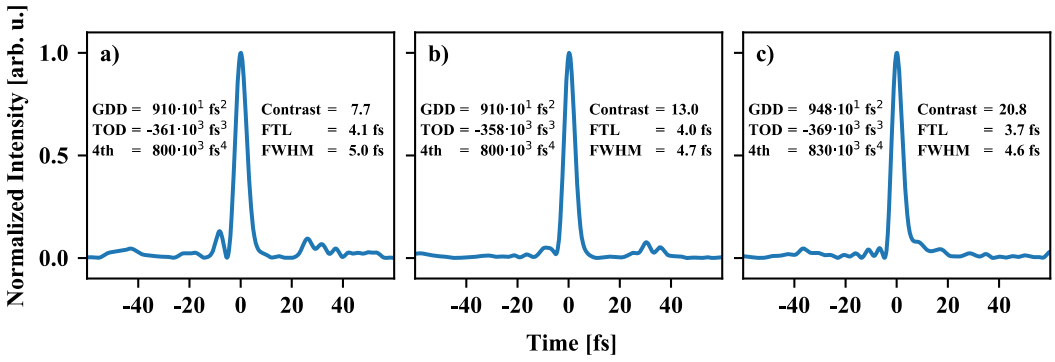

Figure 3.7: Temporal shapes of the few-cycle near-infrared laser pulse intensity for different settings of the Dazzler. The respective dispersions on the sound wave applied to the Dazzlers crystal are shown on the left side of the pulse. a) Next to the main peak the pulse shows small satellites as a pre (at ~-10 fs) and post-pulse (at ~30 fs). The contrast, i.e., the division of the main pulse amplitude by the greatest satellites pulse amplitude, results in only 7.7. b) By changing the third-order dispersion (TOD) on the sound wave of the Dazzler compared to the settings in a), the contrast increases to 13. Furthermore the pulse duration in full width half maximum (FWHM) decreases from 5.0 fs in a) to 4.7 fs. c) Changing iteratively the TOD, the group delay dispersion (GDD) and the fourth order dispersion, one can almost suppress all satellites and results in a contrast above 20 and a FWHM pulse duration of 4.6. Since the Dazzler is located before the hollow-core fiber, the change of the settings influences the broadening behavior such that the intensity spectrum supports a Fourier transform limited pulse (FTL) of only 3.7 fs.

FWHM, see subfigure b). Note that the change of the dispersion given by the Dazzler is applied on the pulse inside the NIR laser and therewith before the spectral broadening by the fiber and the temporal compression by the chirp mirror array. Thus, the change in the dispersion here propagates with the pulse through the whole pulse compression stage. Furthermore, the change of the dispersion in the laser also changes the temporal shape in front of the hollow-core fiber, and thereby it influences the self-phase modulation in the fiber, which can lead to differences in spectral broadening and throughput efficiencies. The shortest pulse achievable by a given spectrum is the Fourier transform limit (FTL) pulse, which is obtainable if one Fourier transforms the pulse spectrum assuming a flat spectral phase. Therefore, the pulse duration changes from 4.1 fs in subfigure a) to 4.0 fs in subfigure b). Further compression of the pulse duration and contrast enhancement is achievable by also changing the fourth-order dispersion. Subfigure c) shows an example of a 4.6 fs pulse with a contrast of 20.8 between the main peak and the satellites for an almost optimal Dazzler setting. Although one can change the GDD of the pulse by the wedge position in principle, the change of the GDD by the Dazzler here is applied in order to compensate for the changes in the other orders and thereby increase the spectral broadening in the fiber as mentioned above.

Carrier-Envelope Phase Stabilisation

The carrier-envelope phase (CEP) of a laser pulse describes, as mentioned in the fundamentals chapter, the phase slippage between the carrier and the envelope of the pulse's electric field. Hence, in the case of an ultrashort laser pulse, in particular, for a few-cycle pulse, the CEP strongly determines the maximum strength of the electric field. For a CEP of 0 or π the absolute value of the electric field is higher at the point in time with maximal field envelope than the electric field at any moment of a pulse with a different CEP. Thus, processes that are sensitive to the electric field of a laser pulse, for instance, the high harmonic generation, strongly depend on the CEP. In this thesis, the ionization gating technique is used to produce almost isolated attosecond pulses and therewith a broad continuous harmonic spectrum. Taken together, for stable and reliable experimental conditions, enhancement of the high-harmonic yield, and good harmonic spectral properties, one needs to control and stabilize the CEP at the light-matter interaction point.

As discussed in the section about the generation of ultrashort NIR pulses, the fast fluctuation of the CEP in the oscillator's cavity is stabilized by the feed-forward method using an acousto-optic frequency shifter. However, it cannot stabilize all long term drifts of the CEP due to, for instance, thermal or air pressure fluctuation, which are accumulated during the propagation of the pulse on the whole optical table. For this purpose, a second CEP stabilization module is used.

The module consists of an f-2f interferometer for the CEP measurement [103,104] and a piezo-driven glass wedge to change the CEP. The measurement is performed close to the entrance of the attosecond beamline. Figure 3.8 a) shows a picture of the measurement setup with red arrows indicating the laser propagation direction. The laser beam enters the setup from the bottom by a periscope, and it is focused by a spherical mirror into the conversion medium for high harmonic generation in the beamline. The entrance is a fused-silica glass window with a 45° angle of incidence. The most power of the beam is transmitted through the glass into the beamline, and about 1 % is reflected to the next pick-up mirror. Reflections occur on both surfaces of the window so that a double pulse in time is created. In order to obtain a clean interference signal in the f-2f interferometer, one thus has to block one pulse. The most convenient point to do so is the position of both beam foci because here, they are clearly separable. In the setup, the back of the steering mirror SM1 serves as the blocking material. After the focus in air, the divergent beam is collimated by a second spherical mirror to allow a convenient alignment of the beam into the interferometer using the steering mirrors SM1 and SM2.

In the f-2f interferometer, a second harmonic signal of the fundamental pulse is produced in a BBO, which is aligned with respect to the beam in order to achieve

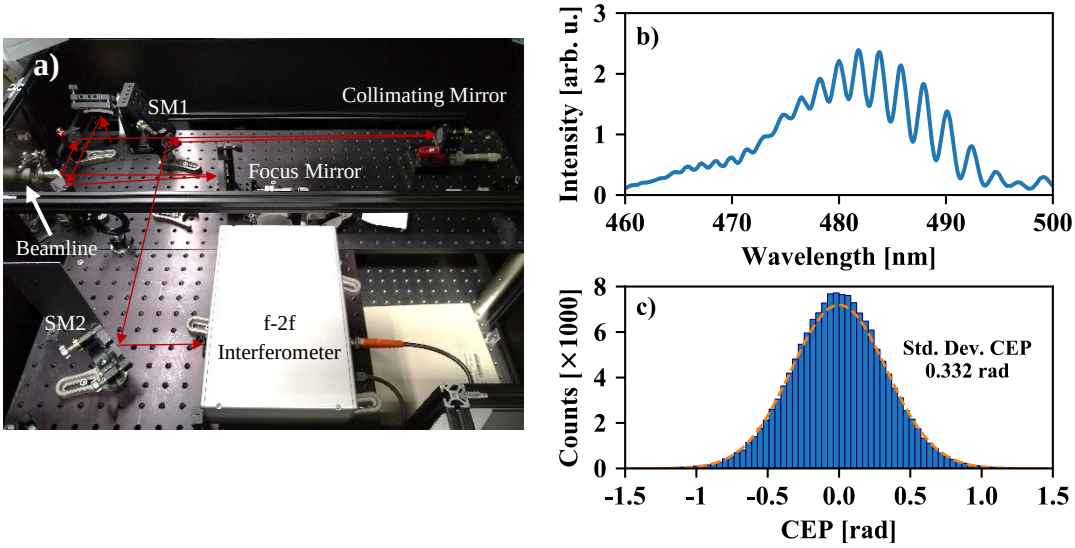

Figure 3.8: The carrier-envelope phase (CEP) stabilization of the few-cycle near-infrared pulse in front of the attosecond beamline. a) The experimental setup to measure the CEP by an f-2f interferometer. The red arrow indicate the laser propagation direction. In order to measure the CEP close to the high-harmonics generation point, the weak reflection on the entrance window to the beamline is used for the measurement. The components are discussed in the main text. b) An example of the interference pattern recorded by the f-2f interferometer. The position of this pattern in wavelength direction has to be controlled in order to stabilize the CEP. c) A histogram of the stabilized CEP for several hours. The stabilization is achieved by moving a piezo-driven wedge in the near-infrared laser (not shown). The deviation from the target CEP of 0.0 rad is normal distributed. A fit by a Gaussian fit function (orange dashed curve) results in a standard deviation of the CEP of 332 mrad.

good phase-matching conditions. The spectrum of the fundamental spans at least an octave so that if one overlaps the fundamental with the second harmonic signal, spectral interference appears, which is recorded by a spectrometer. Figure 3.8 b) shows an example of observable interference fringes. The spectral position of the fringes is linked to the carrier-envelope offset frequency of the pulse train, which, in turn, is proportional to the CEP. By measuring the spectral phase of the fringes using Fourier transformation, one thus can deduce a relative value for the CEP.

Deviations from a desired value for the CEP are used as an error signal to feed a proportional-integral-controller. The controller applies a specific voltage to a piezo accumulator that moves a dispersion glass wedge, which is placed in the stretcher stage inside the NIR laser. Since the attosecond beamline is evacuated, the change of the laser pulse's CEP inside the beamline is negligible. Thus, placing the measurement part directly before the beamline and the controlling part in the NIR laser has the benefit that all CEP fluctuations, which are accumulated during the whole pulse propagation through the amplifier, the hollow-core fiber, and the chirped mirror compressor, can be compensated at once and this without any additional disturbance factor, see also reference [105]. The piezo-controller and the spectrometer are both triggered by a fraction of the laser’s repetition rate in order to stabilize the CEP on a synchronized shot to shot basis. Figure 3.8 c) shows a histogram of a stabilized CEP measurement under typical laser performance conditions. A fit on the histogram by a Gaussian function results in a CEP standard deviation of only about 330 mrad.

The Attosecond Beamline

The attosecond beamline is the core of the experimental setup. Here the attosecond pulse is produced and overlapped spatially and temporally with the (NIR) femtosecond pulse. Both pulses are focused together on the target of investigation. By scanning an applied time delay between the attosecond and the femtosecond pulse in an interferometric way, the quantum mechanical dynamics of the target can be studied within a time resolution on its natural timescale. Hereby, the observable is the spectrum of the attosecond pulse, which is transmitted through the target and recorded in propagation direction by a grating-based spectrometer. This measurement procedure is called here attosecond transient absorption spectroscopy.

The production of pulses on the attosecond timescale with a tabletop system is based on the generation of high harmonics of a preferentially long-wavelength laser. For this purpose, the NIR laser is focused by a spherical mirror, 1 m radius of curvature, into the conversion gas neon, argon, or xenon. The harmonics are in the XUV spectral region. Since the characteristic absorption length of an XUV pulse in air is less than 1 mm, the HHG and therewith the whole following experimental setup

is placed and has to be controlled inside vacuum chambers. A rendered computer-aided design of the whole beamline is shown in figure 3.9. For this purpose, a vacuum of about 10^{-3} mbar is enough, but due to the high gas load in the HHG and target chamber, a high pumping speed is needed. Furthermore, considering the high intensity of the laser and the high photon energy of the XUV pulse, a vacuum below 10^{-8} mbar can increase the lifetime of the optical components in the beamline, which otherwise would lead to the deposition of carbon on the optical components from residual oil vapor after some time.

In the experiment, the same fundamental NIR laser pulse used for the HHG can be reused for the time-delay and/or intensity-dependent transient absorption spectroscopy measurement. This reusing provides inherent stability against timing jitter between both pulses since the XUV pulse is phase-locked to the NIR pulse due to its production process. Here, the propagation paths of both pulses are then the same, and the interferometer geometry is a line of the two collinear pulses. Since the NIR pulse and XUV pulse are defined in different spectral regions, they have a different divergence after the focus for the HHG [38]. This difference is exploited in the experimental setup in order to separate the two pulses in time and space and control the intensity of the NIR pulse.

A schematic view of the realization of the pulse manipulation is shown in figure 3.10. The NIR pulse is focused into a machine-drilled pinhole of an HHG-

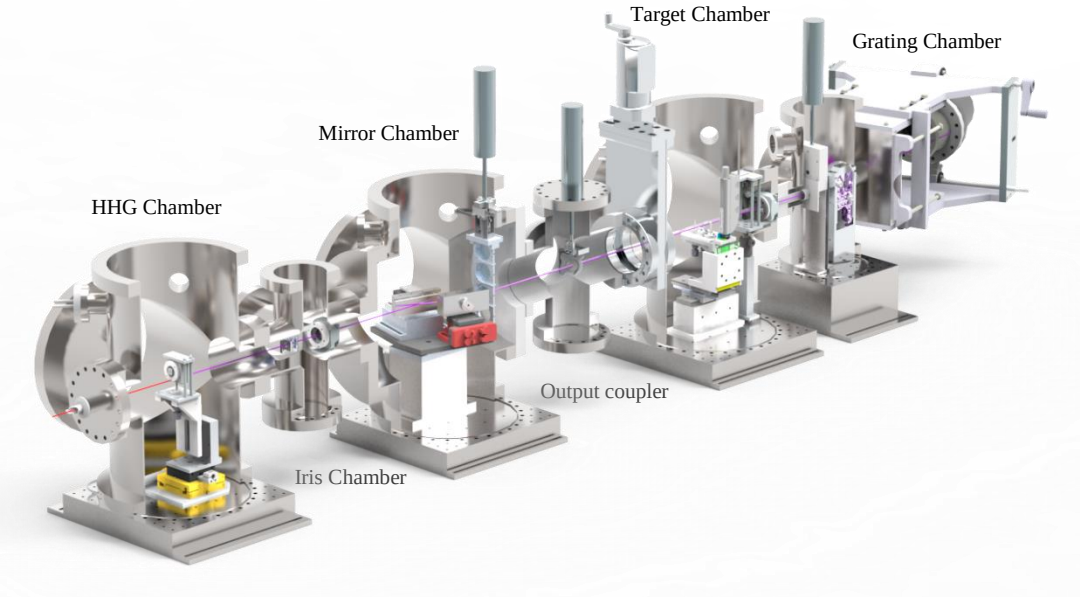

Figure 3.9: Computer-aided design of the attosecond beamline. The whole setup is placed inside vacuum. Each optical component for the manipulation of the pulses, the target of investigation and the grating-based spectrometer are located in separate vacuum chambers in order to realize differential pumping between the points with high gas load, i.e., the high harmonic generation (HHG) and target chambers and the optical component, in particular in the mirror and grating chamber. Details about the purpose of each components can be found in the main text. The figure is adapted from reference [85].

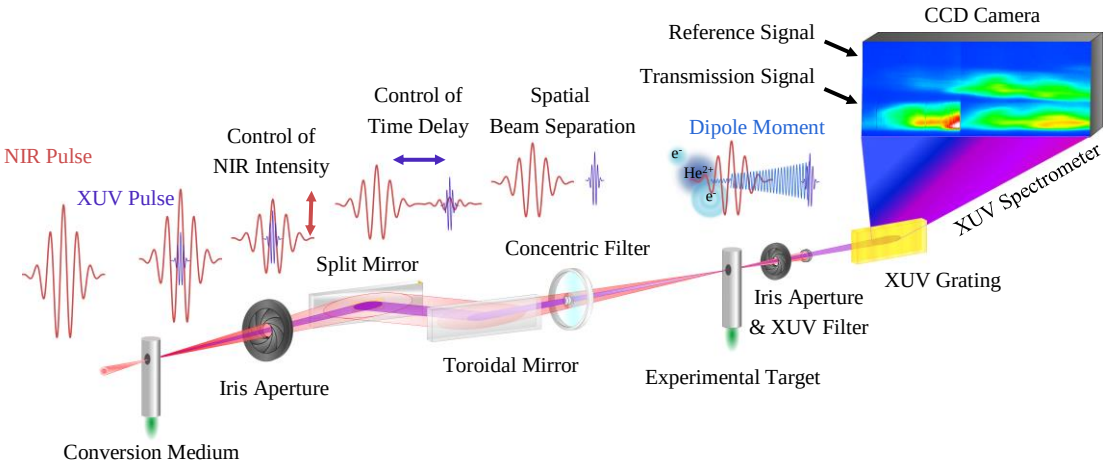

Figure 3.10: A schematic setup of the attosecond beamline. The near-infrared (NIR) pulse and the extreme ultraviolet (XUV) pulse are both focused into a helium target. The XUV induces a decaying dipole moment in the target, which is manipulated by the NIR pulse. The different manipulation stages to perform the experiment are indicated. They are the control of the NIR intensity by an iris aperture, the control of the time delay between the NIR and XUV pulse by a split mirror, their focusing by the toroidal mirror, their spatial separation by a concentric band-pass filter, and the recording of the XUV spectrum by a grating-based spectrometer. An example of the XUV transmission and *in situ* reference signal recorded by the spectrometer camera (CCD) is shown. The figure is adapted from reference [85].

conversion-gas-filled ceramic tube. The 3 mm thick tube helps to apply a local gas pressure up to hundreds of mbar without venting the whole beamline. The gas flows out of the tube through the pinhole with a 100 or up to 300 µm inner diameter and is pumped out by a turbo-molecular pump (HiPace 2300 by Pfeiffer Vacuum) that is flanged on top of the HHG chamber. A constant flow of gas has the advantage that the conversion medium is always renewed after its ionization by the NIR laser. Together with a stabilized gas pressure supply, this provides a constant path-length density for the laser. For the tube, the ceramic Macor® is used due to its mechanical resistance, where otherwise a material like stainless steel could melt and be cut under the high field intensity in the laser focus in the alignment procedure. Remotely-controllable motorized translation stages help to align the gas tube with respect to the position of the focus in the direction of the optical axis to achieve optimized phase-matching conditions for the HHG and in the direction perpendicular to the optical axis for high power throughput.

A closed-loop iris with zero-aperture capability controls the intensity of the NIR pulse. It blocks parts of the NIR light, whereby the collinearly propagating XUV pulse is not affected due to its smaller divergence. The steps in the closing of the iris are not linear to the NIR laser intensity change. This is because the intensity is not constant across the transverse beam profile and, in particular, considering optical beam propagation, a smaller beam waist due to the iris closing results in a greater beam waist in the focus of the target and therewith in a lower intensity. Thus, if one wants to perform intensity-dependent measurements, the NIR intensity in a certain

measurement campaign has to be calibrated. Some examples of doing so will be addressed in the next chapter.

The time delay between the NIR and XUV pulse is controlled by a split-mirror, for which an inner mirror is placed in and can be translated with respect to a fixed outer mirror introducing a different path length for each pulse. The two beams hit both mirrors in a grazing incidence angle of 15° in order to increase the mirror's reflectivity for a spectrally broadband range, in particular, for the XUV. The inner mirror is designed to reflect best the XUV pulse, and therefore it is gold-coated, and its dimension of 2 mm in height and 10 mm in width fits – considering the incident angle – the beam size of the XUV pulse. The outer mirror is silver-coated and can highly reflect the NIR pulse. The inner mirror is mounted on a piezoelectric stage (PIHera by Physik Instrumente), which can move the mirror perpendicular to its surface with nanometer precision.

Using a continuous wave helium-neon-alignment-laser (HeNe), the interferometric stability of the split-mirror can be measured. For this purpose, the HeNe is reflected on both mirrors, and the spatial interference is recorded by a camera close to a focus position further downstream. By scanning the piezo position, the intensity on a certain region of interest of the camera oscillates due to the interference between the HeNe beams that are split on the mirrors, see figure 3.11 a). The exposure time of the camera must be shorter than every integration time used for the experiment later in order to cover all parasitic frequencies, which might influence the piezo stability. The oscillation should follow a sinusoidal curve with the periodicity of the HeNe wavelength of 632.8 nm divided by the sine of the angle of incidence. Instabilities cause deviations from this periodicity in the piezo movement, which are shown in figure 3.11 b) in units of time. The standard error of this deviation results in a possible time delay resolution of 26.9 as which is only one-tenth of the typical XUV pulse duration.

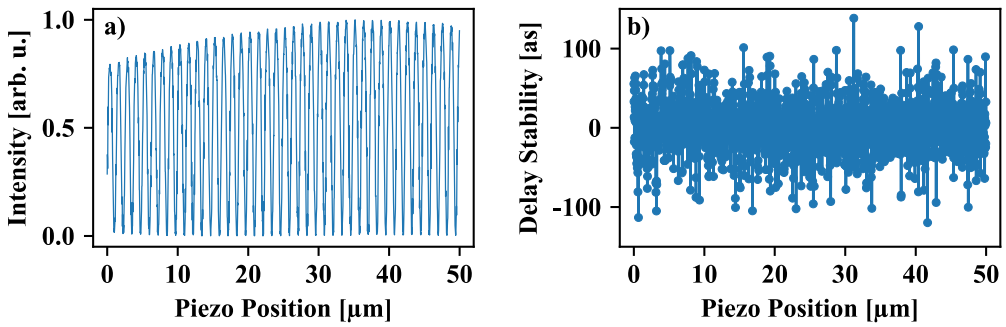

Figure 3.11: Time delay stability of the collinear interferometer geometry. a) The intensity of an interfering continuous wave helium-neon laser at a certain region of interest on the recording camera for different piezo position of the split-mirror. The oscillation period follows the wavelength of the laser considering the angle of incidence of 15°. b) Deviation of the phase from a perfect sinusoidal oscillation in a) translated in the time domain. The standard error of deviation results in 27 as stability for the time-delay scan.

After applying a time delay between the XUV and NIR pulse, both pulses are focused into the target by a toroidal mirror. With the toroidal shape, the focus in the HHG medium is mapped one to one onto the target, which minimizes possible aberration of the focus. Although the interferometer geometry provides, as shown above, high passive timing stability, the translation of the inner mirror in the grazing incidence causes a displacement of the XUV focus in the target. After simple geometrical considerations, applying 1 fs time delay results in a parallel beam displacement of about 1.1 µm. The focus size of the typical NIR beam is 80 µm and of the XUV beam about 20 µm. Thus, in a time-delay scan of an experimental run, one has to make sure that both foci are always in the spatial overlap, whereby this walk-off effect limits the maximal time-delay range to about 50 fs. Therefore, all the following experimental results are in this time-delay window. Furthermore, the parallel displacement of the XUV beam causes a time-delay-dependent shift of the recorded XUV spectrum and influences the output efficiency through the pinhole of the target tube. However, one can correct these effects in retrospect to the measurement, as will be shown in the next chapter.

Despite the different divergences of the beams on the split-mirror, a fraction of the NIR beam is still reflected by the inner, and a fraction of the XUV beam is reflected by the outer mirror, respectively. In order to get rid of these residual spectral components on the mirrors and thereby realize a total temporal and spatial separation between the XUV and the NIR pulse, a concentric filter is placed after the mirror setup, which spatially separates the NIR and XUV beams. Here a round 200-nm-thin metallic filter-foil (manufactured by Lebow) blocks the central NIR part and, at the same time, lets pass the XUV component from the inner mirror. The used species of the metals depend on the investigated photon energies. For the photon energies between 16 and 72.5 eV, the most practical to use is aluminum. For low harmonic energies between 12 and 16.5 eV, indium, and energies between 72.5 and above 200 eV zirconium can be used [106]. The spectral filter transmission of the species is shown in figure 3.12 a). In particular, indium has a low XUV transmission of below 25% and therewith strongly suppresses the harmonic signal, which makes its usage experimentally challenging. The metallic foil with a diameter of 2 mm is glued onto a home-built twisted Kapton® wire or is directly glued onto a Kapton® foil with a central hole. The foil or the wire are mounted on a 4 cm outer diameter aluminum ring, which is held in place by a variable and in vacuum movable support array, see figure 3.12 c), d), and e).

To filter out the residual XUV that is reflected by the outer mirror of the split-mirror setup, two membrane filters can be used, which are a 2 µm thin nitrocellulose (by National Photocolor) or a 7.5-micron thin Kapton® foil (by Lebow). The nitrocellulose pellicle blocks very efficiently all XUV spectral components, whereby all effects on the NIR pulse are negligible. However, it is fragile and can easily break also by the light pressure of the intense NIR pulse, which makes its handling difficult. Compared to that, the Kapton® foil is more stable, such that the foil can even serve as a supporter for the metallic filter, see figure 3.12 d). This has the advantage that no further spatial alignment between the central hole in the NIR filter and the metallic XUV filter is needed. However, the transmission of the Kapton® foil is 90%, which is measured by dividing the recorded NIR spectrum with and without Kapton in the beam path, and its spectral transmission window is limited to about 500 nm on the short wavelength side, see figure 3.12 b). Furthermore, one has to take the dispersion of the foil into account. Its group velocity dispersion (GVD) can be calculated by values for the refractive index taken from the reference [107], which is shown in figure 3.12 b). The thickness of the foil is 7.5 µm, and that leads to a wavelength-average group-delay dispersion of about 4.5 fs^2. In order to generate a short pulse in

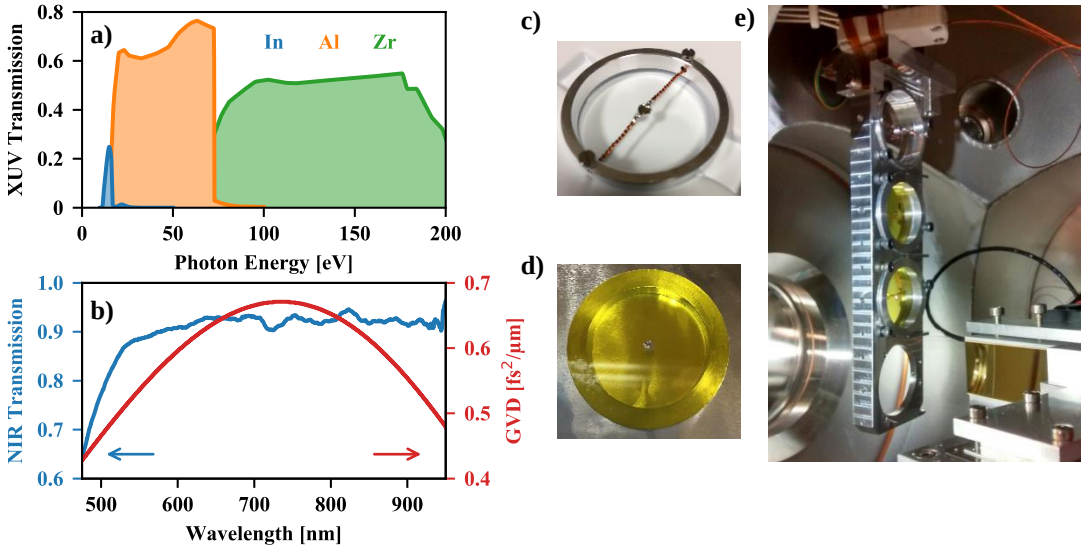

Figure 3.12: The concentric filter for the spatial separation of the near-infrared (NIR) and extreme-ultraviolet (XUV) pulse. a) Different metallic species for the 200-nm-thin transmission filter can be used for different spectral regions of the XUV from 12 eV using indium (In) to aluminum (Al) around 50 eV up to 200 eV using zirconium (Zr). b) The measured transmission and calculated wavelength-dependent group velocity dispersion of the Kapton® NIR filter. c) A metal filter glued onto a home-built twisted Kapton® wire. The wire is mounted on 4 mm aluminum ring and placed in the variable filter supporter. d) The Kapton® NIR filter with directly glued aluminum XUV filter on top. e) A photographic picture of the whole filter setup in the vacuum chamber. The supporter can hold four different concentric filters for different experimental settings and it can be moved in all dimensions inside vacuum for alignment purpose. The data for a) and b) are taken from references [106] and [107], and the pictures are adapted from reference [85].

the target, this dispersion has to be compensated for by the movable glass wedges in front of the beamline, which correspond to an additional 100 µm fused silica glass or moving the wedge on the stage by 1.4 mm. However, this additional glass also affects the NIR dispersion in the HHG conversion medium, which may influence the HHG process, and one has to make a tradeoff between the best harmonic spectrum and the shortest pulse in the target.

On the same mount for the concentric filter, a small XUV transmission grating is glued onto a Kapton® wire. The grating is a thin and 3 mm in diameter wire grid that is commonly used for transmission electron microscopy (TEM). Its wire spacing is such that it diffracts the XUV beam into different spatial orders and, at the same time, lets the NIR beam almost unaffected. Figure 3.13 shows a photographic picture of the TEM-grid and the diffraction pattern for a green alignment laser. The zeroth order of the diffraction is focused into the target, and its transmission spectrum is recorded

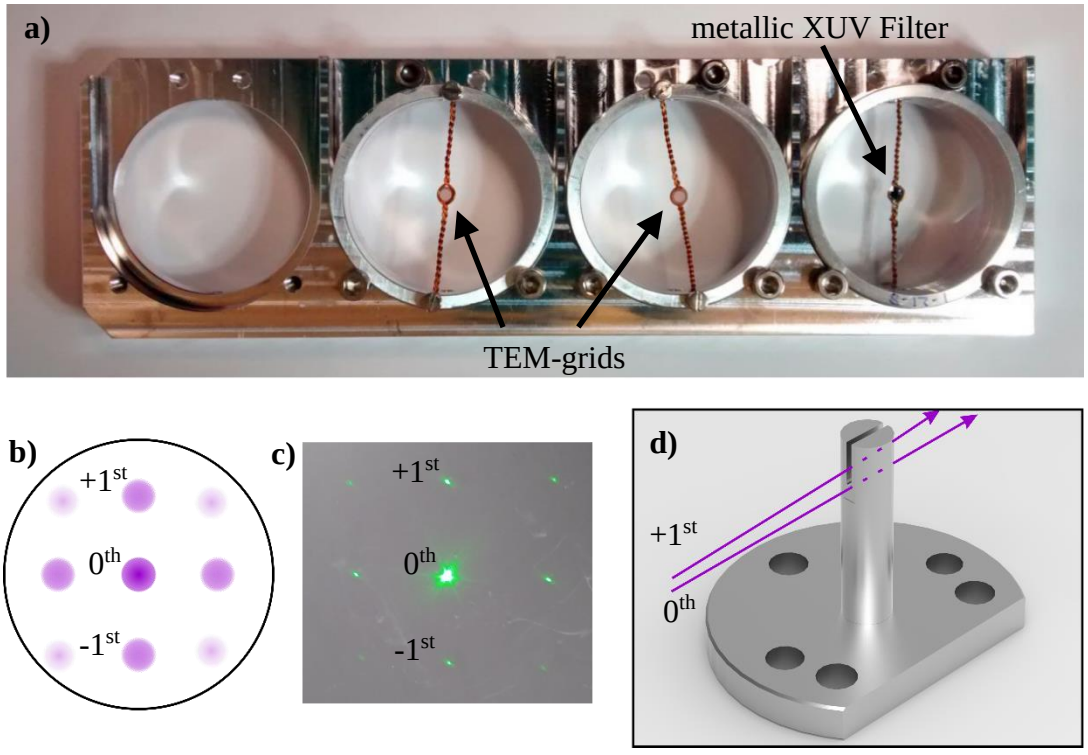

Figure 3.13: Functionality of the XUV diffraction grid for the *in situ* XUV reference. a) The transmission electron microscopy grids (TEM-grids) are glued onto home-built Kapton® wires and mounted on the variable supporter of the concentric band-pass filter array. The shown grids have a different grid spacing used for different XUV spectral regions. b) The modeled spatial diffraction pattern in the view of the laser propagation direction. c) Photographic picture of a diffraction pattern of a green alignment laser propagating through the TEM-grid and blocked on a laboratory wall. The achieved pattern reproduces well the modeled one. d) A computer-aided design of the target tube. The 0^{th} order diffraction propagates through the target pinhole while the $+1^{st}$ order passes the target from above through a groove of the tube without being affected by the target gas. All other orders of the diffraction pattern (not shown) are mechanically blocked by the target tube. Some picture are adapted from reference [85].

by the XUV spectrometer further downstream. Therewith, it provides the main observable in the experiment. The first order on top passes the target and serves as an unabsorbed *in situ* XUV reference spectrum, which is recorded by the XUV spectrometer as well and, in particular, in the same integration time. As will be shown in the next chapter, this reference spectrum can be used to normalize the transmission spectrum, which is needed in order to compare the measurement results from quantum mechanical model simulations. More details about the experimental setup for this *in situ* XUV reference can be found in the references [51,85].

After passing the annular band-pass filter array and the TEM-grid, the NIR and the XUV beam are both focused on the gas target of investigation. The gas flows from a pinhole in a gas-filled Marcor® tube with a similar setup that is used for the HHG conversion medium. After the target the NIR is filtered out by a second metallic filter protecting the following XUV spectrometer from stray light or light-induced damage. Due to the fabrication procedure, the metallic filters have small microholes producing small NIR leakages through the filters. In order to minimize these leakages and therewith decrease the integration background in the XUV spectrometer, a stack of two filters is used.

The dispersive element of the spectrometer is an aberration-corrected concave grating (by Hitachi) with a variable groove density. It provides a flat-field spectroscopic image, which is recorded by a back-illuminated thermo-electrically cooled camera (CCD, PIXIS 400B by Princeton Instruments). The grating compensates the disadvantage of conventional gratings, which generate an image on a Rowland circle and thereby cause aberrations if flat cameras record the spectrum. With this grating and the above-mentioned camera, one can measure the XUV spectrum with a resolving power of up to 1500.

For XUV energies of interest between 10 and 100 eV, two gold-coated Pyrex gratings are used. The first has 1200 grooves per mm on average and is used for wavelengths from 11 to 62 nm corresponding to about 20 to 112 eV photon energy. The second has 600 grooves per mm on average with increased efficiency for wavelengths between 22 to 124 nm corresponding to 10 to 56 eV. Both gratings are stacked onto a variable home-built stage, allowing to switch between the gratings under vacuum conditions remotely. Each grating is mounted on a mirror mount to provide access to separately tune their position and angle of incidence for high diffraction efficiency and resolution [27].

The here presented components of the attosecond beamline are sufficient to perform a transient absorption experiment. In the following, two further upgrades of this beamline will be presented, which were conducted as part of this dissertation.

Time-Delay Interferometer with Circular Polarization

In the attosecond beamline, the NIR pulse used for the HHG is reused as a (strong) perturbing laser field for transient absorption measurements. With this, high passive time-delay stability can be achieved. However, a drawback is the previously discussed walk-off of the XUV beam when scanning the time delay, which in turn limits the accessible time-delay range to about 50 fs. Furthermore, the collinear propagation geometry hinders additional manipulations on the NIR pulse, like its temporal shape or polarization, since both would affect the HHG as well. In particular, if one wants to perform experiments with circular NIR polarization, the HHG process would break down because it critically depends on the ellipticity of the driving pulse [108]. Changing the NIR polarization after the HHG is, in principle, possible; see, for instance, reference [109]. However, considering the used NIR pulse durations of below 5 fs, standard optical components to do so would introduce too much dispersion to realize short pulses in both the high-harmonics conversion and the target medium. In order to get access to longer delay ranges and different polarizations, the NIR beam can be split before and recombined within the beamline.

Figure 3.14 shows a sketch of a realized experimental setup. Here, the NIR beam impinges on a glass anti-reflection coated beam splitter, which reflects 30% of the beam's power. The residual transmitted power is used to generate high harmonics, and the reflected part passes some manipulating optical components and enters the beamline from a separate optical access port. Both interferometer paths recombine inside the vacuum beamline by a mirror with a 2 mm central hole drilled under 45° with respect to the reflective surface. The XUV pulse produced in the HHG medium can pass the mirror through the hole without being affected due to its small divergence, while the mirror substrate blocks parts of the generating fundamental NIR. The NIR, which is reflected by the beam splitter, is reflected by the hole mirror under 45° and propagates afterwards collinear with the XUV beam. Due to the central hole, the NIR beam profile obtains a donut-shaped mode, which is, nevertheless, similar to the mode after the concentric band-pass filter. The splitting and recombination lead in total to an interferometer geometry with two separate arms that are called the HHG and the external NIR arm in the following. For each interferometer arm, the optical path length and the pulse dispersion have to be controlled in order to be able to perform a time-delay scan across the time overlap with pulses as short as possible.

The optical path length and therewith the time delay between the pulses propagating through the two arms can be scanned by an optical retroreflector in the

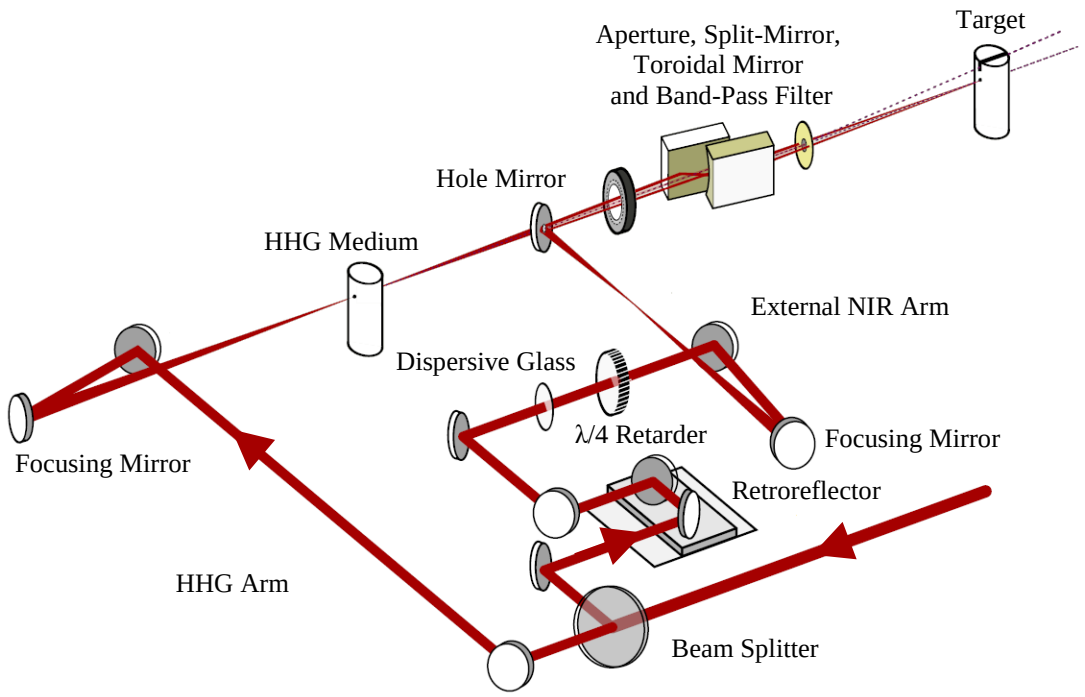

Figure 3.14: Sketch of the optical setup for the two-arm interferometer. The pulse on the HHG arm is used for the HHG while the pulse on the external NIR arm is used to perform the time-delay or intensity-dependent transient absorption experiment. The time delay between the pulses and the NIR polarization can be controlled by a retroreflector and polarization retarder in the external NIR arm, respectively. Further details of the components can be found in the main text. The drawing is adapted from reference [110].

external NIR arm. It is mounted on a piezo-driven stage (PIHera by Physik Instrumente). The stage has a travel range of 260 µm that corresponds in this geometry to a maximal time-delay range of 1.7 ps. This is much longer than the delay range of 50 fs mentioned above and can be used to investigate dynamics on a longer timescale, e.g., vibrational wave-packet dynamics in molecular targets. In order to make sure that one can scan across the time overlap, the positioning of the whole retroreflector can be aligned by an additional micrometer stage. The interferometer stability is measured again by recording the spatial interference of a continuous wave HeNe laser propagating through both arms by a fast camera. It results in a passive timing stability of ~ 350 as in full operation mode, i.e., all electronic devices and turbopumps are on. Details of the stability measurement and a reliable alignment procedure for the time and spatial overlap can be found in reference [110].

In this setup, an experiment with different NIR polarization can be performed. It is controlled by an additional broadband polarization retarder in the NIR external arm, for instance, a λ/4 wave plate depicted in figure 3.14. Hereby, one has to consider that the retarder and the optical access port to the vacuum beamline introduce additional pulse dispersion, which has to be compensated, for instance, by the positioning of the glass wedges. Additionally, a focusing of the external NIR beam is necessary in order to obtain NIR divergence properties similar to the collinear

interferometer geometry. With this, one can still make use of the following divergence-dependent components, i.e., the aperture for the NIR intensity control, the concentric band-pass filter for the spatial separation, and the aberration-free one to one focus mapping by the toroidal mirror.

To further mention, the here introduced interferometer allows realizing, additional to the used ionization gating, a gating technique for the HHG that relies on the polarization of the driving pulse such as generalized double optical gating [74]. This gating technique is not practical with the collinear interferometer geometry since the polarization-dependent temporal shape of the NIR laser used to gate the HHG would also be present in the target medium, where here a pure linear or circular polarization is often desired.

Blue-Shifts of the Near-Infrared Spectrum

The first step in HHG, as discussed in the fundamentals chapter, is the tunnel ionization of the conversion medium's atoms. This leads to an increased number of free electrons in the medium during the interaction with the intense NIR pulse. The freed electrons result in a time-dependent change of the local refractive index, which in turn changes the spectral properties of the NIR pulse when it is propagating through the medium. In the collinear interferometer geometry, the NIR pulse for the HHG is reused further downstream for the time-delay and intensity-dependent experiments. Since some features in the measurement results depend on the NIR spectrum, as will be discussed further below, one has to consider these changes in the NIR spectrum.

For low electron densities ρ_e the relative change of the wavelength λ of a certain spectral component is proportional to the time derivative of the density times the interaction path length L [111,112]

$$\frac{\Delta\lambda}{\lambda} \propto -L \frac{\partial \rho_e}{\partial t}. \qquad (3.2)$$

The minus sign effectively leads to a blue shift of the spectrum. Figure 3.15 shows the experimental setup for the recording of the NIR spectrum inside vacuum and some examples of spectra for different HHG conversion media and pressures. Here, the NIR can scatter at a remotely controlled iris aperture when it is completely closed. An in-vacuum optical fiber catches the scattered light and directs it into a spectrometer outside the vacuum (USB2000+ by Ocean Optics). The blue shift depends on the used HHG conversion medium. Using neon, almost no shift is present due to its high ionization potential of 21.6 eV and therewith low free electron densities, see subfigure 3.15 b). However, using argon or xenon with lower ionization potentials as conversion media, the blue-shift of the NIR spectrum is not negligible

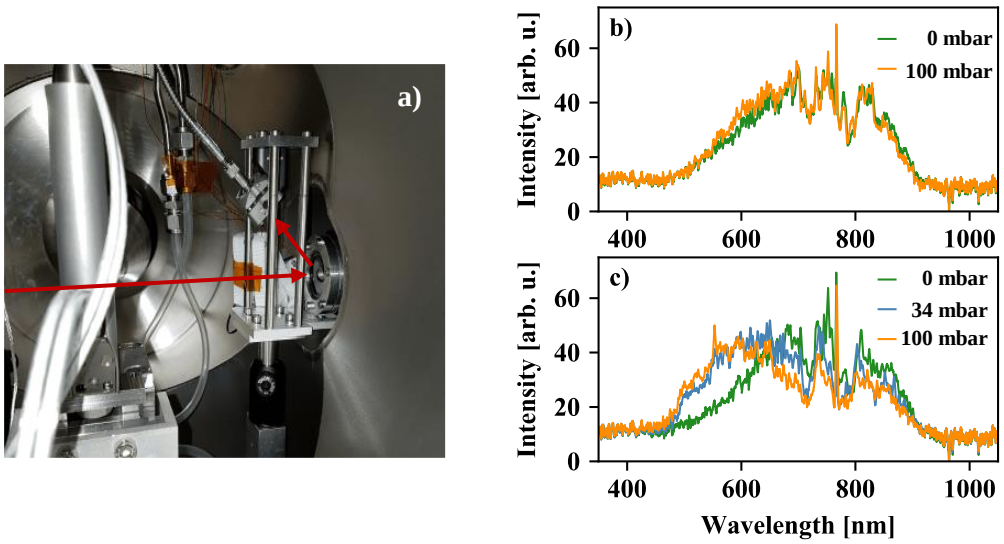

Figure 3.15: Measurement of the blue-shifted near-infrared spectrum. a) A photograph of the experimental setup for the measurement of the spectrum in the target chamber. The red arrow indicates the propagation direction of the laser pulse. After passing the target (here rear view) the laser beam hits a closed iris. The scattered light is caught by an optical fiber which directs the light into an Ocean Optics spectrometer outside the vacuum. b) The NIR spectrum in the target chamber with and without Neon as HHG conversion medium. c) The NIR spectrum for Argon as conversion medium.

even for lower backing pressures in the HHG tube, see subfigure 3.15 c). Further details about this setup can be found in reference [113].

Since the free-electron-induced change of the refractive index shifts the central wavelength of the NIR spectrum to lower values, it can also be used for wavelength-dependent measurements in the future. A possible scan parameter could be the conversion gas or its pressures to achieve different central NIR wavelengths in the target. Furthermore, the iris aperture is utilized for a pre-attenuation of the NIR power. In particular, when using the fragile indium foils for the XUV filtering before the spectrometer, the foils can break by the heating and light-pressure of the NIR beam [27]. By closing the aperture such that the low divergent XUV beam can still pass through the opening, the high divergent NIR beam can partly be blocked, and the lifetime of the filters might be enhanced.

4. Data Processing and Calibration

In attosecond transient absorption spectroscopy, the measured observable is the XUV transmission spectrum through a target medium with respect to a time-delayed strong NIR pulse. It is recorded as described in the previous chapter by a dispersive grating and an XUV camera. Here, the spectral data are collected fully automatically via a computer-aided scanning of the experimental parameters that are mainly the position of the inner mirror to scan the pulses' time delay and closing or opening of the iris-aperture to control the NIR intensity. The experimental set parameters are voltages to the piezos, which drive the inner mirror and the iris. Thus, for reliable interpretations of the spectral data, calibrations for these parameters are needed. Furthermore, since the strengths of the transmitted intensity spectra depend on the incident XUV intensity focused on the target, one typically normalizes the transmission spectrum by an unaffected reference spectrum and calculates therewith the medium's absorbance. The present chapter aims to compactly describe the main data processing steps in order to generate the results data of the transient absorption experiment with high sensitivity. The physical interpretation of the results will solely be given in the following chapters, where this chapter serves as a reference describing the methods in order not to disturb the discussion of the results.

From Transmission to Absorbance Spectra

A CCD camera with 1340 x 400 pixels records the XUV transmission spectrum, which can be translated along the image plane of the flat-field spectrum produced by the variable line-spaced grating in the spectrometer. An example of the recorded camera raw image of the transmission through helium is depicted in figure 4.1. Here, the color encodes the XUV photon counts on the camera pixels for the integration time of 4 s that is 12,000 consecutive laser shots. Due to the dispersion of the grating, the horizontal direction on the camera is approximately linear to the wavelength of the XUV pulse. The vertical direction corresponds to the spatial dimension of the XUV beam.

The signal strip between the solid black lines on the lower part of figure 4.1. is the actual transmission signal through the target medium, whereby the absorption from resonant transitions in the helium atoms are visible as sharp vertical gaps in the spectrum. The smooth changes of the signal strength along the horizontal pixel direction is the modulation of the high-harmonic incident spectrum. Due to its highly nonlinear generation processes, this spectrum changes from shot to shot. However, in the end, one wants to investigate the NIR-induced changes of the transmission

while scanning the time delay between the XUV and NIR pulse. Thus, the fluctuation of the incident harmonic spectrum will overlap with the changes of interest and thereby reduce the measurement sensitivity. Furthermore, due to the modulated spectral structure of the harmonics, the absorption signals are spectrally on a signal slope, and thereby their line shapes are slightly changed; see for both figures 4.2 a) and 4.3 c) and the discussion further below. In order to get rid of these transmission changes by the harmonic fluctuation and the modulated spectral structure, one can normalize the signal by referencing it to the harmonic incident spectrum.

For the acquisition of the reference XUV spectrum, different methods are used with method-specific advantages and drawbacks. A straightforward and simple approach is to measure the transmission spectrum with and without the target in the propagation path of the XUV pulse. However, here the recording is sequential, and due to the shot to shot fluctuation of the harmonic spectrum, one needs many spectra at one specific experimental parameter set point in order to be able to average out the fluctuations sufficiently. Therefore, long measurement times together with high long-term laser stabilities are needed, which makes this approach experimentally challenging.

A second commonly used approach is the so-called Fourier referencing. With this, one exploits that the harmonic spectrum is—for good phase-matching conditions in the generation of the high harmonics—only smoothly modulated across the XUV

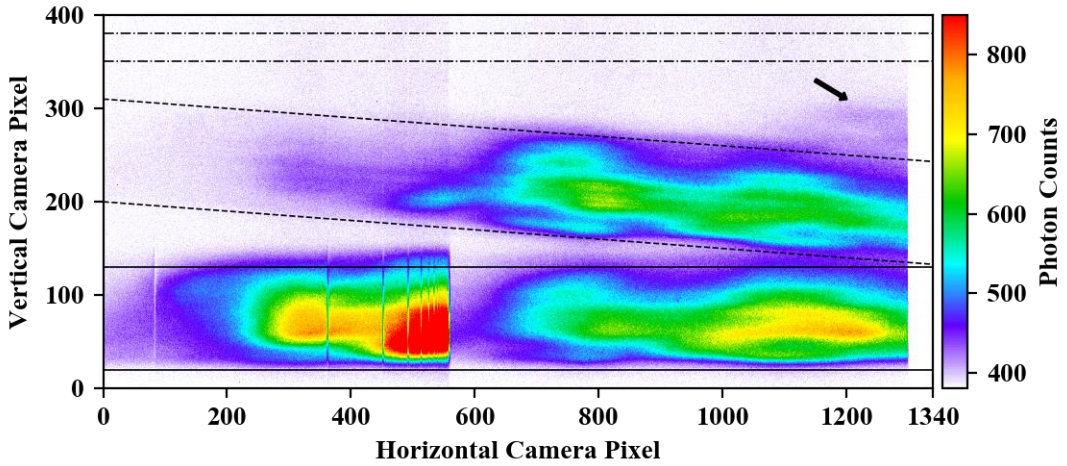

Figure 4.1: Raw camera data of the transmission spectrum of helium. The axes are the 400 x 1340 pixel of the camera, whereby the horizontal pixels are approximately linear with the wavelength and the vertical pixels correspond to the divergence of the XUV pulse beam. The color depicts the photon counts over an integration time of 4 seconds that corresponds to 12,000 consecutive laser shots. The spectrum is cut after horizontal pixel 1300 by a geometrical block in the spectrometer setup. The horizontal spectrum between the solid lines is the transmission signal through helium, where the absorption lines are visible as sharp cuts in the continuous spectrum. The skewed spectra between the dashed lines are the unabsorbed *in situ* XUV reference. An arrow indicates the appearance of the second spatial diffraction order by the TEM grid for the *in situ* reference. The region between the dashed dotted lines is used for the background determination.

wavelength compared to the sharp absorption lines. Utilizing Fourier transforming of the transmission signal with respect to the wavelength direction and using a low pass filter, one can reconstruct the XUV reference directly from the transmission in a single acquisition. While this approach provides reliable results for sharp absorption features, it fails for broad signals. In particular, it hides NIR-induced changes in the absorption in the ionization continuum since they are expected to appear with similar wavelength-dependency like the harmonic spectrum. Furthermore, the exact shapes of the absorption lines are influenced by the low-pass settings, where one has to make a tradeoff between a reliable reconstruction of the incident harmonic spectrum and reducing artifacts in the absorption spectral line shapes. This is, in particular, important for the ionization threshold since it shows a step-like increase of the absorption above the threshold and therewith corresponds to a broad signal in the Fourier domain. Therefore, the Fourier low-pass filter will partly include the Fourier signal of the ionization threshold and leave a residual absorption step in the XUV reference spectrum. More details about this method, together with the advantages and disadvantages, can be found in the references [27,57,82,85].

A third recently developed approach is the recording of the incident XUV spectrum simultaneously with the transmission spectrum in one single acquisition. The production of this *in situ* XUV reference in the experimental setup is already described in the previous chapter. Its spectrum is visible by the tilted signal strip between the dashed lines in figure 4.1. It is a weak copy of the unabsorbed transmission spectrum, and it is tilted due to the dispersion of the TEM grid, making the vertical pixel direction on the camera slightly wavelength dependent. The reference signal can be obtained by averaging between the region of interest given by the dashed lines in figure 4.1 and shown in figure 4.2. By cutting out the reference signal, one has to check that the averaged reference spectrum should not qualitatively change when slightly changing the region of interest (dashed line in figure 4.1) in order to obtain reliable results for the absorbance. In principle, one can cut out the reference signal by a region of interest that is horizontal and parallel with the camera pixels. However, this will accumulate more background noise of the camera and add artificial signals, for instance, due to the spatial second order of the TEM grid, which is not geometrically blocked and slightly visible in figure 4.1, indicated by a black arrow.

The averaged XUV transmission and reference spectra are depicted in figure 4.2 a). Here the reference is multiplied by a factor $c = 7.7$ for better visibility, whereby this multiplication factor c is determined by the diffraction efficiency of the TEM-grid, and it is slightly different after every alignment of the grid in the attosecond beamline. For its determination, the relative strength of the transmission and reference spectra can be measured without the target gas. By doing so, one has to keep in mind that the harmonic spectrum can be broad, and the second-order spectrum of the spectrometer grating may overlap with the first order transmission

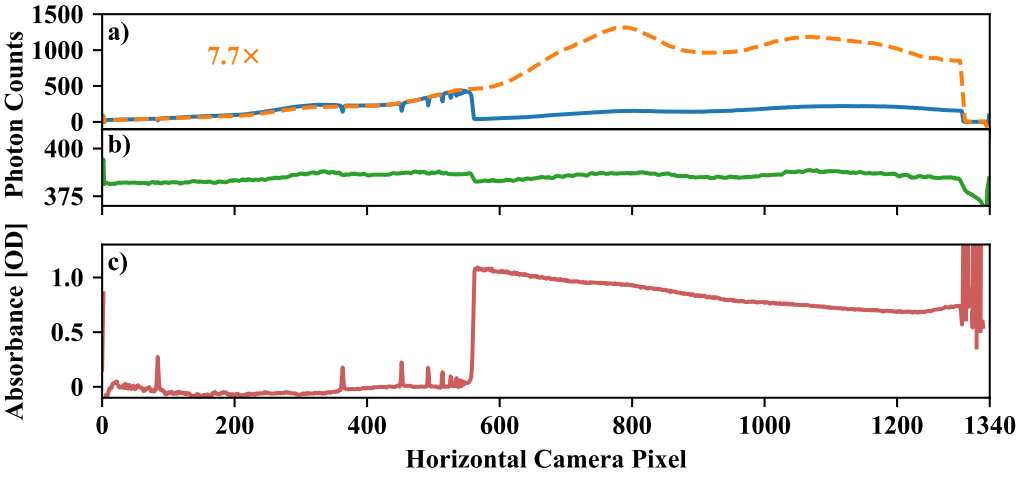

Figure 4.2: The calculation of the absorbance. The horizontal camera pixels are approximately linear with the wavelength of the XUV pulse a) The transmission signal in blue averaged over the region of interested and with dips at energies of the dipole allowed transitions from the ground state of helium. The ionization threshold is visible by the drop of the transmission at roughly camera pixel 560. The dashed orange curve is the *in situ* reference averaged over the region of interest. It is multiplied by a factor 7.7 for a better comparison with the transmission signal. b) The camera background averaged in the region of interest. The background was subtracted from transmission and reference in a). c) The absorbance calculated with equation 4.1 in units of optical density.

spectrum. This second-order spectrum is, however, almost completely absorbed after switching on the target gas due to the high absorption of the ionization continuum, effectively changing the multiplication factor. Instead, one can see, by using equation 2.70 for the calculation of the absorption, that the factor c simply leads to an offset of the absorbance

$$A(\omega) = -\log_{10}\left(\frac{I(\omega)}{c \cdot I_0(\omega)}\right) = -\log_{10}\left(\frac{I(\omega)}{I_0(\omega)}\right) + \log_{10} c, \qquad (4.1)$$

Therefore, it is just subtracted after the recording. Furthermore, for the correct calculation of the absorbance, the background photon counts of the camera have to be subtracted from the transmission and the reference before the absorption is calculated. It can be obtained on the same camera image, above the *in situ* reference spectrum, in the region of interest given between the dashed-dotted lines in figure 4.1 and shown in figure 4.2 b). It shows a slight dip at the position of the ionization threshold, which is probably due to a blooming effect, which is a characteristic of the CCD cameras, or residual XUV light from the diffraction of the XUV beam on the target gas. This XUV diffraction is most efficient close to resonances [114] and thereby also at the sharp onset of the ionization threshold.

The absorption calculated with equation 4.1 shows the absorption of the resonant transition from the ground state to the singly excited states in helium, depicted in figure 4.2 c) in units of optical density. Furthermore, the absorption of the first

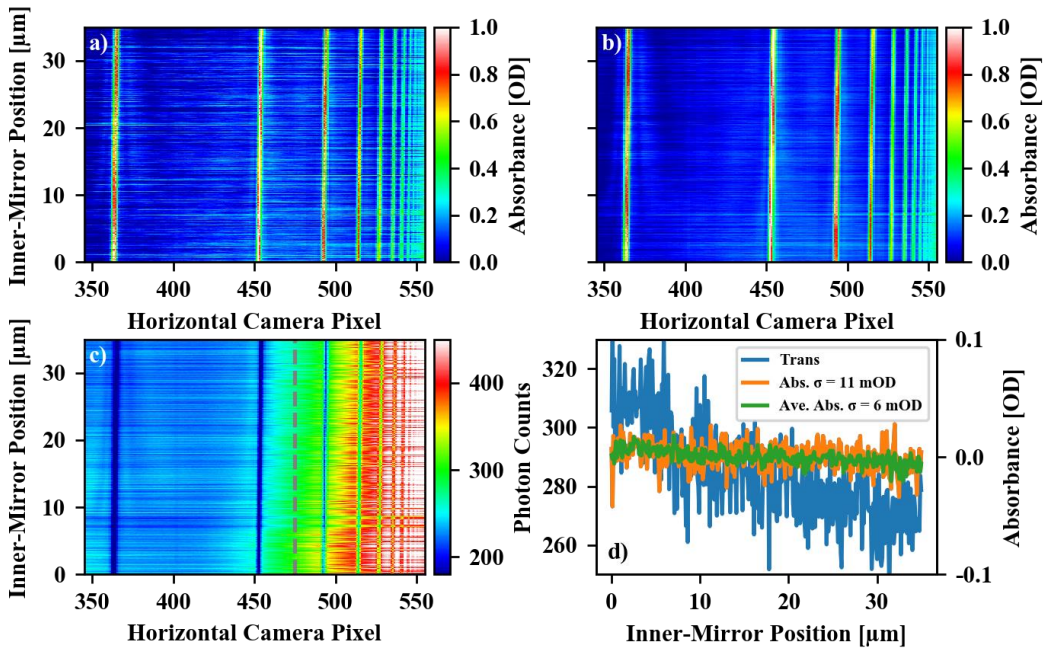

Figure 4.3: Inner-mirror scans of the transmission and calculated absorbance. a) The absorbance in units of optical density for different inner-mirror position, where the NIR is blocked by the iris aperture. The absorption lines of resonant transitions in helium are visible by vertical lines. They are slightly tilted, which is an effect of the walk-off of the XUV beam and it will be corrected further below. b) The absorbance in the same camera region like in a) averaged over 5 scans of the inner mirror. The noise across the scan is greatly suppressed. c) XUV transmission intensity spectrum through helium for different inner-mirror position. The absorption by helium is visible by vertical gaps in the spectrum. The intensity increases from low to high camera pixel due to the structure of the incident harmonic spectrum. The dashed grey vertical lines indicate the position where the lineout is taken for d). d) Lineout of the transmission (Trans.) and absorbance (Abs. or Ave. Abs.) taken from a), b), and c) versus inner-mirror position. The sensitivity of the inner-mirror-dependent signal changes are higher for the absorbance, where the lineouts of the averaged absorbance results in a precision of 6 mOD

ionization continuum is visible together with its threshold by the step-like increase of the absorption around camera pixel 560. This absorbance signal is obtainable for different positions of the inner mirror controlling the time-delay between the NIR and XUV pulses, as shown in figure 4.3 a) for no NIR. One can directly see the improvement of the visibility of the absorption lines compared to the inner-mirror-dependent transmission signal depicted in subfigure c). The lineouts at the camera pixel 475, indicated by a grey dashed line in c), is shown in d). While the transmission signal falls by scanning the inner-mirror position, the absorbance stays almost constant. Its fluctuation is in the order of ∼11 mOD and defines the measurement sensitivity for the absorption. It is further improved by averaging the absorbance for many scans of the inner mirror, shown in subfigure b) for five scans. The corresponding lineout in subfigure d) yields a sensitivity of ∼6 mOD, which is a sufficient precision for a clean observation of many NIR-laser-induced changes of the absorption.

Additional improvements of the signal to noise are achieved by exploiting that the reference and the background are smooth curves with the camera pixel position. Since their signals are weak, the camera noise imprinted on them will dominate the noise after the absorbance calculation. Using a rectangular sliding average between a few camera pixels for the reference and the background (here for three pixels) reduces their noise while negligibly affecting the absorption signal. Furthermore, as visible in figure 4.3 d), the absorbance is slightly linear dependent on the inner-mirror position. Since no NIR was present in this scan, it can be attributed to an artifact of the calculation procedure by the *in situ* reference. Most likely, it is due to small spatial clippings of either the main or reference XUV beam on the target cell, which changes while scanning the inner mirror caused by the above-mentioned XUV walk-off. This clipping leads to a change of the relative strength of the observed transmission or reference signal and thereby to a different calculated absorbance. Experimentally, it can be partly compensated by tracking the position of the target cell with the inner-mirror position. Instead, one can argue that the clipping leads just to an inner-mirror-dependent offset $\log_{10} c$ in equation 4.1. This offset is the same for all the scans with and without NIR, and therefore it is determined once by a scan without NIR and globally corrected for all other scans with NIR.

Photon Energy Calibration

The absorption lines visible in the transient absorption data correspond to specific electronic transitions that are dipole-allowed from the ground state of the atom. For the quantum mechanical interpretation of NIR-induced effects in the absorption, it is thus beneficial to assign the absorption lines to the transition. Furthermore, as discussed in the fundamentals chapter, the presence of strong-field effects depend on the relative energy between the field given in terms of ponderomotive energy and the typical energies of the system. In order to consider this relation and perform the state assignment, a calibration of the excitation photon energy is needed.

A dispersive reflection grating achieves the separation of the different energies of the harmonic spectrum in the spectrometer. Figure 4.4 a) shows a drawing of the dimension of the grating. The different wavelengths of the XUV pulse are projected on the spectral plane, where the CCD camera records the photons. For the dispersion of the XUV wavelength λ one can approximately use the grating equation

$$m\,\lambda = g[\sin(\alpha) - \sin(\beta)], \qquad (4.2)$$

where m is the spectral order of the dispersion, α and β are the angle of incidence and angle of reflection, respectively, and g is the effective grating constant. In the experiment, two different gratings exist for the highest efficiency in two different energy regions of interest. One has a grating constant $g = 1/1200$ mm for the

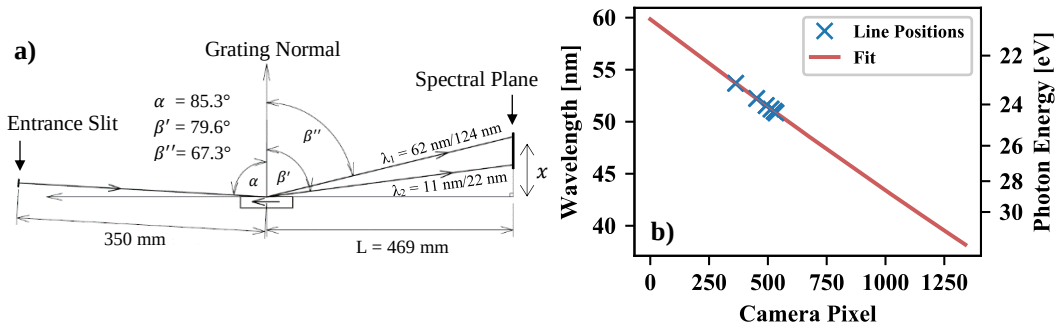

Figure 4.4: The flat-field spectrometer grating and its calibration. a) A sketch of the grating with the design dimensions. For a high spectral resolution, the experiment should adhere to the design values given in the sketch. b) The calibration of the camera pixel to the excitation XUV photon energy. Blue crosses indicate the camera pixel positions of the visible singly excited absorption lines with known resonance wavelengths. The red curve is the fit of the wavelength to the camera pixel given using equation 4.3 and is also given in units of eV by the right axis.

wavelength range between 11 and 62 nm, and the second with $g = 1/600$ mm is for wavelengths between 22 and 124 nm, which corresponds to about 20 to 112 eV and 10 to 56 eV photon energy, respectively. With the grating equation and considering the geometry of the experimental setup, the XUV wavelength can be related to the camera pixel by the equation

$$\lambda = \frac{g}{m}\left[\sin(\alpha) - \frac{1}{\sqrt{\left(\frac{x}{L}\right)^2 + 1}}\right]. \qquad (4.3)$$

Here, L is the distance between the grating and the camera, and x is the position of the camera with respect to the grating substrate surface, see figure 4.4, which can be changed in order to scan the whole spectral plane by the camera of finite size. Furthermore, with the adjustment of L and the orientation of the camera with respect to the spectral plane, the final spectral resolution can be improved, which will be discussed in the next section.

Slight changes in the parameters in equation 4.3 influence the mapping of the wavelength to the camera pixels. Therefore the equation can be used to generate a photon energy calibration curve by fitting the absorption line positions where the transition energy is known. The free fit parameters are then α and x/L. In the case of the energy region between 20 and 30 eV, helium itself can be used, since, without the presence of the NIR, only the dipole-allowed transitions from the $1s^2$ ground state to the singly excited $1snp$ Rydberg series are visible. Blue crosses show the corresponding positions in figure 4.4 b) together with the best fit. In principle, one can also use a polynomial fit function, e.g., a linear function in the present case, to obtain the energy calibration curve. However, the lines are often, and also here, concentrated on a small region on the camera, and using only a polynomial fit

function could lead to high errors above this series, i.e., here in the ionization continuum above 24.5 eV.

As mentioned in the chapter on the experimental setup, the moving of the inner mirror in the split-mirror setup introduces a walk-off of the XUV beam. As a consequence, it slightly changes the angle of incidence on the spectrometer grating. Thus, the calibration curve will depend on the position of the inner mirror. Since the angle of incidence $\alpha \approx 85°$ is large, and its changes are small, the wavelength shift is approximately linear with the inner-mirror position. For the correction of this walk-off effect, one can trace the position of the NIR-free absorption line, i.e., without field-induced line-shape changes, and shift the calibration curve in camera pixel direction. Figure 4.5 shows the 1s4p absorption line without and with compensation of the walk-off. By knowing the strength of the compensation for the spectra without NIR, it can be readily applied to the spectra where the NIR is present. Note due to the walk-off, the whole signal on the camera is shifted, i.e., both the transmission and the *in situ* reference signal. Thus, it is beneficial to compensate for the walk-off before cutting out the reference signal by a tilted region of interest since otherwise, the reference signal will slightly step out of the region. Furthermore, for a similar reason, the correction of the photon energy calibration should be applied before the above-mentioned correcting of the inner-mirror-position-dependent offset.

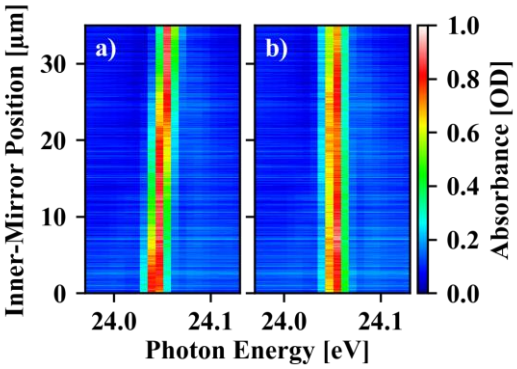

Figure 4.5: The correction of the shift of the calibration curve with the inner-mirror position due to the walk-off of the XUV beam. a) the 1s4p absorption line where no NIR is present. The energy shift of the line is solely attributed to the walk-off and it can be compensated by shifting the calibration curve in pixel direction for different mirror positions as shown in b).

The Effect of Finite Spectrometer Resolution

In the interpretation of the absorption strength, in particular, if one wants to compare the absorption from bound-bound and bound-continuum transitions, one has to consider the finite spectrometer resolution carefully. Its importance is noticeable, in particular, for the singly-excited Rydberg series in helium. Here the static absorption of the resonant transitions visible in figure 4.2 c) appears small compared to the absorbance of the ionization continuum. However, the photoionization cross section of the helium close above the threshold is 7.5 Mb, and the cross-sections of the resonant transitions are several orders of magnitude higher [63,115,116]. Figure

4.6 shows the cross-section of helium given by a numerical model simulation, which will be described in the following chapter. The sharp vertical lines are the resonant lines and are up to a hundred times higher than the cross-section plateau starting at 24.58 eV that is the first ionization continuum.

In order to compare the cross-section to the measurement, the absorbance in units of optical density, according to equation 2.70, has to be calculated. Here, commonly the spectrometer resolution is considered by convolving the cross-section by a point spread function of Gaussian shape $K(\omega)$ given by:

$$K(\omega) = \frac{1}{\sqrt{2\pi\sigma_{\mathrm{res}}^2}} e^{-\frac{1}{2}\left(\frac{\omega}{\sigma_{\mathrm{res}}}\right)^2} \qquad (4.4)$$

where σ_{res} is the spectrometer energy resolution. Equation 2.70 is then modified to

$$A'(\omega) = \frac{\sigma(\omega) * K(\omega)}{\ln 10}\, \rho\, l, \qquad (4.5)$$

where $*$ is the convolution operator. The resulting absorbance for the experimental helium density of $\rho \approx 1.2{\cdot}10^{18}\,\mathrm{cm}^{-3}$ that corresponds to a backing pressure of 50 mbar and a propagation length of $l = 3$ mm is shown in blue in the subfigure 4.6 c). Comparing with the measured absorbance, see figure 4.2 c), here, the absorbance of the resonant transitions is overestimated, whereby the absorption strength of the continuum is on a similar scale as in the measurement. Thus, while this approach of

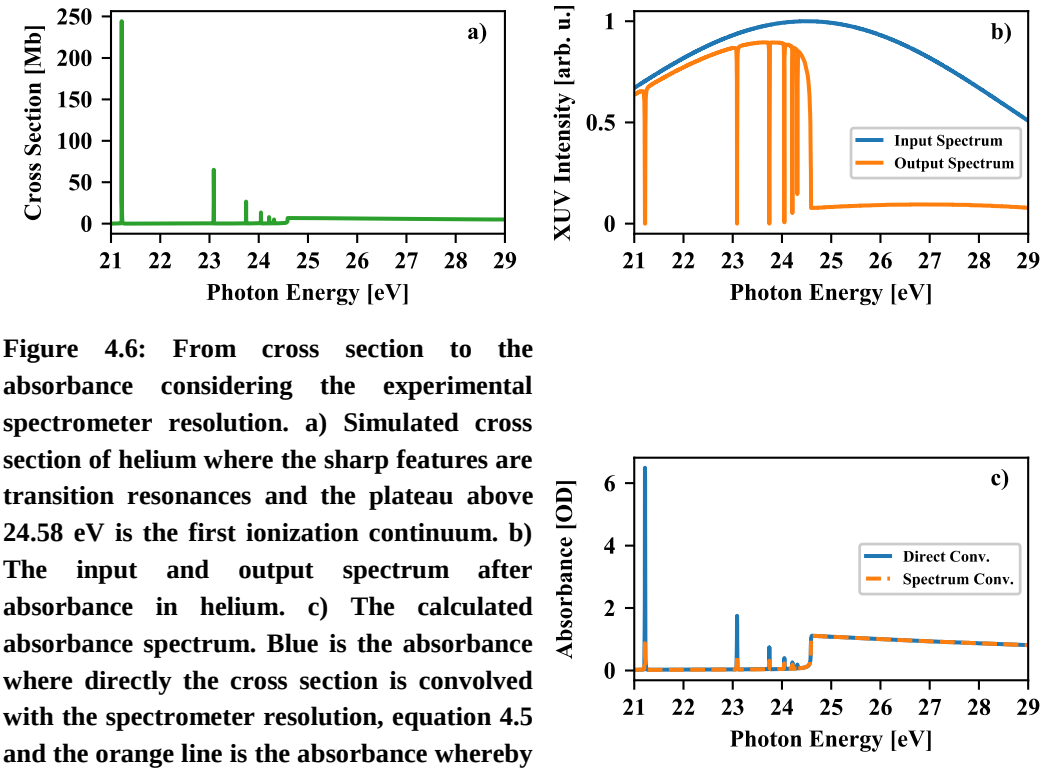

Figure 4.6: From cross section to the absorbance considering the experimental spectrometer resolution. a) Simulated cross section of helium where the sharp features are transition resonances and the plateau above 24.58 eV is the first ionization continuum. b) The input and output spectrum after absorbance in helium. c) The calculated absorbance spectrum. Blue is the absorbance where directly the cross section is convolved with the spectrometer resolution, equation 4.5 and the orange line is the absorbance whereby the output spectrum is calculated and convolved first, equation 4.6.

considering the spectrometer resolution by convolving the cross-section is appropriate for relatively broad spectral lines, it fails for sharp lines with high cross-sections.

The XUV spectrometer records the transmitted intensity rather than directly the absorbance. According to Beer's law given by equation 2.68, the cross-section enters in the exponent of the factor that is multiplied with the incident spectrum. Figure 4.6 b) shows an example of a simulated incident and transmission XUV spectrum. The sharp lines in subfigure a) become sharp dips in the transmission spectrum, whereby their depth is even not distinguishable anymore for the first lines with the lowest energy. Applying the convolution with the function for the spectrometer resolution onto this transmission spectrum leads to the absorbance that is shown by the orange dashed curve in subfigure c). The equation used for the calculation reads

$$A''(\omega) = -\log_{10}\left(\frac{K(\omega) * \left[I_0(\omega)e^{-\sigma(\omega)\rho l}\right]}{I_0(\omega)}\right). \qquad (4.6)$$

With this procedure, the absorbance of the resonant transitions is highly suppressed compared to the continuum absorption. To summarize, the reason for the low resonant absorption lines observed in the measurement despite their high cross-section is the convolution of the transmission spectrum with the finite spectrometer resolution. As a consequence, if the NIR laser is present, it will broaden the resonant absorption lines and therewith increase their visible absorption strength.

Time Delay Calibration

As will be discussed in the chapters about the experimental results, the signatures of laser-driven quantum-dynamical processes, like NIR-induced couplings among bound quantum states, are observable in transient absorption spectroscopy typically by NIR-electric-field-cycle or even NIR-sub-cycle oscillations of the absorption. For the central wavelength of ~750 nm, one NIR-field-cycle is about 2.5 fs. Thus, in order to be sufficiently sensitive for sub-cycle oscillations of the absorption, one needs a time-delay resolution of below 250 as, which corresponds to ten time-sampling points of the oscillation. This resolution is provided by the interferometer geometry of the attosecond beamline, where both NIR and XUV co-propagate and are split in time by the split mirror setup. Here, the inner mirror is translated with respect to the outer mirror by a piezo-driven translation stage. Experimentally, one cannot adjust a certain time-delay point but rather a voltage on the piezo. Therefore for further analysis, the time delay has to be calibrated with the piezo position.

For its first estimation, one can consider the geometry of the split-mirror with the grazing incidence angle θ of the laser beam onto the mirror setup. Here, the moving

of the translation stage of the inner mirror by Δx results in a laser-propagation-path-length change of Δl and yields a time-delay change $\Delta\tau$ that is given by

$$\Delta\tau = \frac{\Delta l}{c} = \frac{2\,\Delta x\,\sin\theta}{c}, \qquad (4.7)$$

where c is the speed of light. Using the design gracing incidence angle of $\theta = 15°$, this corresponds to ~1.727 fs for the translation of the stage by 1 µm. Since the incident angle depends on the alignment of the lasers, this time-delay dependence might change slightly. For a more reliable calibration, it can be measured using a helium-neon alignment laser with a known wavelength λ_{HeNe}. It is impinged onto the mirror setup, and its interference is recorded in the focus, which is a similar setup, as was described in the experimental setup chapter. Figure 3.11 shows the intensity oscillation of the interference while scanning the translation stage position. From the slope m of the oscillation phase, one can directly access the time-delay change, which reads

$$\Delta t = \frac{m}{\Delta x}\,\frac{\lambda_{\mathrm{HeNe}}}{2\pi\,c}. \qquad (4.8)$$

The here presented measurement yields a change of 1.705 fs per µm, where the typical relative error by this calibration is below 1%. A similar procedure can be performed for the interferometer geometry with the externally incoupled NIR laser pulse that results in a time-delay change of ~6.67 fs per µm translation.

It is often sufficient to know the relative delay between the XUV and the NIR pulses. However, for some timing-sensitive processes like the ionization gating of the time-dependent dipole moment, which will be treated in the last result chapter of this thesis, the knowledge about the point of absolute time overlap between the pulses is needed. A simple approach to find this overlap is to impinge the short NIR pulse onto the split-mirror setup and to record its beam profile in its focus position by a camera. By setting the inner-mirror stage position close to time overlap, an NIR-interference pattern appears on the camera. While scanning the time-delay position, the point of the highest visibility of the interference can be interpreted as the point where the maxima of the pulse envelope are in overlap, i.e., defining time zero.

This procedure, however, provides just an estimation of the point of time overlap because it crucially depends on the experimental settings. For instance, choosing different annular filter material in the attosecond beamline will lead – according to equation 2.24 – to different retardation of the pulses depending on the material's dispersion. It also depends on the relative orientation of the mirrors in the split-mirror setup, and small changes here for a better spatial alignment of the overlap of the XUV and NIR foci in the target influence the time overlap point. Furthermore, when using not the co-propagating interferometer geometry but the NIR pulse that is externally coupled into the beamline, every additional optical component for the manipulation

of the NIR pulse changes the overlap of the pulses. Thus, a reliable procedure for the determination of the time overlap has to be applicable during operation.

For this purpose, timing-sensitive strong-field-induced effects can be used for the determination of the time overlap. For instance, one can strong-field ionize the atom after its XUV excitation. With this, the XUV-induced dipole moment is cut when the NIR laser is present, and the strength of the absorption lines in the XUV spectrum will depend on the time delay of the pulses, where it will be minimal in the time overlap. An example of this method was applied to the autoionizing states in argon, so-called window resonances [24,117]. Other exploitable effects are the sub-cycle build-up of ion absorption lines [118] or the strong-field-induced ponderomotive shift of the atomic state's energy. The shift leads to the modification of the absorption line shape [35], which can be traced by the dipole control model (DCM) that was discussed in the fundamentals chapter and treated in further detail in the references [84,119].

Figure 4.7 a) shows the line shape of the sp_{24+} doubly excited state in helium for different time delays of the XUV and NIR. This line shape can be fitted by the

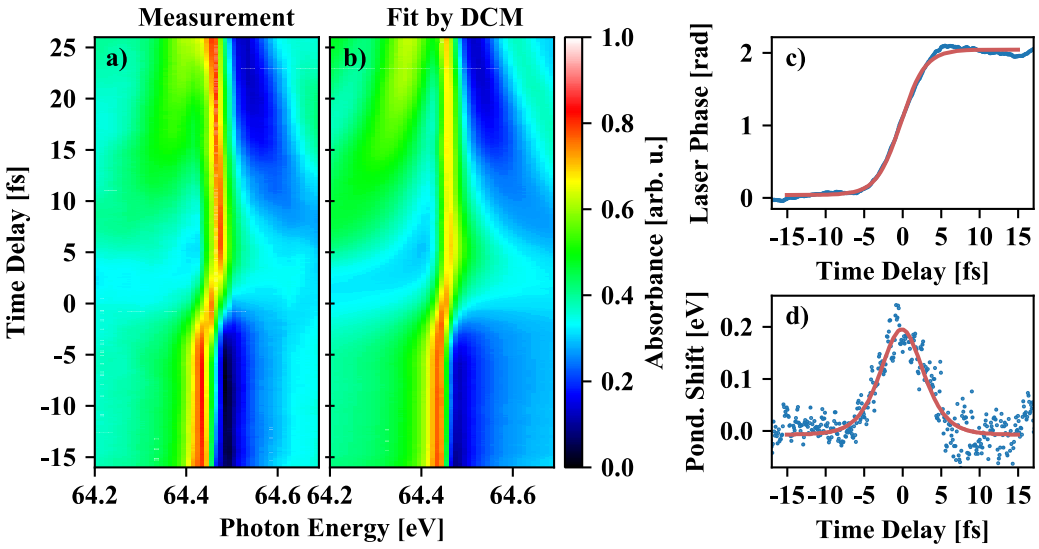

Figure 4.7: Determination of the time overlap of the NIR and XUV pulses. a) Time-dependent absorption spectrum of the sp_{24+} doubly excited state in helium. Negative delays means the NIR precedes the XUV pulse. The data are averaged in time for one NIR electric field cycle in order to suppress sub-cycle oscillation of the absorption line due to resonant couplings to other states. The NIR induces a change in the absorption line shape, which can be attributed to a phase shift in the dipole response that generates the absorption line. b) The fit results applied on the measured data using the dipole-control model given by equation 2.85. It reproduces all main features of the measurement. c) The laser-induced phase in blue resulting from the fit on the spectral absorption data. The red line is a fit to the phase of the function given by equation 4.9, where the pulse for the ponderomotive potential calculation is modeled by a $\sinh^2$-shaped intensity envelope. d) The ponderomotive shift in blue dots extracted from the fit results of the laser-induced phase by taking its time derivative. The red line is a fit to the data using equation 2.33 for the ponderomotive potential.

function for the dipole moment in the spectral domain given by equation 2.85, as is shown in subfigure b). Here, the amplitude for the ionization of the line is set to unity, and the DCM phase is a free fit parameter. The result for the phase is shown in subfigure c), and it is a smooth increasing curve across the time overlap. According to the reference [119], the time-delay-dependent phase $\phi(\tau)$ is given by the equation

$$\phi(\tau) = \frac{m}{\hbar}\int_0^\infty U_p(t-\tau, \tau_{\mathrm{FWHM}})dt + c. \qquad (4.9)$$

It is the time-integrated ponderomotive shift U_P that the NIR laser pulse with pulse duration τ_{FWHM} induces onto the state. The fit parameter c is the data offset, and m is a multiplication factor ≤ 1, which depends on the considered state. It accounts for the susceptibility of the state to be affected by the strong laser field. It is generally higher the energetically closer the bound state is to the continuum, i.e., the more loosely bound the state is to the core. Using equation 4.9, one can fit the time-delay dependent phase, shown in red in figure 4.7 c), whereby reliable fit results are obtained by modeling the NIR laser pulse with a sech^2 time-shape given by equation 2.3 with a pulse duration of 5.5 fs. The inflection point of the fit then corresponds to the time position when the dipole excitation occurs in the maximum of the NIR field envelope, i.e., in the time overlap. Thus, the time axis can be shifted such that time zero is at this point, which is already done in the figures. Note that the time-delay value is also used in the fit procedure of the spectral line shape by the DCM model. Therefore, one has to iteratively fit the line shape again with the shifted time-delay axis of the data and test the final convergence.

The pulse-like shape of the NIR-induced ponderomotive shift can be seen by taking the derivative of the time-delay-dependent phase. Figure 4.7 d) shows $\hbar\frac{d\phi(\tau)}{d\tau}$ by blue dots in units of energy. The observed peak of the shift should be symmetric around the time overlap. Here one can directly fit the function for U_P given by equation 2.33 in order to obtain the pulse duration and the zero time position, depicted by a red line in the figure. The fit results are similar to those obtained by directly fitting the laser-induced phase. Furthermore, the derivative here shows the maximal magnitude of the ponderomotive shift, which is proportional to the peak intensity of the NIR pulse and whose calibration will be discussed in the following section.

Peak Intensity Calibration

The NIR intensities can be defined to be strong, as discussed in the fundamentals chapter, if the corresponding energy scale, e.g., the ponderomotive potential, is comparable with energies of the target system, for instance, the ionization energy or transition energies between resonances. This definition is practicable because one observes different laser-induced quantum-dynamical processes to be dominant with

weak or with strong fields. In addition, from a scientific perspective, these processes are of great interest in the transition from weak to strong intensities. In the experiment, one can adjust the NIR laser intensity by closing and opening of an iris-aperture. Here, one systematically cuts out power from the beam profile of the NIR laser beam, and thereby the intensity in the target is a monotonic function of the iris opening. However, it is not linear with the iris position because the cutting of the power is centrosymmetric starting from the outer part of the beam profile, and the power is not the same across the transverse section of the beam. Furthermore, the cutting effectively leads to a change in the beam waist. Thus according to the laws of laser beam propagation [38], it changes the focus size and thereby the peak intensity in the target. Hence, in order to know the intensity regimes in the experiment and to be able to compare the measurement results with benchmark simulations, the NIR intensities have to be calibrated with the iris opening position.

In the field of attosecond transient absorption spectroscopy, the peak intensity and the pulse duration in the target is typically determined directly by means of photoelectron streaking experiments additional to the absorption measurement; see, for instance [120,121]. However, the time of flight apparatus needed for this type of experiment is not yet implemented in the attosecond beamline during the data acquisition for this dissertation, but it is planned to upgrade the setup in the future. Nevertheless, the order magnitude of the peak intensity can often be deduced by other procedures. A straightforward method is to measure the average NIR power and the beam waist in the target focus for different iris-aperture openings. Using the equations 2.9 and 2.10 and knowing the pulse duration and repetition rate of the laser, the peak intensity can directly be calculated and thereby related to the iris position. However, this procedure neglects that the XUV focus and therewith the interaction volume in the target is smaller than the NIR focus, and thus not the whole laser power contributes to the experiment. Furthermore, the macroscopic signal is generated by the coherent superposition of the dipole responses of the atoms in the gaseous target cloud, and not every atom is subjected to the same NIR intensity, which makes the need for a spatial focus averaging.

For a more reliable intensity calibration, a method is needed, which is *in situ* and treat better the experimental conditions. For this purpose, an intensity-dependent effect in the absorption can be used, similar as for the determination of the time overlap of the pulses. As shown in figure 4.7, the ponderomotive shift of the state's energy is linked to the line shape of the doubly excited states in helium. Since the peak intensity goes linear with the shift, see equation 2.33, one can readily scan the iris opening and trace the maximal applied ponderomotive shift. By doing so, one should favorably choose a state, which is as loosely bound as possible, i.e., a high Rydberg state, since then the parameter m in equation 4.9 is close to unity. This procedure applies only to a certain limit of intensities since, at some point, the strong-field ionization of the state is too high, and the strength of the absorption line

decreases or even vanishes such that the determination of the laser-induced phase by the fitting procedure breaks down.

Another approach is to directly compare the measured absorption for different intensities with results of numerical model simulations. As an example, one can trace the Autler-Townes splitting of the 2s2p doubly excited absorption line in helium for different iris openings. The splitting is due to the two-NIR-photon resonant coupling of the 2s2p state at 60.15 eV with the sp_{23+} state at 63.66 eV via the intermediate $2p^2$ state lying at 62.06 eV. Figure 4.8 a) shows the absorption line for different time delays between the XUV and NIR pulse. It is split into a symmetric doublet at slightly positive delays when the states are subjected to the almost full NIR pulse, indicated by a grey arrow in the figure. This signal that is time-averaged around the time of maximal splitting, is shown in figure 4.8 c) for different iris openings, and it can be compared with the results of the numerical model simulation shown in subfigure d).

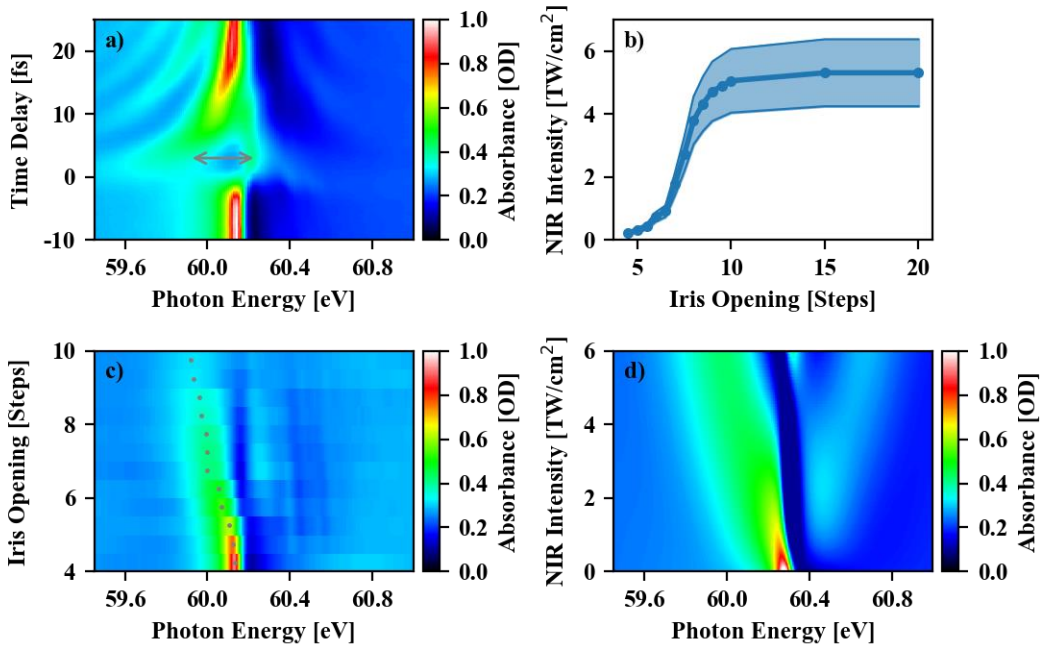

Figure 4.8: Calibration of the NIR intensity with the iris-aperture opening. a) Time-delay-dependent transient absorption spectrum of the 2s2p doubly excited state in helium. Negative time delays mean that the NIR proceeds the XUV pulse. The data is averaged in time by one NIR-electric-field cycle in order to suppress the sub-cycle oscillation of the absorbance due to resonant couplings to other states. These couplings lead to the Autler-Townes splitting of the resonant absorption line, which is indicated by a grey arrow. b) The *in situ* calibration curve of the NIR intensity for different opening positions of the iris aperture valid for a specific NIR input power. The curve is obtained by comparison of the measured Autler-Townes splitting with results of a numerical model simulation. The shaded area denotes the 20% error by this calibration procedure. c) The measured splitting for different openings of the iris. The data is a three data point average around the time of maximal splitting shown in a). The grey dotted line indicates the trace of the splitting, whose position is used for the intensity calibration. d) The expected line splitting calculated by a numerical model simulation for different NIR intensities. This result it used as a reference to generate the calibration curve in c).

In this model, the above-mentioned states are coupled by a simulated NIR pulse with a certain intensity, and their response is calculated via solving the time-dependent Schrödinger equation in a split-step algorithm. An example of the implementation of such a numerical simulation will be given in the next chapter. By comparing the traces indicated by the dotted line in figure c), one can assign the iris openings to the specific NIR peak intensity, which is shown in subfigure b). Here the position of zero means full closing of the iris. Due to this comparison, the error is estimated to be 20%. The field intensity increases nonlinearly for the openings between 5 and 10 and shows a plateau below and above these values. Although the intensity values here are only valid for the specific input power used for the scan, the general trend of the intensity increase with iris opening position is provided. However, one should still calibrate the peak intensity for every single experiment. Furthermore, special caution has to be exercised if one scans the time-delay between the XUV and NIR since the split mirror introduces a walk-off, i.e., lateral displacement of the XUV focus with respect to the NIR focus. Thus one obtains an inner-mirror-dependent NIR intensity. This limits the maximal time-delay range, and one has to align both foci such that they stay in the overlap in this limited range of interest.

5. Attosecond Transient Absorption of a Continuum Threshold

With the possibility to generate attosecond light pulses by means of high harmonic generation, many time-resolved measurements have been performed for the investigation of light-matter interaction of atomic, molecular, and solid-state systems with a time resolution on the natural timescale of electronic excitations; see the references [21–26,28] to mention a few. The high time resolution has been achieved in these experiments via scanning a time delay between an isolated attosecond pulse or a pulse train and a second ultrashort (and strong) laser pulse that are focused on the target under investigation. These pulses excite or ionize the target, and the measured observable is either the spectrum of the photoionized fragments, i.e., the photoelectrons or the ions, or the photoabsorption spectrum.

When measuring the photoionization fragments, the target has to be ionized, meaning that at least one electron is always excited into the continuum. Here, the ionization is achieved either by single-photon ionization or utilizing multiphoton or multicolor ionization. In typical experiments, the yield or the spectra of photoelectrons or photoions are measured by a detector that is located far away from the light-matter interaction point. With the help of the measured kinetic energy, the point of impingement on the detector, or both, one can trace back to the point in time and/or space of the light-matter interaction to study the light-induced dynamics [122]. By doing so in a time-resolved manner, one is sensitive to phases between different ionization pathways or streaking traces [120]. This sensitivity to these phases allows, for instance, to access and control the quantum phases between resonant transitions [123–125], to measure the temporal structure of the laser pulses [126], or to determine the ionization delays on the attosecond time scale [127,128].

For the delay experiments, the Coulomb interaction of the freed electron with the residual electrons or the ionic core dominantly governs the duration of the delays during the ionization process. Thus, for slow photoelectrons with small kinetic energies, which remain longer in the vicinity of the parent ion, these delays become longer [129]. Furthermore, since the impact of the Coulomb potential is not small for slow electrons, the often-used strong-field approximation breaks down, which neglects the Coulomb field with respect to the electric field [130]. Thus, new insight about the light-matter interaction can be expected from measurements of light-induced time-dependent structures on slow photoelectrons, which are electrons excited closely above the ionization threshold [130–136].

The complementary type of experiments on the attosecond timescale is based on the measurement of the XUV photoabsorption spectrum. Here, one directly accesses light-induced dynamics on electronic bound states of a system. With this all-optical method, one can resolve state-specific transitions far below, close to as well as embedded in an ionization continuum. However, in contrast to the photoelectrons/ions measurements, here, one does not need to ionize the system. Instead, the laser-induced modification of the absorption spectrum observed in these measurements can be attributed to the laser-induced changes of the time-dependent dipole moment of the non-ionized system. This dipole moment interferes coherently with the XUV excitation pulse and leads to the absorption spectrum, which encodes the characteristic laser-induced changes. This interferometric understanding intuitively explains the sensitivity to laser-induced phase and amplitude modifications of the resonances [31,33,35]. To further point out, as seen by the equation 2.58, the XUV-induced dipole response is dominated by the overlap of the excited and ground-state spatial wave function. Thus, by measuring the time-dependent dipole moment using absorption spectroscopy, the system is probed locally at the light-matter interaction point within the atom.

Despite most experiments in the field of attosecond transient absorption spectroscopy concentrated on dynamics involving resonant transitions, the XUV pulse can also ionize the system. Thus the dipole moment between the continuum and the ground state is expected to give rise to light-induced structures in the transient absorption spectra as well. Similar to resonant absorption lines, one should be sensitive to light-induced phase shifts or amplitude modifications of the continuum states encoded in these structures. Furthermore, due to the local measurement scheme, the probed photoelectron is nearby to the residual ion, where its dynamics are expected to be most strongly influenced by the Coulomb potential. The first treatments of the XUV absorption spectrum for a smooth continuum, i.e., well above the ionization threshold, were theoretically addressed in reference [137], and transient absorption measurements have been performed at the ionization threshold in helium [56,138–140]. However, there the results are interpreted by laser-induced couplings between bound states, and the role of the time-dependent continuum dipole moment has not yet been elucidated.

This chapter discusses the signatures of the ionization threshold in attosecond transient absorption spectroscopy in the case of helium. The here presented absorption measurements become sufficiently sensitive for the first time with the help of the *in situ* XUV reference method. This allows one to reconstruct the time-dependent dipole moment that generates the spectrum at the threshold, which is a probe of slow free electrons in the vicinity of the ionic core. Thus, this study is a step towards linking local measurements by transient absorption spectroscopy and slow electron measurement in phase-sensitive photoionization measurements. Parts of this

chapter have been published in the reference [1], and the discussion here will therefore adhere closely to this publication.

Sub-Cycle-Resolved Response of the Continuum Threshold in Helium

With the high time and spectral resolution of the attosecond beamline, the effects of the NIR pulse on the absorption of the helium atom at the first ionization threshold can be resolved. Figure 5.1 shows the time-delay-dependent transient absorption spectra of helium around its first ionization threshold. The data processing steps to obtain this spectra from the experimental data acquisition are described in the previous chapter. The spectra show modifications of the bound absorption lines typical for transient absorption, like NIR-induced broadenings, NIR-sub-cycle oscillations of the line strength, or hyperbolic structures with respect to the time delay. All these can be attributed to NIR-induced resonant or non-resonant couplings between bound and continuum states. Here the discussion will focus on the NIR-modified absorption of the ionization threshold, while the interested reader may find further information for the absorption of the bound states in the references [33,55,56,138,139].

At XUV photon energies higher than the ionization threshold at about 24.58 eV, mainly two characteristic features are observed. The first is a fast NIR-half-cycle oscillation, which appears across a broad spectral range both below and above the ionization threshold. To investigate this in more detail, figure 5.1 b) depicts the amplitude of the Fourier transform with respect to the time-delay axis. The fast oscillation leads to diagonal Fourier peaks around 3 eV in Fourier energy, which

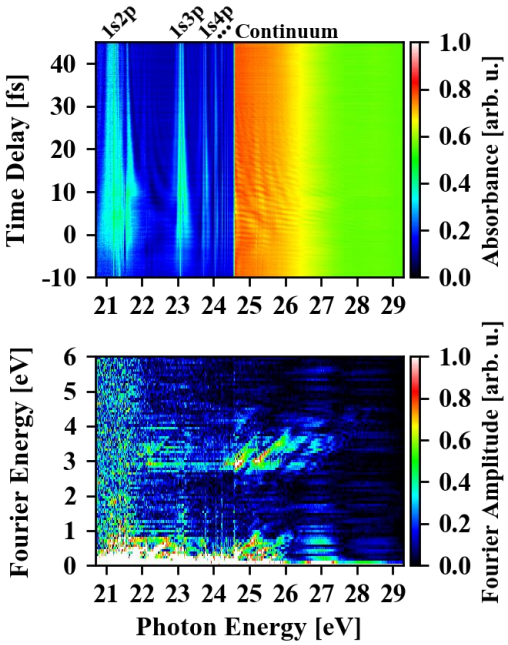

Figure 5.1: Time-delay-dependent transient absorption spectra of the first ionization threshold in helium. a) Absorption spectra for different time delays between the NIR and XUV pulse, where negative delays mean that the NIR precedes the XUV pulse. The observed NIR-induced modifications of the spectra are discussed in the main text. b) The amplitude of the Fourier transform of the absorption with respect to the time-delay axis in a). The NIR-sub-cycle oscillations of the absorption lead to Fourier signals around 3.2 eV Fourier energy that is about twice the NIR central photon energy. Slow hyperbolic-like structures in the absorption spectra lead to diagonal Fourier signals close to zero Fourier energy.

corresponds to twice the NIR central photon energy of about 1.6 eV, thereby indicating a two-NIR-photon coupling process. One can isolate this feature in the transient absorption spectra by applying a band-pass filter around the diagonal peaks in the Fourier domain and Fourier transforming back in the time delay domain. The result that is zoomed into the threshold region is shown in 5.2 a) together with the filtered Fourier signal in b). Here the strong DC-Fourier signal is subtracted such that the absorption step of the ionization threshold is suppressed. The oscillation shows several phase jumps at photon energies of resonant absorption lines and, in particular, across the ionization threshold. Since the absorption signal results from the constructive or destructive interference of the XUV-induced time-dependent dipole moment with the XUV electric field, see fundamentals chapter, the phase jumps may be attributed to phase shifts of the dipole moment energetically below and above an absorption line. The visibility of the phase jump across the ionization threshold could indicate that the response of the continuum influences the dipole moment of the atom, and it has to be included for its whole interpretation, which will be further discussed below.

The second feature visible in the transient absorption spectra is a slow hyperbolic-like structure after the XUV-NIR temporal overlap, which converges to photon energies close to the continuum edge for increasing time delays, see figure 5.2 b).

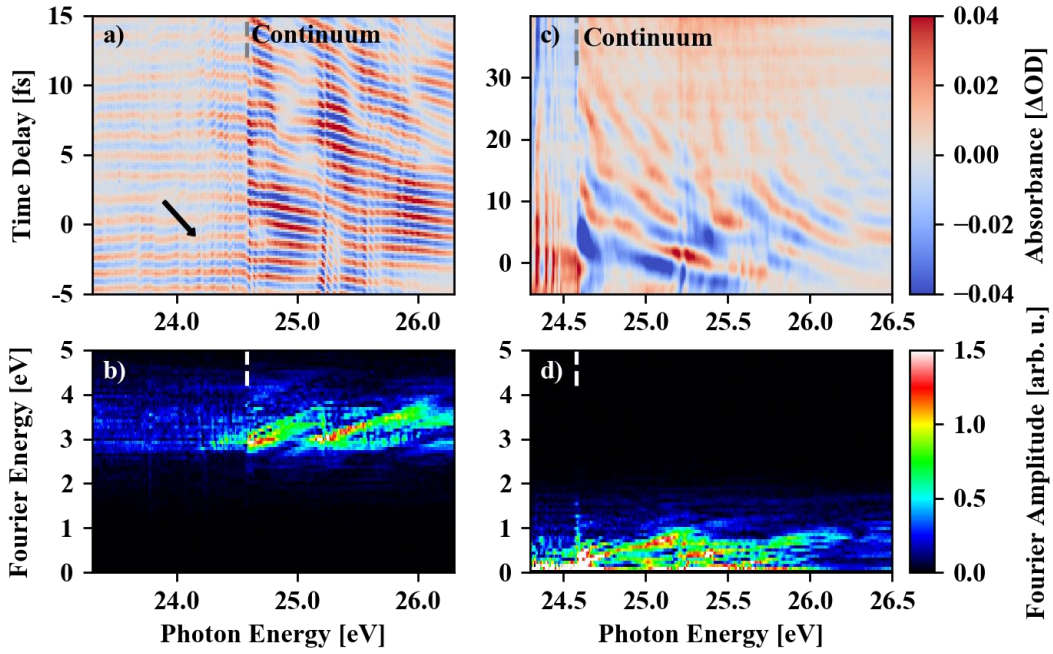

Figure 5.2: Time-delay-dependent change in the absorption for two different frequency regions of the change. a) NIR-induced absorption change in the periodicity of the half-NIR-cycle oscillation. The oscillation appears in a broad spectral range and phase jumps appear across resonant absorption lines and the ionization threshold. b) The filtered Fourier signal from the measurement leading to the change in absorbance shown in a). c) Slow absorption changes. Above the ionization threshold hyperbolic-like features appear, which leads to diagonal Fourier signals for low Fourier energy shown in d).

This structure leads to a diagonal feature of the Fourier amplitude near-zero Fourier energy, which intersects the photon-energy axis to XUV energies of the Rydberg states and the continuum threshold. For better visibility, the zoom-in of this signal with an applied filter for the low Fourier energies is shown in figure 5.2 c) and d).

As mentioned above, the spectrum for each time delay corresponds to a time-dependent dipole moment of the helium atoms. With the help of the method for its reconstruction directly from the absorption spectrum, presented in the fundamentals chapter, and in particular, in reference [50], the response of the ionization threshold can be traced in real-time. Here, one can exploit that the reconstruction method serves the possibility to select different energy regions of interest since both the absorption of the Rydberg lines as well as of the non-resonant ionization continuum contribute significantly to the total reconstructed dipole. In order to isolate the response of the continuum, an asymmetric super Gauss filter function $F_{\mathrm{G}}(\omega)$ can be used, which cut out the absorption of the continuum and has the form

$$F_G(\omega) = \begin{cases} \exp\left(-\left(\dfrac{|\omega-\omega_0|}{\Omega_{\mathrm{left}}}\right)^{n_{\mathrm{left}}}\right) & \text{for } \omega \leq \omega_0 \\ \exp\left(-\left(\dfrac{|\omega-\omega_0|}{\Omega_{\mathrm{right}}}\right)^{n_{\mathrm{right}}}\right) & \text{for } \omega > \omega_0. \end{cases} \qquad (5.1)$$

The parameter ω is the photon energy, ω_0 is the energy position, Ω_{left} and Ω_{right} the left and right-sided width, and n_{left} and n_{right} the left and right-sided order of the asymmetric filter, respectively. Figure 5.3 a) shows this filter together with the static absorption of helium without the NIR. By choosing appropriate parameters, this filter ensures that the filtering process only weakly contributes to the results of the time-dependent dipole. For instance, by including the ionization continuum within the filter, a relative smooth right part, i.e., for higher photon energies, with a large Ω_{right} suppresses a false dipole signal for long real times, which would be present by using a sharp-edged filter. On the left side, the absorption is almost zero closely below the threshold, and thus a filter with sharp edges does not significantly change the result.

The amplitude of the dipole response of the ionization threshold without the presence of the NIR is shown in figure 5.3 b). The response falls rapidly for the first few femtoseconds, which corresponds to the broad spectral structure of the ionization continuum, and it shows some small revivals of the dipole, which can be attributed to the step-like increase of the absorption across the ionization threshold. This response can be reconstructed for different time delays of the, now present, NIR, which is shown in subfigure c). Here, the NIR induces oscillations of the response around the time overlap of the XUV excitation and the NIR pulse. Furthermore, a structure appears, which follows in real time the time-delay position of the NIR. For better visibility of the NIR-induced changes of the dipole response, subfigure d) depicts the dipole response subtracted by the static response without NIR, shown in b). Here, the fast oscillation is more pronounced. Furthermore, one can observe a

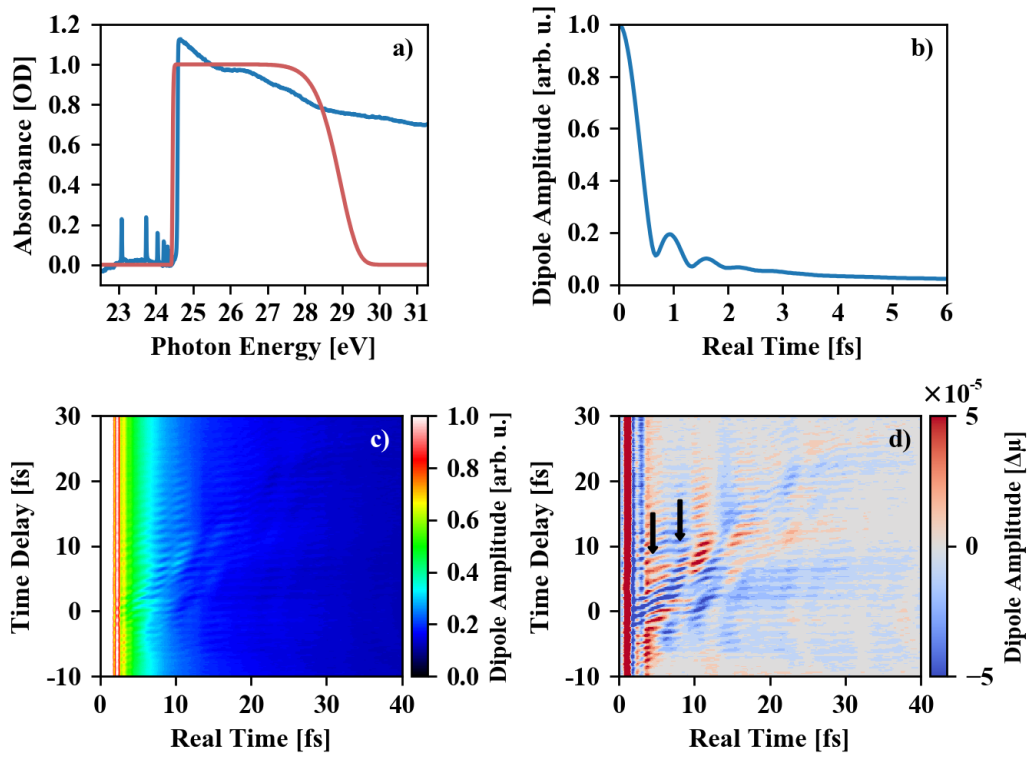

Figure 5.3: Time and time-delay-dependent dipole response of the ionization threshold in helium. a) The absorption spectrum of the ionization threshold without NIR and the applied spectral asymmetric filter for the dipole reconstruction method. b) The amplitude of the time-dependent dipole moment of the ionization threshold. Corresponding to the broad spectrum of the ionization continuum the dipole is a fast decreasing function in time with some small revivals reflecting the step in the absorption across the threshold. c) The time-dependent dipole moment amplitude dressed with a time delayed NIR pulse. Fast and slow oscillation with respect to the time delay and real time appear. d) The dipole moment shown in c) subtracted by the moment without NIR shown in b) for better visibility of the oscillations. Despite the fast half-NIR-cycle oscillation of the dipole moment with respect to the time delay, it shows an overall enhancement and drop in real time following the NIR time position, which is indicated by arrows.

drop and increase of the dipole response for short real times that are indicated by black arrows.

The here presented features in the time-delay-dependent absorption spectra at the ionization threshold could have different origins. For instance, so-called light-induced states could appear in the threshold's energy region. These are states which are mapped into the continuum by one or two NIR photon from lower bound states, and they are mainly visible in the time overlap of the NIR and the XUV pulse [55]. Furthermore, as already discussed, the fast modulation of the absorption at the threshold could be caused by two-photon couplings among bound states. Nevertheless, also the absorption of the ionization continuum itself might contribute to these features. In order to mechanistically understand and isolate possible contributions of the ionization continuum in the spectra, a method is needed that is able to selectively switch on and off the presence of the continuum and thereby test the changes in the absorption. For this purpose, a quantum-mechanical multi-level

model is applied to simulate numerically the absorption response in helium that will be introduced in the following sections.

Quantum Mechanical Multi-Level Model Simulation

For a reliable comparison between the measured spectra with results of numerical model simulations and in order to identify the contributions of the continuum in the transient absorption spectra, a flexible and modular simulation algorithm is needed. High flexibility is provided by simulations using a multi-level model. Here, the energy levels are represented by bound states, as well as discrete continuum states of the simulated atom. The total state $|\psi(t)\rangle$ is then given by a superposition of bound $|\phi_i\rangle$ and continuum states $|\xi_i\rangle$

$$|\psi(t)\rangle = \sum_i \alpha_i\,(t)|\phi_i\rangle + \sum_j \beta_j\,(t)|\xi_j\rangle, \qquad (5.2)$$

with their corresponding time-dependent complex-valued state amplitudes $\alpha_i(t)$ and $\beta_i(t)$, respectively. The modeling of the continuum by the discrete levels will be described in the next section, while first, the steps of the simulation algorithm are introduced. In order to simplify the equations and reduce the numerical costs, for the calculation, the atomic unit system is used (a.u.). The derivation of the equation will thus adhere to this system. The definition of this system and the conversion factors to the common SI units are given in the appendix.

The states are excited by an XUV pulse, and then they are strongly coupled by a time-delayed NIR pulse. The dipole response of the modeled helium is calculated with the help of the complex-valued time- and time-delay-dependent dipole moment $\mu(t,\tau)$ between the levels. With this dipole moment, one can generate the XUV photoabsorption cross-section for every NIR-XUV time-delay position τ by [141]

$$\sigma(\omega,\tau) = g\,4\pi\alpha\omega\;\mathbb{Im}\left\{\frac{\tilde{\mu}(\omega,\tau)}{\tilde{F}_{\mathrm{XUV}}(\omega)}\right\}. \qquad (5.3)$$

Here g is the number of considered electrons ($g = 2$ for helium), $\alpha \approx 1/137$ is the fine structure constant, $\tilde{\mu}(\omega,\tau)$ is the Fourier transform of $\mu(t,\tau)$ with respect to the real-time, and $\tilde{F}_{\mathrm{XUV}}(\omega)$ is the complex-valued XUV excitation spectrum. This cross-section is proportional to the XUV-photon-absorbance, which can be compared to the measured spectra in the end.

The algorithm for the simulation is numerically implemented by a parallelized Python script using matrix representation. Here, the total state is written as a state vector, where the vector elements are the state's amplitudes

$$|\psi(t)\rangle = \begin{pmatrix} \alpha_0(t) \\ \vdots \\ \alpha_M(t) \\ \beta_0(t) \\ \vdots \\ \beta_N(t) \end{pmatrix} \quad (5.4)$$

with M representing the number of bound and N the number of continuum states. The state vector is then numerically propagated in time by a split-step algorithm [142] that solves the Schrödinger equation

$$i\hbar \frac{d}{dt}|\psi(t)\rangle = \left[\hat{H}_0 + \hat{H}_{\text{int}}(t)\right]|\psi(t)\rangle. \quad (5.5)$$

Here $\hat{H}_0$ is free Hamiltonian, which is represented by a diagonal matrix with the energies of the states as entries, and $\hat{H}_{\text{int}}(t)$ is the interaction Hamiltonian with the NIR pulse in the dipole approximation given by

$$\hat{H}_{\text{int}} = \hat{\mu}_{\text{int}} F_{\text{NIR}}(t) = \begin{pmatrix} 0 & \mu_{0,1} & \cdots & \mu_{0,N} \\ \mu_{1,0} & \ddots & & \vdots \\ \vdots & & \ddots & \mu_{N-1,N} \\ \mu_{N,0} & \cdots & \mu_{N,N-1} & 0 \end{pmatrix} F_{\text{NIR}}(t), \quad (5.6)$$

where $\mu_{i.j}$ is the dipole moment between state i and j with $\mu_{i,j} = \mu_{j,i}^*$. $F_{\text{NIR}}(t)$ is the time-dependent NIR electric field defined on a numerical time grid.

At the beginning of the simulation, only the ground state is occupied, i.e., $\alpha_0(t) = 1$, and the amplitudes of all other states are zero. As introduced in the fundamentals chapter, the ground state of helium is the state where both electrons are in the 1s energy level. Considering the dipole-transition rules, the weak XUV pulse perturbatively populates all odd excited states with p-symmetry given by previously derived equation 2.48 for the temporal change of the state amplitude in perturbation theory. The model includes the bound states with even and odd parities, the s-, p- and d-symmetries up to 1s4s, 1s5p, and 1s8d, as well as the odd-parity continuum states 1sEp.

After the XUV excitation, the state vector is transformed into an eigenstate of the interaction Hamiltonian. The transformation matrix $\hat{T}$ consist of the basis eigenvectors that are obtained by the diagonalization of the dipole matrix $\hat{\mu}_{\text{int}}$. The transformed state is then propagated with one time step Δt dressed by the time-dependent NIR electric field. Finally, the state is back-transformed to an eigenstate of the free Hamiltonian. To summarize, the operations for the NIR interaction are:

$$|\psi(t + \Delta t)\rangle = \hat{T}\left[e^{-iE_{\text{int}}\Delta t\, F_{\text{NIR}}(t)} \cdot \left[\hat{T}^T \cdot |\psi(t)\rangle\right]\right], \quad (5.7)$$

where E_{int} are the eigenvalue of $\hat{\mu}_{\text{int}}$And" $\cdot$ " denotes the dot product. At the end of the algorithm, one step with the free energies is applied

$$|\psi(t + \Delta t)\rangle = |\psi(t)\rangle \cdot e^{-\left(iE_0 + \frac{\Gamma}{2}\right)\Delta t}, \quad (5.8)$$

where E_0 is the vector with the eigenvalues of the free Hamiltonian $\hat{H}_0$, and Γ is the decay vector, which accounts for the de-excitation of the states. The values for the decay rate of the states will be given below. Finally, the dipole matrix element is calculated via

$$\mu(t) = \langle \psi_g | \hat{\mu}_{\text{int}} | \psi(t) \rangle, \qquad (5.9)$$

where $|\psi_g\rangle$ is the ground state. In principle, one can calculate the whole dipole moment; however, the XUV spectrum is dominated only by the dipole moment between the excited and ground state, and it is, therefore, sufficient to use the approximated equation 5.9. Here, the valid assumption is made that the amplitude of the ground state always remains almost unity since the XUV only perturbatively populates the excited state from the ground state. The NIR intensity and its photon energy are too low that it has only a negligible impact on the depopulation of the ground state.

The described algorithm is applied on a time grid and for different time delays between the XUV and NIR pulse. Here, the length of the time grid determines the resulting energy resolution of the simulated spectra, and the time step size determines the maximal observable photon energy without producing numerical artifacts. In the simulated spectra shown below, the photon energy resolution is 0.0002 eV, which corresponds to the total propagation time of about 20 ps (~850000 a.u.). The highest photon energy of interest is set to 40 eV, which is about 15 eV above the ionization threshold, and therefore it needs the time step size of about 10 as (~0.43 a.u.). Thereby the simulation performs 2,000,000 time steps in total.

The XUV pulse is modeled by a $\cos^2$-shaped intensity envelope in time with the pulse duration of 150 attoseconds full width at half maximum (FWHM), and it is energetically centered at 24.5 eV photon energy. This definition leads to a sufficiently

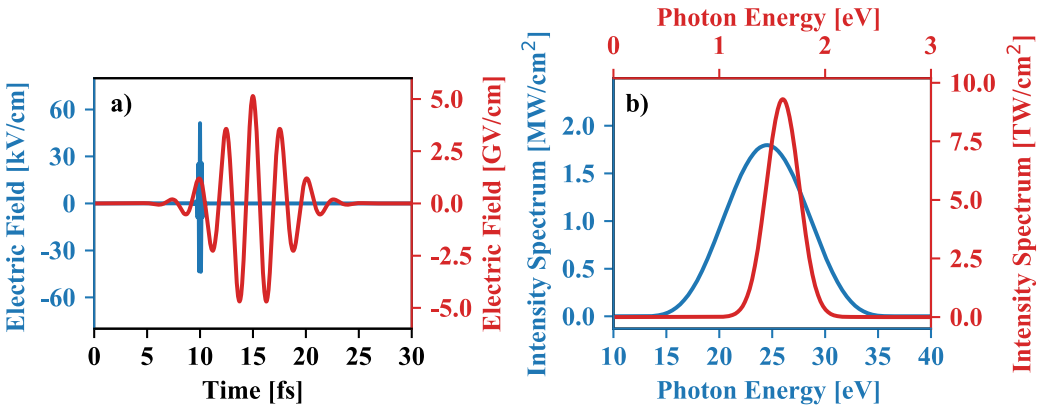

Figure 5.4: The XUV (in blue) and NIR (in red) pulses used for the model simulation. a) The electric field of both pulses in time. For better visibility each pulse has its own y-axis. Here, the time delay between the pulses is set to 5 fs. b) The intensity spectra of the two pulses. The XUV spectrum is centered around the ionization threshold of helium (~24.58 eV) and the central NIR photon energy is 1.6 eV.

broad excitation spectrum with well-defined limits covering the XUV energy region of interest between 20 and 30 eV, see figure 5.4. The time-delayed NIR pulse has a Gaussian intensity profile, a duration of 5 fs FWHM, central photon energy of 1.6 eV, and a peak intensity of ~$9.3 \cdot 10^{12}$ W/cm^2, as it is similar to the NIR pulse in the experiment.

Modeling of the Continuum Threshold

In the multi-level model simulation, each state has specific properties that are its energy E_i, the decay rate in terms of the decay constant Γ_i and values for the dipole moments to all other states. For the first few bound states, the values for the energies and dipole moments can be found in different references [62,63]. However, as in the references, the values for the oscillator strength are often given rather than directly the dipole moments. With the definition of the dipole moment given by equation 2.57, one can relate the oscillator strength $f_{1,2}$ to the absolute value for the dipole moment [63,143]. It is given by (for clarity in SI units):

$$\mu_{1,2} = -e \left| \sqrt{\frac{3\hbar}{2m_e \omega_{1,2}} f_{1,2}}, \right| \qquad (5.10)$$

where m_e is the electron mass (= 1 a. u.) and $\omega_{1,2}$ is the transition angular frequency. In the equation, one neglects the mass of the electron compared to the proton mass, which would, including the ratio, only be a $\sim\sqrt{0.1}\%$ correction. Furthermore, only the linear polarization of the XUV and NIR pulses are treated. Thus, the electric-field-induced couplings are only among states with magnetic quantum number $m_l = 0$, and thereby any states' degeneracy factor is unity. The dipole moments between the bound states used for the simulation are summarized in table 2 and 3 of the appendix.

The natural lifetimes of the singly-excited states in helium are in the order of several nanoseconds [144], which corresponds to natural absorption linewidths below 1 µeV. The XUV spectrometer has, however, in the spectral range of the singly-excited Rydberg series, a spectral resolution of about 10 meV. Thus, it cannot resolve these narrow lines in the experiment. In order to observe these lines, they have to be (NIR-induced) broadened to several meV of spectral width first. In the end, the absorption spectra resulting from the model simulation should be compared to the measured spectra. Therefore the simulated spectra have to be convolved with the spectral resolution of the experiment. Thus, it is sufficient to use lifetimes in the picosecond timescale for the bound states in the simulation, which corresponds to linewidths in the order of hundreds of µeV. These lifetimes are at least 2 orders of magnitude longer than any timescale for light-induced modification of the atomic response, and so they will not change the results. In addition, since the maximal

propagation time of the simulation determine the spectral resolution, the shorter lifetimes relax this simulation time and therewith reduce the numerical costs.

For states with energies above the ionization threshold, no published values are known. Thus, these values have to be calculated using some model assumptions. By doing so, the solutions should guarantee that the shape of the simulated continuum absorption is similar to the measured absorption. That means one has to reproduce the step-like increase of the absorption across the ionization threshold, the continuous absorption above the threshold, and the slight decrease of the absorption strength for higher energies. For this purpose, one can calculate the energies of the state in the continuum by assuming that the free electron is in a box potential. The scaling of the energy E_n with the continuum states' number n is then given by

$$E_n = \varepsilon\, n^2 + I_\mathrm{p}, \qquad (5.11)$$

where $I_\mathrm{p} = 24.58$ eV is the ionization potential, and ε is a proportionality factor. If the volume of the model box V increases, this factor will decrease, and in the limit of an infinite box, ε tends to zero

$$\lim_{V\to\infty} \varepsilon = 0. \qquad (5.12)$$

By choosing small values for ε, i.e., a large model box, the resulting individual absorption lines in the continuum will – if a certain linewidth is given - start to overlap with each other. Close to the limiting case of equation 5.12, they will therewith generate a flat absorption spectrum.

In a real atom, the total number of continuum states N is infinite. In the simulation, one has to cap N, and thereby the resulting flat absorption is cut at a specific maximal energy. This leads to a second threshold on the high energy side of the spectrum, and one has to verify that this artificial threshold is not affecting the final results. Furthermore, by choosing small ε and considering equation 5.11, one has to increase N in order to obtain an absorption in a broad spectral range above the ionization threshold. However, the computational costs scale with the square of N, and therefore one has to make a tradeoff between choosing ε as small as possible with still tractable N. In the following, ε is set to 10^{-4} eV, which is two orders of magnitude smaller than the energy resolution of the measurement. The number of the states is therefore set to 400 in order to cover photon energies up to at least 15 eV above the threshold, and thereby the energy corresponds to a continuum state's momentum of above 1 a.u.; see description below.

The XUV-photon-absorption calculated by equation 5.3 is dominated by the dipole moment between the ground state and the excited (bound or continuum) states. Considering equation 2.58, this dipole moment depends on the spatial overlap between the electronic wave function of the excited states and the ground-state wave function. If a real atom is ionized, i.e., the atom is excited into continuum states, the liberated electron will leave the parent ion. Thus, the electronic wave function will

lose the overlap with the ground-state wave function over time, and therewith the dipole moment between these states decreases. In order to account for this dipole decrease in the model simulation, the continuum states have an effective decay, and thereby one obtains non-zero absorption linewidths for the continuum states in the absorption spectrum. Here, the decay constant Γ_n of continuum state n linearly scales with the velocity of the freed electron, which is (in atomic units) the state's momentum p_n. The momentum can be calculated by the excess energy that is given by the difference between the state's energy and the ionization potential I_p

$$\Gamma_n = \gamma\, p_n = \gamma\sqrt{2\left(E_n - I_\mathrm{p}\right)} = \gamma\, 2\,\sqrt{\varepsilon}\, n. \qquad (5.13)$$

The last equality uses equation 5.11.

Equation 5.13 states that the decay rate scales linearly with the continuum state number n. The linear proportionality factor γ determines the final linewidth in the absorption spectrum, and it has to be chosen such that the individual lines are not visible anymore, i.e., all absorption lines add up into a flat continuous absorption spectrum. Although the linear scaling of the decay rate with the state's momentum is a model approximation, the proportionality factor has an intuitive interpretation. Its reciprocal is the characteristic distance in atomic units of the electron from the atomic core that leads to the decrease of the wave function overlap and therewith of the dipole moment.

The absolute value of the dipole moments between bound and continuum states can be calculated by solving the integral given by equation 2.58. In order to do so, the wave function for the bound and continuum states are needed. In first approximation, only one electron of the helium atom is active, i.e., it is excited or ionized, and the other electron stays on its lowest quantum level and therewith screens the charge of the atomic core seen by the excited or ionized electron. Thus, the wave function of the continuum states can be approximated by hydrogenic atomic structure theory with an effective core charge Z_eff. Here, one can assume, with good approximation, that this effective charge is unity for all states except for the ground state.

Using the hydrogenic atomic structure theory, the wave functions are Coulomb wave functions, which are the solutions of the time-independent Schrödinger equation of the hydrogen atom with negative or positive energy. The Coulomb potential is only distance-dependent, and thus the wave function can be factorized [46]

$$\psi_i(\vec{r}) = \chi_i(r) Y_{l_i,m_i}(\theta,\varphi), \qquad (5.14)$$

where $\chi_i(r)$ is the, yet to be determined, radial wave function and $Y_{l_i,m_i}(\theta,\varphi)$ is the spherical harmonic of state i with angular momentum quantum number l_i and magnetic quantum number m_i. r, θ, and φ, are the radial distance, polar angle, and

azimuthal angle of the spherical coordinate system, respectively. Using this decomposition of the wave function, equation 2.85 reduces to the dipole moment from the state 1 to state 2 given by

$$\mu_{1,2} = -C_{1,2} \int_0^\infty \chi_2^*(r)\, r^3\, \chi_1(r) dr, \qquad (5.15)$$

with the prefactor

$$C_{1,2} = \int_0^\pi \int_0^{2\pi} Y^*_{l_2,m_2}(\theta,\varphi)\ \sin\theta\ \cos\theta\ Y_{l_1,m_1}(\theta,\varphi)\, d\varphi\, d\theta. \qquad (5.16)$$

This factor exhibits all the dipole transition rules and is only nonzero if $|l_1 - l_2| = 1$ and $|m_1 - m_2| \leq 1$. Here, it is assumed that the polarization of the XUV pulse points in the $z = r\cos\theta$ direction.

For the radial wave function, two different general solutions exist depending on whether the energy of the solution is negative or positive, i.e., the state is bound or unbound [145,146]. For the bound solution (subscript b) for a particular principal quantum number n, one gets

$$\chi_b(r) = \mathcal{N}_b(n,l,Z_{\text{eff}})\, e^{-rZ_{\text{eff}}/n}\, r^l\, {}_1F_1(-n+l+1;\ 2l+2;\ 2r\,Z_{\text{eff}}/n). \qquad (5.17)$$

Here, $\mathcal{N}_b(n,l,Z)$ is a normalization factor given by

$$\mathcal{N}_b(n,l,Z) = 2^{l+1}\left(\frac{Z_{\text{eff}}}{n}\right)^l \frac{\sqrt{(n+l)!/(n-l-1)!}}{(2l+1)!\ n^2/Z_{\text{eff}}^{3/2}}, \qquad (5.18)$$

and ${}_1F_1$ is the confluent hypergeometric function of the first kind that is

$${}_1F_1(a;b;z) = \sum_{k=0}^{\infty} \frac{(a)_k}{(b)_k}\, \frac{z^k}{k!}, \qquad (5.19)$$

with the notation

$$(x)_0 = 1 \ \text{ and } \ (x)_n = \prod_{k=1}^{n}(x+k-1). \qquad (5.20)$$

For the unbound state, the continuum state with subscript c, the solution is given for a certain momentum p_c by

$$\chi_c(r) = \mathcal{N}_c(p_c,l,Z_{\text{eff}})\, e^{ip_c r}\, r^l\, {}_1F_1(-iZ_{\text{eff}}/p_c + l + 1\,;\ 2l+2;\ -2ip_c r), \qquad (5.21)$$

with the normalization

$$\mathcal{N}_c(p_c,l,Z_{\text{eff}}) = 2^l p_c^{l+1}\, e^{\pi Z/2p_c}\, \frac{\sqrt{2/\pi}\,|\Gamma(l+1+iZ_{\text{eff}}/p_c)|}{(2l+1)!}, \qquad (5.22)$$

where Γ is the gamma function. Figure 5.5 shows the radial wave function given by equation 5.17 and 5.21 for different momenta of the continuum states. The continuum wave function is an oscillatory function and nonzero also for considerable distances,

and the envelope slowly decreases when the distance approaches zero. The periodicity depends on the state's momentum, and it is faster for higher momenta. The results for the dipole moments are sensitive to the spatial overlap between the wave functions, and thus as visible in figure 5.5, for higher momenta, the dipole moment increases first and decreases again; see also figure 5.7.

The whole model has now three free parameters that are γ, ε and Z_{eff}, which influence the shape of the simulated continuum absorption. Figure 5.6 shows the behavior of the absorption spectrum for different combinations of these parameters. By changing the decay rate proportionality factor γ, the most dominant effect is that the step-like increase of the absorption across the ionization threshold becomes softened, in particular, below the threshold. For high γ the step-like increase even vanishes, which can be seen by the green line in subfigure 5.6 a). Thus, in order to observe the threshold absorption step, the continuum states with energies closely above the threshold have to be very long-lived. This is intuitive since they represent free electrons with very low momenta, and the long lifetimes also apply to the high Rydberg states that are also energetically close to the threshold.

The effective charge of the ground state for the calculation of the dipole moments mainly changes the slope of the absorption versus energy, see subfigure 5.6 b). For $Z_{\text{eff}} = 2$, i.e., there is no screening of the doubly-charged helium core if the electron is in the ground state, an almost flat absorption across the energies is obtained. For lower effective charges, i.e., the inactive electron screens the helium core, the absorption has a maximum closely above the threshold and gets lower for higher photon energies. The energy step size ε has a minor influence on the overall shape of the absorption. Choosing too high values results in an absorption spectrum, where the individual lines are still discernable; see green line in subfigure 5.6 c). For values below the energy resolution, all individual absorption lines add up to a flat continuous

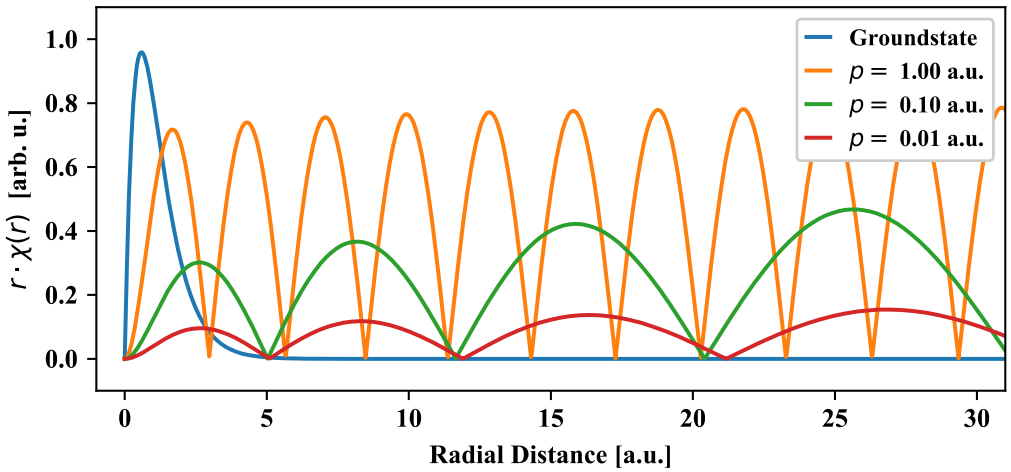

Figure 5.5: The radial wave function versus the radial distance in atomic units of the ground state given by equation 5.17 and for the continuum states by equation 5.21 for different momentum p in atomic units.

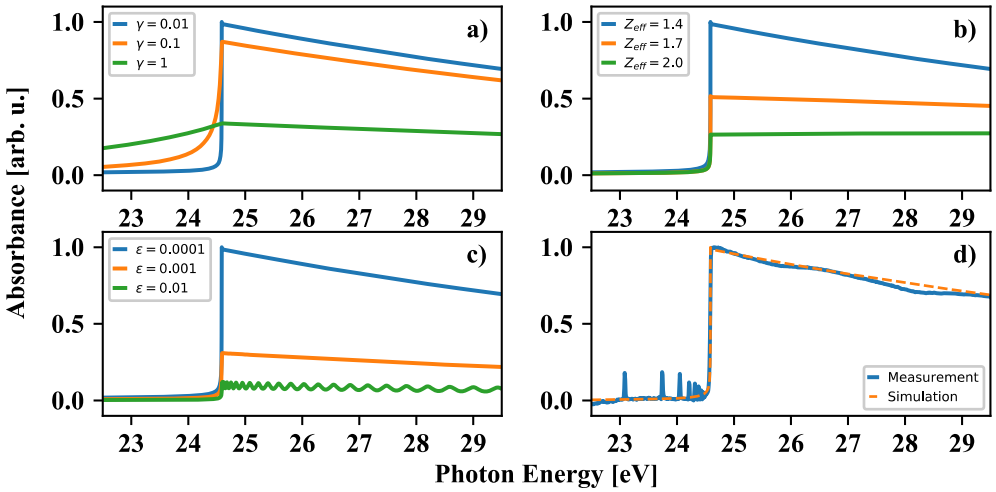

Figure 5.6: The simulated absorption spectra for different free parameter of the model. a) The spectra by changing the decay rate γ while $\varepsilon = 10^{-4} eV$ and $Z_{\mathrm{eff}} = 1.4$. b) The spectra for different Z_{eff} and $\gamma = 10^{-2}$ and $\varepsilon = 10^{-4} eV$. c) Spectra for different ε and fixed $\gamma = 10^{-2}$ and $Z_{\mathrm{eff}} = 1.4$. The behavior of the spectrum with the tuning of the parameter is discussed in the main text. d) Overall agreement of the measured and the simulated absorption spectra for the parameter $\gamma = 10^{-2}$, $\varepsilon = 10^{-4} eV$, and $Z_{\mathrm{eff}} = 1.4$. The small Rydberg series is visible in the measured absorption spectrum, which is, however, not yet included in the simulation.

absorption. Figure 5.6 d) shows the comparison of the measured and simulated absorption spectra for almost optimal parameters. The excellent agreement is achieved by the parameters $\gamma = 10^{-2}$, $Z_{\mathrm{eff}} = 1.4$, and $\varepsilon = 10^{-4}$eV, which will be used in the following. Tests showed that slight changes in these free parameters do not change the key findings that are discussed below.

Figure 5.7 summarizes the behavior of the continuum states' properties, i.e., the energy, the decay rate, and the dipole moments to the ground state for the above-mentioned parameters. According to equations 5.11 and 5.13, the energy scales quadratically, and the decay rate linearly with the state number. The dipole moment increases very rapidly, and after a peak, it decreases again. Subfigure b) depicts the density of states, that is $\Delta N/\Delta E$, the decay rate, and the dipole moments versus the excitation photon energy. It demonstrates the following: In order to represent the step-like increase of the absorption across the ionization threshold, a high density of states closely above the ionization threshold is needed, where the absorption of the states adds up. In the limit of very small energy step sizes, i.e., large model boxes, this would lead to a divergence of the density of states and therewith the absorption. However, the dipole moments decrease fast towards zero if one comes closer to the threshold, and thereby the individual states get less occupied by the XUV-excitation. Thus, the decrease of the dipole moment compensates the divergence of the density of states at the threshold, and together they lead to the absorption shape of the continuum onset similar to the measured onset. Furthermore, the amplitude of the dipole moments peaks at about 28 eV photon energy and decreases again almost

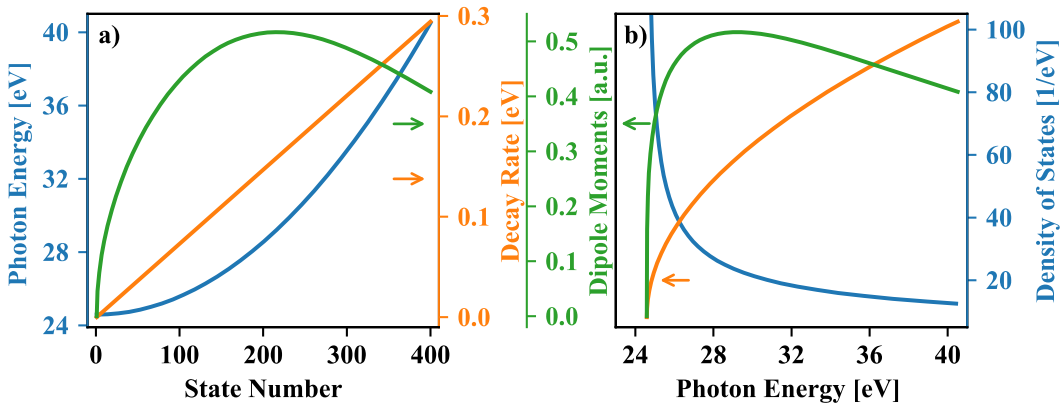

Figure 5.7: The continuum state's properties. a) The energy, the decay rate, and the dipole moment to the ground state with respect to the state number. b) The density of states, the decay rate, and the dipole moment versus the excitation photon energy. For the calculation of dipole moments the effective core charge for the ground state is $Z_{\mathrm{eff}} = 1.4$ and unity for the continuum states. In b) the density of states is shown given by $\Delta N/\Delta E$. It divergences towards infinity and the dipole moment convergeces to zero at the ionization threshold of about 24.58 eV.

linear for higher energies. This decrease finally leads to the decrease of the XUV absorption for higher photon energies that can also be observed in the measurement.

Note that all parameters change the total absorption strength, as seen in figure 5.6. For example, by choosing a small energy spacing, a higher number of states is needed, according to equation 5.11, in order to cover a broad energy spectrum. These states add up their absorption and therefore lead to higher absorption. However, not the total but rather the change of the absorption for different time-delays of the perturbing NIR pulse is of interest. So one can always normalize the final result.

Comparision of the Simulated and Measured Response

Figure 5.8 presents the results of the transient absorption spectra obtained by the model simulation with and without including the continuum absorption. Here, the photoabsorption cross-section is calculated into the absorbance by considering the experimental spectrometer resolution of 8 meV via the XUV transmission spectra, a procedure introduced in the previous chapter. Without continuum, subfigure a), some experimentally observed structures, for instance, the half-NIR-cycle modulation, are qualitatively reproduced. They appear, in particular, around the energy of the ionization threshold and lead to the diagonal Fourier feature at 3.2 eV Fourier energy, as shown in subfigure b). Thus, the origin of this feature at these photon energies is the all-optical interference between the direct XUV light and the delayed XUV-NIR transitions through the 1snp states, thereby creating light-induced states. This is consistent with previous observations, and the presence of the continuum threshold is not necessary for its explanation [33,138,139]. However, by applying the Fourier

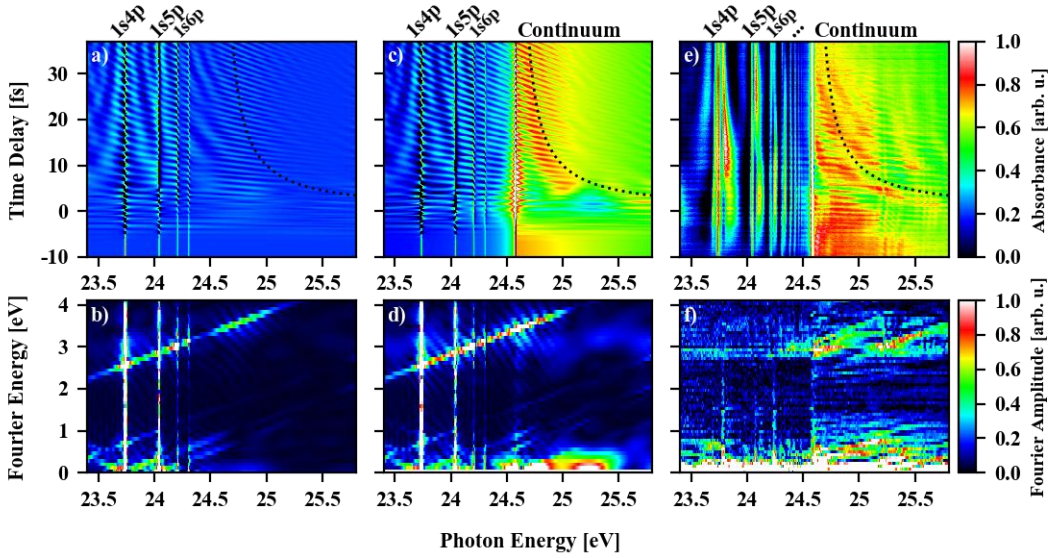

Figure 5.8: Simulated and measured time-delay-dependent transient absorption spectra. Positive time delays mean that the NIR follows the XUV pulse. a) Simulated transient absorption spectra without including the continuum response in the model simulation. Many NIR-induced features observed in the measured spectra are reproduced. However, the hyperbolic structure seen in the measurement is suppressed, indicated by a dotted curve. b) Fourier Signal by Fourier transformation of the time-delay axis in a). Almost no Fourier signal is observed above threshold and low Fourier energy. c) Simulated spectra with including the continuum in the model simulation. The hyperbolic structures observed in the measurement are recovered. It results in a diagonal Fourier signal above threshold and low Fourier energy in d). e) For comparison zoom-in of the measured spectra at the ionization threshold in helium. The hyperbolic structure above threshold is highlighted by a dotted line. f) Amplitude of the Fourier transform with respect to the time delay axis in e).

filter again around this Fourier feature, it turns out that the continuum is needed to reproduce the observed phase shift of the oscillation across the threshold, see figure 5.9. Furthermore, concerning the Fourier signal close to zero Fourier energy and photon energies above the ionization threshold, the simulation without the continuum show almost no signal, whereas the measured data show rich structures in this region, see figure 5.8 e) and f).

By adding the continuum states to the state manifold of the simulation, additional features arise, which are shown in figures 5.8 c) and d). First, the sharp absorption step at the ionization threshold of 24.58 eV is reproduced. Second, the hyperbolic structures above the ionization energy become more pronounced in the time-delay-dependent absorption spectra. This leads, in agreement with the experimental observation, to diagonal Fourier features intersecting the photon-energy axis at the ionization threshold. As a result, this comparison shows that the hyperbolic structures at the ionization threshold are linked to the NIR-induced couplings between bound and continuum states. As a result of this, the ionization threshold shows a similar—not a priori clear—behavior in the time-resolved absorption spectra, as is the case for a bound–bound transition.

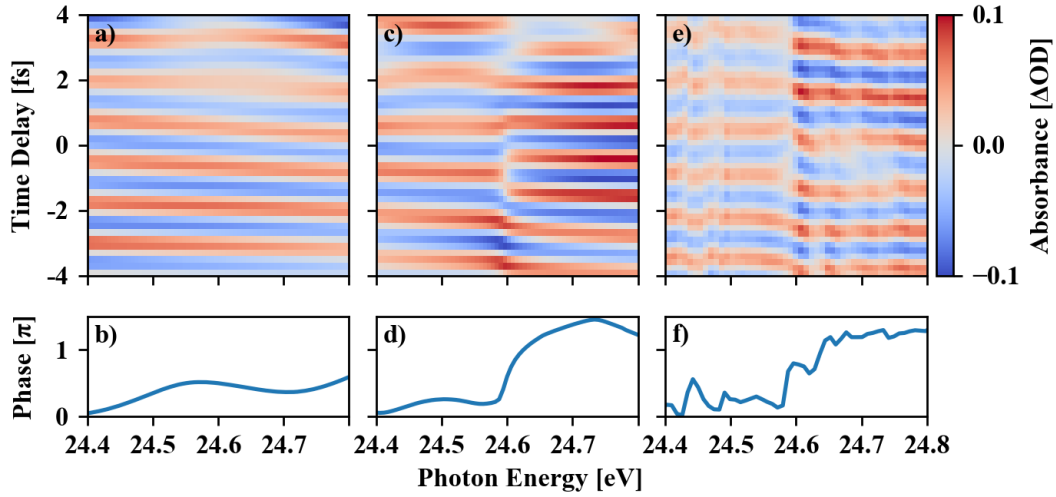

Figure 5.9: Phase-shift of the half-cycle oscillation of the absorption across the ionization threshold. a) The simulated absorbance without continuum states. The phase of the oscillation is almost flat as a function of the photon energy average over delays between -4 and 4 fs shown in b). c) The half-cycle oscillation of the absorbance with including the continuum state in the simulation. Here a phase step of the oscillation is visible between photon energies below and above the threshold that is shown in d). e) The measured change in absorbance showing the phase step that is quantified in f).

The results of the numerical model simulation can be used, as shown above, as a toy experiment yielding a time-delay-dependent absorption spectrum. With this, one can reconstruct the time-dependent dipole moment from the absorption spectra similar to previously done with the measurement spectra. Figure 5.10 shows the reconstructed amplitude of the dipole resulting from the simulation in a) and again from the measurement in b). Here, one can directly reproduce the oscillation of the amplitude for short real times. A possible explanation of this oscillation will be given

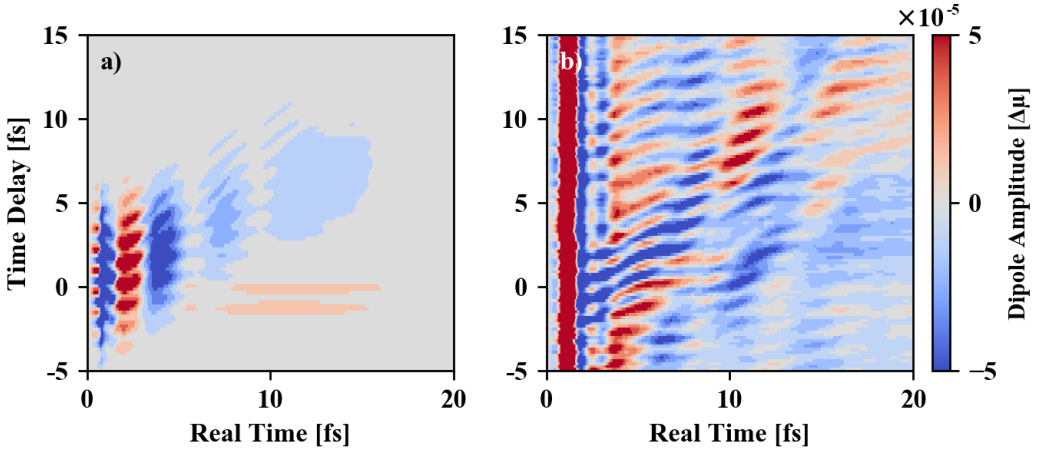

Figure 5.10: Comparison of the time and time-delay-dependent dipole response of the ionization threshold. a) The simulated NIR-induced change of the dipole response of only the threshold. A drop and revival of the response in real time that is observed in the measurement is reproduced. b) A zoom-in in the change of the measured dipole response from figure 5.3.

further below, whereby first, the model of the continuum used in the simulation should be tested, and the origin of the hyperbolic-like structure in the absorption is identified.

Continuum Modeling by a Numerical Grid Potential

The above-described modeling of the continuum states has the advantage that one has ready access to all parameters, like the coupling strength between bound and continuum states or one can simulate with or without the continuum. However, only one continuum with the p-symmetry is considered, and, in principle, also the continuum with s- and d-symmetry may change the final results. Furthermore, the choice of the model, i.e., the scaling laws with respect to the number of states given by equation 5.11 or 5.13 or the determination of the dipole moments by the hydrogenic atomic structure theory, could influence the final observations.

In order to validate the results, one can compute the energies and dipole moments more rigorously by using a heuristic radial potential of the helium atom that is defined on a numerical grid. The states' energies are then obtained by the diagonalization of the Hamiltonian, which incorporates this potential. Furthermore, one can also calculate the wave function on the grid and thereby obtain numerically the dipole moments between these eigenstates considering the pre-factors for the angular momentum given by equation 5.16. The radial potential is given by[1]

$$V(r) = -\frac{1}{r} - \left(\frac{1}{r} + 1.3313\right) e^{(-3.0634\, r)}, \qquad (5.23)$$

and it is depicted in figure 5.11. Here, it is multiplied by the radial distance r in order to make the potential shape visible despite the singularity at $r = 0$. For small radii, this potential approximates the Coulomb potential as seen by an electron close to the doubly charged helium core, i.e., $\lim_{r\to 0} V(r) = -2/r$. For larger radii, the potential converges to a Coulomb potential of a singly charged core, i.e., the other bound electron completely screens the helium atom. To include also the free continuum

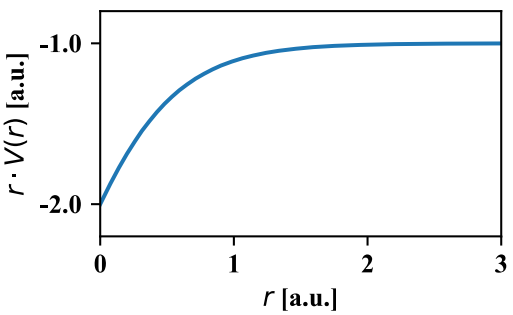

Figure 5.11: The effective Coulomb potential times the radial distance for better visibility. For low radii the potential approximates the Coulomb potential by the doubly charged helium core. For larger radii the other bound electron screens the core and the potential is Coulomb-like with a singly charged core.

[1] The potential and the wave functions together with the state's energies and the dipole moments were developed and calculated by Prof. Dr. Klaus Bartschat.

wave functions as solutions of the Schrödinger equation, the potential is set to infinite at the limit of the grid. Thereby it represents a box potential for large radial distances. The potential reproduces the bound-state energies with an accuracy of about 1%. Furthermore, it presents a systematic way to account (approximately) for the high-lying Rydberg states and the continuous transition to the discretized continuum for higher energies.

The decay constants for the bound states are again set such that the corresponding characteristic lifetimes are 1 ps. For the decay of the continuum states, equation 5.13 is reused. With this, the momentum of continuum state n is calculated by its kinetic energy that is the difference between the total energy and the potential energy

$$E_{n,\mathrm{kin}} = E_n - E_{n,\mathrm{pot}}, \qquad (5.24)$$

and the potential energy is the expectation value of the potential

$$E_{n,\mathrm{pot}} = \int_0^a \psi_n^*(r)\, V(r)\, \psi_n(r)\, r^2 dr, \qquad (5.25)$$

where a is the grid size. The two free parameters, the grid discretization step size, and the total grid size, determine the number of states within a given energy interval and the number of bound states in the system. The total number of states is 400, and it is set such that it is similar to the number used for the modeling of the continuum in the previous section.

The behavior of the resulting total energy, the potential energy, and the kinetic energy given by the heuristic potential of equation 5.23 versus the state number is depicted in figure 5.12 a), where zero energy is set to the ionization threshold. For the first few states, the total energy is negative, and therewith they correspond to the bound states of the system. At the ionization threshold around state number 20, the curve becomes flat, indicating a high density of states, and above the threshold, the increase of the total energy with the state number is again approximately quadratic like it is the case for the previous continuum model in a box potential described above. The potential energy is negative for the bound state and zero for the continuum states above the threshold, representing the free electrons that are almost unaffected by the Coulomb potential of the residual ion.

The advantage of the here presented model is the continuous change of the density of states energetically across the ionization threshold from Rydberg-like to an n^2-dependence in a box potential, see figure 5.12 b). Similar to the previous model of the continuum, the dipole moment from the ground to the dipole-allowed 1snp manifold of excited states shows a minimum at the threshold. Therewith the divergence of the density of states at threshold is compensated by the low occupation of these states due to the low dipole moments from the ground state. In the figure 5.12, only the properties of the states with p-symmetry are shown. However, this model includes all continuum states with the relevant symmetries, i.e., the s-, p- and d-symmetries, which show similar behavior of their properties. With this model,

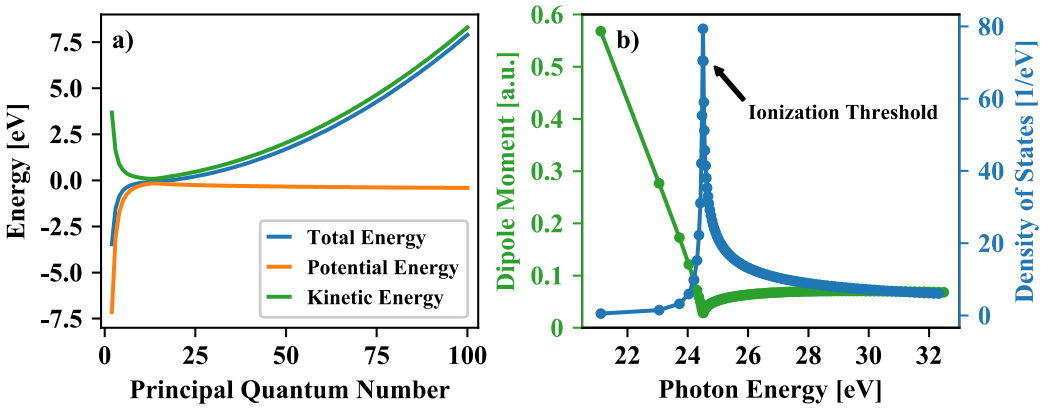

Figure 5.12: The energies and the states' properties of the atomic model resulting from the heuristic helium potential given by equation 5.23. a) The total, potential, and kinetic energy versus the number of the state in the simulation. Negative energies for the total energy corresponds to bound states and positive energies to continuum states. The trends of the energies are discussed in the main text. b) The dipole moment from the ground to excited states of the 1snp manifold and the density of states for different photon energies. At the threshold the density of states diverges, whereby the dipole moment tends to zero and increases again for higher energies, i.e., to the smooth continuum.

one can therefore test whether the even-parity continua affect the time-dependent absorption spectrum.

The resulting absorption spectra, together with the Fourier signal with respect to the time delay, are shown in figure 5.13. Here many features that are also observed in the measurement are reproduced. In particular, the hyperbolic structure above the ionization threshold is still present, and it leads to the diagonal Fourier feature pointing to the ionization threshold, see subfigure b). To conclude, the laser-induced hyperbolic-like structure is not sensitive to the exact modeling of the continuum, but instead, it is a universal feature of the field-driven response of an ionization threshold.

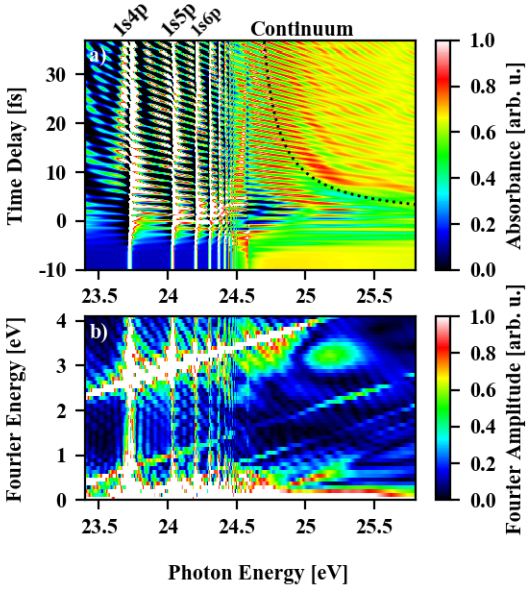

Figure 5.13: Simulated time-delay-dependent transient absorption spectra with the He+ potential. a) The absorption at the first ionization threshold. The hyperbolic structure above threshold is reproduced and indicated by a dotted curve. (b) Fourier amplitude with respect to the time-delay axis in (a). The fast and slow oscillations generate diagonal Fourier signals. The hyperbolic structure leads to a diagonal above the threshold and at low Fourier energy similar to the observation in the measurement.

Laser-Induced Ponderomotive Shift on the Continuum

Making use of the modularity of the multi-level model, one can obtain further insight into the origin of the hyperbolic structure in the time-delay-dependent absorption spectra above the ionization threshold. One can switch off the NIR-induced dipole couplings between the excited bound and continuum states by artificially setting their dipole moments to zero. Instead, the NIR pulse should artificially induce only an energy shift on the free electron's energy, expressed in atomic units by:

$$E_i(t) = \frac{\left(p_i - A(t)\right)^2}{2}. \qquad (5.26)$$

Here $A(t) = -\int_{-\infty}^{t} F_{\mathrm{NIR}}(t')dt'$ is the time-dependent vector potential of the NIR electric field expressed in atomic units, which adds a ponderomotive shift to the energy $E_i(t)$ of the continuum states with momentum p_i. Since the square in the numerator in equation 5.26 introduces a mixing term of the kind $p_i A(t)$, the free time evolution of the state given by equation 5.8 will depend on the sign of the momentum. This sign represents the spatial propagation direction of the electrons in the polarization plane of the laser pulses. However, in the experiment, the total dipole signal is generated by an ensemble of ionized atoms with equal distribution for negative and positive signs of the free electron's momentum. Thus, in order to account for this isotropy of the electron's propagation directions, one has to double the number of continuum states in the simulation. These two continuum manifolds have positive and negative momenta and therewith a different time evolution. In the end, one has to coherently add up their contributions to the total observed time-dependent dipole given by equation 5.9 and use this to calculate the photoabsorption cross-section.

The resulting time-delay-dependent absorption spectrum, shown in figure 5.14, readily shows the hyperbolic structure at the continuum threshold, as observed in the measurement. Thus, the ponderomotive energy shift (or ac-Stark shift, if the dipole couplings between the bound and continuum states are included) is sufficient to qualitatively explain the typical time-dependent perturbed response of the continuum onset. Note that the Fourier signal at low Fourier energy, shown in the subfigure b), is almost symmetric around the ionization threshold. However, in the measurement, the signal below the threshold is suppressed, which is probably due to the domination of Fourier signatures resulting from couplings between high-lying Rydberg states with the ionization continuum. Furthermore, the ponderomotive energy amounts here to only ~0.2 eV, much smaller than the NIR photon energy of 1.6 eV. Thus, as discussed in the fundamentals, this NIR field strength is often considered to be weak. However, here a clear strong-field-induced ponderomotive dressing effect is

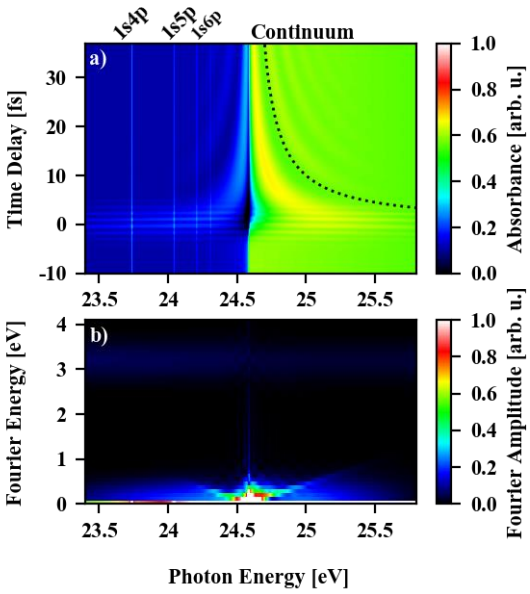

Figure 5.14: Effects on the attosecond transient absorption spectra, where the NIR only introduces a ponderomotive shift onto the continuum states' energy. a) The simulated time-delay-dependent transient absorption spectra. The hyperbolic-like feature above the ionization threshold is reproduced indicated by a dotted curve. b) The amplitude of the Fourier transform with respect to the time delay in a). The hyperbolic structure leads to a diagonal Fourier feature pointing to the threshold similar to what is observed in the measured spectra.

identified, owing to the high sensitivity to small energy shifts within XUV transient absorption spectroscopy.

Signatures of Electron Recollision

In the real-time-and-time-delay-dependent dipole response spectrally at the ionization threshold, a revival structure appears, which follows the NIR after the XUV excitation, i.e., at positive time delays, shown in figures 5.3 and 5.10. Since the spectral window used in the reconstruction of the dipole is above the ionization threshold, the response corresponds to atomic states representing the free electron in the ionization continuum. Thus, one might explain the revival structure with the free electron's wave packet being pushed back into the parent ion forced by the NIR field, which can be interpreted as XUV-excited and NIR-driven recollision of the electron.

To test this hypothesis, a framework is needed that links the increase of the dipole moment with the center of gravity of the wave packet's amplitude representing the free electron. For this purpose, another simulation is conducted based on solving the time-dependent Schrödinger equation on a spatial grid. The following shall introduce the model of the simulation where further details can be found in the references [110].

The time propagation is achieved using a split-step algorithm again. Here, the evolution of the wave function represents the spatial dynamics of a single electron of the helium atom. Its other electron is not active and just screens the charge of the helium core. This assumption is known as the single-active-electron approximation. Furthermore, since previous studies show good reproducibility of the main features observed in measured absorption spectra with models using reduced spatial dimensionality [147], the propagation of the wave function is calculated on a single

spatial dimension x. This provides some computational simplicity and lowers the numerical costs. Here, the total grid size is ± 512 a. u., with a spatial grid step size of $\Delta x = 0.25$ a. u. resulting in a total number of grid points of $N = 4096$.

The electron is subjected to a Coulomb potential of a singly charged core. Since this potential exhibits a singularity at the origin, it leads to numerical troubleshoots or artifacts. To avoid this, commonly, the potential is smoothed out in the origin by substituting it with a so-called soft-core potential [147]. Furthermore, to account for the decrease of the wave packet when the electron leaves the vicinity of the parent ion, an imaginary potential $iV_{\mathrm{Bound}}(x)$ is added to the soft-core potential at the boundaries of the spatial grid. This results in a spatially dependent decrease of the wave function at the edges of the grid during its time propagation. The effects of this absorbing boundary on the behavior of the wave function together with different set parameters of the soft-core potential are discussed in [110]. The total potential is then expressed in atomic units by

$$V(x) = \frac{-1}{\sqrt{x^2 + a}} - iV_{\mathrm{Bound}}(x). \qquad (5.27)$$

Here a = 0.483 is set such that the first unbound eigenstate of the laser-field-free Hamiltonian has an energy of 24.58 eV, i.e., the energy of the first ionization threshold in helium. The potential is shown in figure 5.15.

The interaction of the electron with the electric field $F(t)$ of the combined NIR and XUV pulses is defined in the length gauge using the dipole approximation. With this, the total Hamiltonian reads in atomic units

$$\hat{H}(x, p, t) = \frac{p^2}{2} + V(x) - xF(t), \qquad (5.28)$$

where p is the momentum of the wave function. The propagation of the wave function in time using the split-step method is then given by

$$\psi(x, t + \Delta t) = e^{-i[V(x) - xF(t)]\frac{\Delta t}{2}} \cdot \mathcal{F}^{-1}\left[e^{-i\frac{p^2}{2}\Delta t} \cdot \mathcal{F}\left[e^{-i[V(x) - xF(t)]\frac{\Delta t}{2}} \cdot \psi(x, t)\right]\right]. \qquad (5.29)$$

Here, $\mathcal{F}$ and $\mathcal{F}^{-1}$ denotes the Fourier transformation and back-transformation along the spatial grid dimension, respectively.

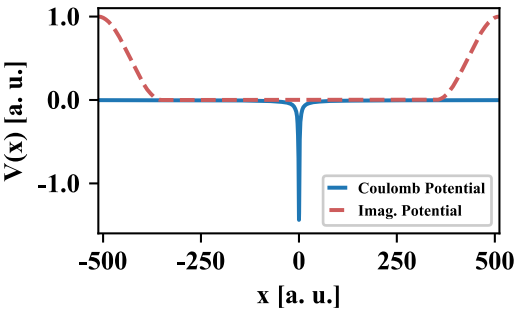

Figure 5.15: Spatial model potential of the helium atom for a single active electron defined on an numerical grid in one dimension. The Coulomb potential (solid blue) of the atomic core is approximated by a soft-core potential to avoid the singularity at the origin. The imaginary potential (dashed red) provides the absorbing boundaries at the edges of the grid.

The resulting absolute value of the wave function is presented in figure 5.16 b), where for better visibility, the difference of the wave function is shown given by

$$\Delta\psi(x,t) = |\psi(x,t)| - [|\psi_{\mathrm{NIR}}(x,t)| - |\psi_0(x)|] - [|\psi_{\mathrm{XUV}}(x,t)| - |\psi_0(x)|] - |\psi_0(x)|. \quad (5.30)$$

Here $\psi_{\mathrm{NIR}}(x)$, $\psi_{\mathrm{XUV}}(x)$, and $\psi_0(x)$ denote the wave functions if only the NIR or XUV pulse is present in the simulation and the initial ground state wave function, respectively. The pulses which drive this wave function are depicted in subfigure c), where the XUV pulse marks time zero indicated by a violet dashed line. In the figure, one can see several field-induced effects that are marked by letters "a," "b," and "c." Parts of the wave function are directly ionized by the XUV pulse and escape the vicinity of the core, indicated by an "a". Another part is wiggling around the central

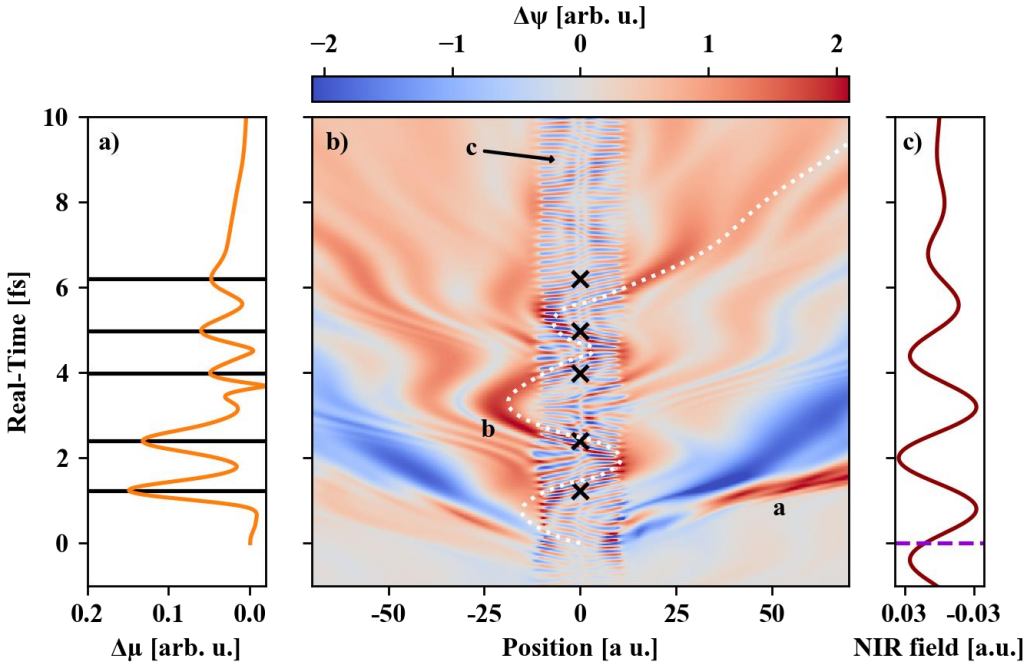

Figure 5.16: Recolliding electron wave-packet dynamics. a) The time-dependent dipole response reconstructed from the absorption spectrum above the ionization threshold. The spectrum is calculated from the dynamics of the wave function in the one dimensional spatial grid simulation. For better visibility the amplitude of the dipole response without an NIR pulse is subtracted from the response in the simulation with NIR. The local maxima of the response are highlighted by black lines. b) Light-induced dynamics of the wave function on the spatial grid. Here a difference in wave function is shown that is defined by equation 5.30 and therewith emphasizes the light-induced dynamics. Different effects are observed: the ionization of the electron marked by an "a", the field-driven wiggling around the center "b" and the wave packet beating of bound states "c". The dotted curve denotes a possible classical trajectory of an electron in both the laser field and Coulomb field calculated by equation 5.32. Black crosses mark the time position of the local maxima of the dipole response from a). c) The used pulses in the one-dimensional grid simulation. The violet dashed line indicates the XUV excitation pulse, which defines time zero and the red curve depicts the NIR electric field. The figure is adapted from [110].

position following the NIR pulse, marked by “b”, and a small fraction oscillates in real-time also for later times and is located close to the center, “c”. The latter represents the beating of the coherently excited bound state wave packet. The wiggling part represents the NIR-driven recollision of the free electron in the atomic core, whereby a small fraction gets bound again, i.e., recombines into the atom, which is visible by the increase of the oscillatory wave function’s amplitude after the first recollision.

With the evolution of the wave function driven by both pulses at hand, one can calculate the absorption spectra via equation 5.3 and using the time-dependent dipole moment

$$\mu(t) = \int_{-L}^{L} \psi^*(x,t)\, x\, \psi(x,t)\, dx, \qquad (5.31)$$

where $L = 512$ a.u. is the boundary of the spatial grid. To compare the simulated results with the measured response, one is interested in the dipole response spectrally above the ionization threshold. Therefore, the absorption spectrum is filtered with the same spectral window used for the measurement, and the time-dependent dipole moment is reconstructed again from the filtered spectrum using its Fourier transform. The so obtained response amplitude is depicted in figure 5.16 a), whereby the response that results from a simulation without the NIR pulse is subtracted, i.e., $\Delta\mu = |\mu(t)| - |\mu_{\mathrm{XUV}}(t)|$. It shows a revival of the response amplitude at different real-times, similar to what is observed in the measurement. The time positions of the local maxima of the amplitude are marked by black lines in a) and crosses in subfigure b). It turns out that the maxima of the response appear when the recollision of the electron wave function happens.

The interpretation that the wave function of the ionized electron recollides with the parent ion can further be tested. For this purpose, the white dotted curve in figure 5.16 b) presents a classical trajectory of an electron, subjected to the Coulomb field of the parent ion and the laser field. Its equation of motion is given by

$$\frac{d^2}{dt^2}x(t) = -F(t) - \frac{d(\mathcal{R}e[V(x)])}{dx}. \qquad (5.32)$$

The exact solution of this equation depends on the initial conditions given by the initial position and the initial velocity of the electron at time zero. Here, it is assumed that the electron is ionized by the XUV pulse, defining the initial time at the position $x_0 = 0$ with the excess energy of $\frac{m_e {v_0}^2}{2} = 0.80$ eV (in SI), i.e., the energy difference of the XUV-ionization photon energy and the ionization potential. The trajectory agrees well with the major part of the wiggling wave function supporting the recollision hypothesis.

The probability of the electron recollision should depend on the polarization of the NIR pulse, similar to the electron recombination probability in the process of high

harmonic generation (HHG). It depends on the ellipticity of the NIR polarization, which is observable by the strong ellipticity dependence of the harmonic yield [108]. In HHG, the ionization mechanism is tunnel ionization, whereby here, the ionization is induced by the XUV pulse. However, the recombination step is similar, a colliding motion of the electron forced by the oscillatory NIR field.

The signature of this polarization dependence can be measured by the presented attosecond beamline using the external interferometer setup, discussed in the chapter on the experimental setup. For this purpose, the polarization of the NIR, which interacts with the target, is switched from linear to circular using a broadband quarter-

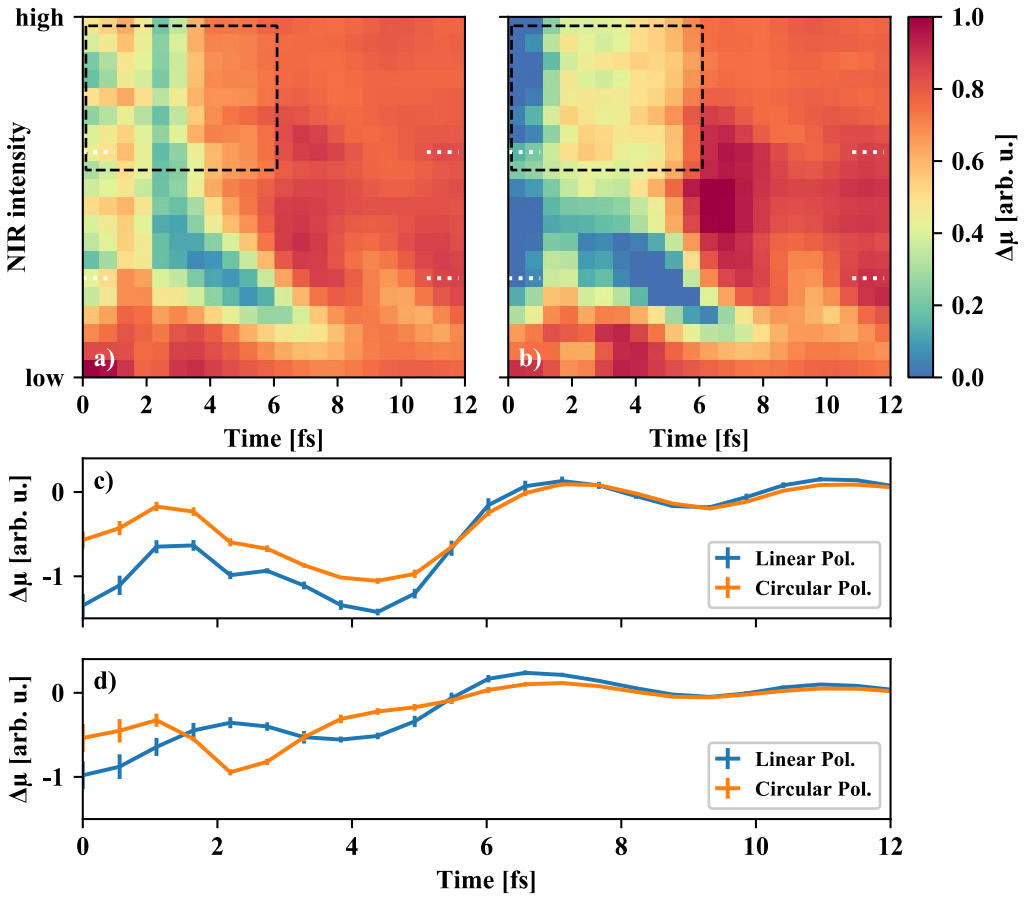

Figure 5.17: Measured intensity-dependent dipole response for linearly and circularly polarized NIR fields. The differences in the dipole response amplitude with and without NIR for the time overlap of the NIR pulse and XUV excitation are plotted. a) The dipole response for the linear polarization. The time positions for the lineouts in c) and d) are marked by white dotted lines. b) The dipole response for the circular polarization. A deviation of the response compared to the response in a) is observed within the black dashed box at high NIR intensities. It might be explained by the laser-driven recollision of the electron into the parent ion. c) Lineouts of the dipole response from a) and b) for low NIR intensities. The responses for the different polarizations are qualitatively the same. The error bars are the standard errors of 12 individual measurements. d) Lineout of the responses for high NIR intensities. Here, the responses significantly deviate from each other pointing to the importance of the electron recollision in the response. The figure is adapted from [110].

wave plate. Figure 5.17 shows the reconstructed dipole response above the ionization threshold for the linear polarization in a) and the circular polarization in b) for different NIR intensities. Here again, the differences in the response with and without NIR is plotted. While for low intensities (~10^{12} - 10^{13} W/cm^2), the response is rather similar; for higher intensities (~10^{14} W/cm^2), the responses significantly deviate from each other within the dashed black box in the figures. For a better visibility, figure 5.17 c) and d) depict exemplary lineouts of the responses for the two NIR intensity regions, marked by dotted white lines in a) and b).

This observed deviation can be explained as follows. For rather low intensities, light-induced states are present in the absorption spectra around the ionization threshold, as discussed above. They rely on the couplings of bound states with one or several NIR photons. This photon picture is a perturbative treatment of the light-matter interaction, which breaks down for high intensities. However, the recollision phenomenon is purely describable in the strong-field limit, similar to the HHG process. Therefore, one might interpret the matching of the responses for low intensities by the domination of contributions from light-induced effects other than the electron recollision. For high intensities, however, the presence of light-induced states is suppressed, and the response might be mainly governed by the recollision of the ionized electron, which is a response that depends on the polarization of the NIR field.

6. The Build-up of the Dipole Response

Ultrashort and intense laser pulses have been successfully used to gain knowledge in (correlated) electron dynamics within atoms or molecules on their natural timescale [21,23,148,149]. As a notable example, using these pulses, it was possible to resolve the laser-induced dynamics of and between autoionizing states in time [24,57]. As introduced in the fundamentals chapter, these states are excited states that are degenerate with and coupled to an ionization continuum via configuration interaction [66]. It results in the interference of quantum-paths of the direct ionization of the atom and the ionization via the excited states. The spectroscopic signature of this interference is an asymmetric absorption line shape, the so-called Fano-line shape. Here, key physical questions are how the quantum-paths interference emerges and how long it takes. These had been theoretically predicted first [150–155] and later experimentally investigated for the case of the 2s2p doubly excited state in the helium atom using photoelectron [156] as well as attosecond transient absorption spectroscopy [31].

In the absorption spectroscopy measurement, the formation of the 2s2p Fano-shaped absorption line has been probed in time directly from the measured XUV absorption spectrum. This was done by temporally gating the XUV-excited dipole response of the helium atom by means of time-delayed depletion of the 2s2p state using strong-field-ionization by an intense few-cycle NIR laser pulse. The measured build-up of the Fano resonance was compared to absorption spectra resulting from an *ab initio* simulation and an analytical gating model. In the model, the response of the isolated Fano resonance was excited and depleted impulsively, similar to the approach used in the dipole control model that is introduced in the fundamentals chapter.

The results of this study lead to further crucial questions. First, typically used analytical models of strong-field ionization are often based on the single-active-electron approximation [42,157]. In these, only the (often) outermost electron is considered in the ionization process, while the role of the other electrons of the atom is assumed to merely screen the charge of the atomic core. However, for the case of the doubly excited states, the electrons are highly correlated, and one question is how this correlation is imprinted in the ionization. Recently, theoretical work addresses the quantum dynamics of two active electrons during the process of strong-field ionization [158–161]. Second, what are the dynamics during the build-up not for only an isolated resonance but for a coherently excited wave packet involving multiple excited states? Resolving their build-up simultaneously could provide a more comprehensive time-domain understanding of electron dynamics influencing the

build-up. Third, as stated in reference [31], in order to time-resolve the resonant build-up dynamics, the closing time of the strong-field-ionization gate needs to be shorter than the natural decay time of the XUV-excited states, which corresponds to the build-up time of resonant absorption features. For instance, the bound doubly excited states in helium have an autoionization decay time on the order of 100 fs or longer, and therewith this condition is fulfilled for an NIR pulse of 5 fs duration. However, the question arises whether the approach of gating the dipole response by strong-field-ionization is also applicable to other even faster decaying states, e.g., the continuum states in close proximity to the ionization threshold. To address this question, one should ideally quantify here the gating fall time within the strong pulse, where the pulse duration only represents an upper limit. Fourth, as discussed in the previous chapter, the NIR-induced ponderomotive energy shifts on the resonant and continuum states have a non-negligible impact on the absorption spectra. Thus, is it possible to derive a gating model including the energy shift and which goes beyond the impulsive analytic gating model? Such a model would deliver a more intuitive understanding of the ongoing physics in contrast to *ab initio* model simulations, which are comprehensive but less descriptive.

The following study presented in this chapter provides first steps to tackle these questions. First, a strong-field-ionization gating model is introduced, which incorporates the NIR-induced ponderomotive energy shift and takes into account the temporal shape of the NIR intensity. The model is then applied to gate the responses of two distinct spectral regions. These are the ultrafast response of multiple doubly excited states converging to the $N = 2$ ionization continuum of the excited helium ion and the singly excited Rydberg series, including the first ionization threshold. For a better comparison of the modeled and the measured absorption spectra, the measured dipole response is used as an input response, which results from the reconstruction of the time-dependent dipole moment of the measured static absorption spectrum without NIR. With this, the spectral signatures in the observed absorption are identified that are caused by a non-perfect impulsive ionization gate.

As a result, with the gating model, the build-up of the absorption lines in the doubly excited spectral region is determined. Furthermore, the separations of the partly overlapping Fano resonances are resolved in time. For the singly excited spectral region, the similar transient absorption spectra are shown as discussed in the previous chapter. However, here the intensities of the NIR laser are at least one order of magnitude higher ($\sim 10^{13}\,\mathrm{W/cm^2}$ or higher), beyond the range where modifications in the transient absorption spectra can be interpreted as a ponderomotive energy shift. At the end of the chapter, the build-up of the dipole responses of both spectral regions is presented in the time-domain, where the strong-field-driven dynamics during the ionization of the XUV-excited coherent wave packets can be resolved. With this, it is possible to quantify the gating fall time and the gating time position within the strong few-cycle laser pulse. Furthermore, first indications of deviations from the

single-active electron approximation are observed in the ionization-gated response. Parts of the presented results have been published in the reference [2], and therefore the discussion will closely follow the publication.

The Strong-Field-Ionization Gate Model

Time-delay-dependent absorption spectra typically show features of different processes during the interaction between the target atoms and the strong laser field. The following will assign some of the features to the corresponding strong-field processes. Figure 6.1 a) depicts in blue the unperturbed dipole moment for the first 10 fs for the energy region of the doubly-excited Rydberg series of helium starting from the sp_{23+} up to the $N = 2$ continuum. Here, the response is reconstructed from the static XUV absorption with the help of the dipole reconstruction method, which is described in fundamentals and in the reference [50]. In this method, the continuous background absorption of the $N = 1$ continuum is subtracted from the total absorption spectrum before reconstruction, which leads to a dipole response starting at zero for zero time, and it is oscillating around zero. The visible beating of the response in time reflects the coherently excited wave packet of the series. From the dipole moment, one can then get back to the absorption spectra using Fourier transformation shown in figures 6.1 c), f), and i).

The ionization of XUV-excited states leads to the gating of the dipole moment, switching it off when the sudden ionization takes place. This gate can be approximated by a Heaviside gate, i.e., a function

$$G_\theta(t) = 1 - \theta(t - \tau_G), \qquad (6.1)$$

which is multiplied with the time-dependent dipole moment, see figure 6.1 b). Here, $\theta(t)$ is the Heaviside function and τ_G denotes the time delay between the XUV-excitation pulse and the strong NIR pulse. The resulting dipole moment is depicted in orange in figure 6.1 a), which overlays with the blue unperturbed response and suddenly vanishes at 5 fs, the time when the gate acts on it. By scanning the time delay τ_G of the gate, one obtains the time-delay-dependent absorption spectra for this gated response shown in figure 6.1 c). For negative delays, i.e., when the gating laser pulse precedes the excitation of the dipole, no gating takes place, and the absorption spectra are given by the static spectrum as if no gating laser were present. For positive delays close to zero, the dipole moment is suppressed so fast after the excitation that it leads to a flat absorption and, for slightly later delays, to a strong broadening of the absorption lines of the Rydberg series. For delays of 10 fs or higher, individual absorption lines start to form, regaining the shape of the static absorption for very large delays. The investigation of this time-delay-dependent formation of the absorption is at the heart of this build-up study of the dipole response at an ionization threshold.

The sudden suppression of the dipole moment in time leads to spectral side lobes around the absorption lines. The energy positions of these are time-delay-dependent, and they converge to the parent absorption lines for higher delays. In the time-delay absorption spectra, they show up as hyperbolic-like features around the lines. As will be seen further below, the strength of these hyperbolic features is overemphasized

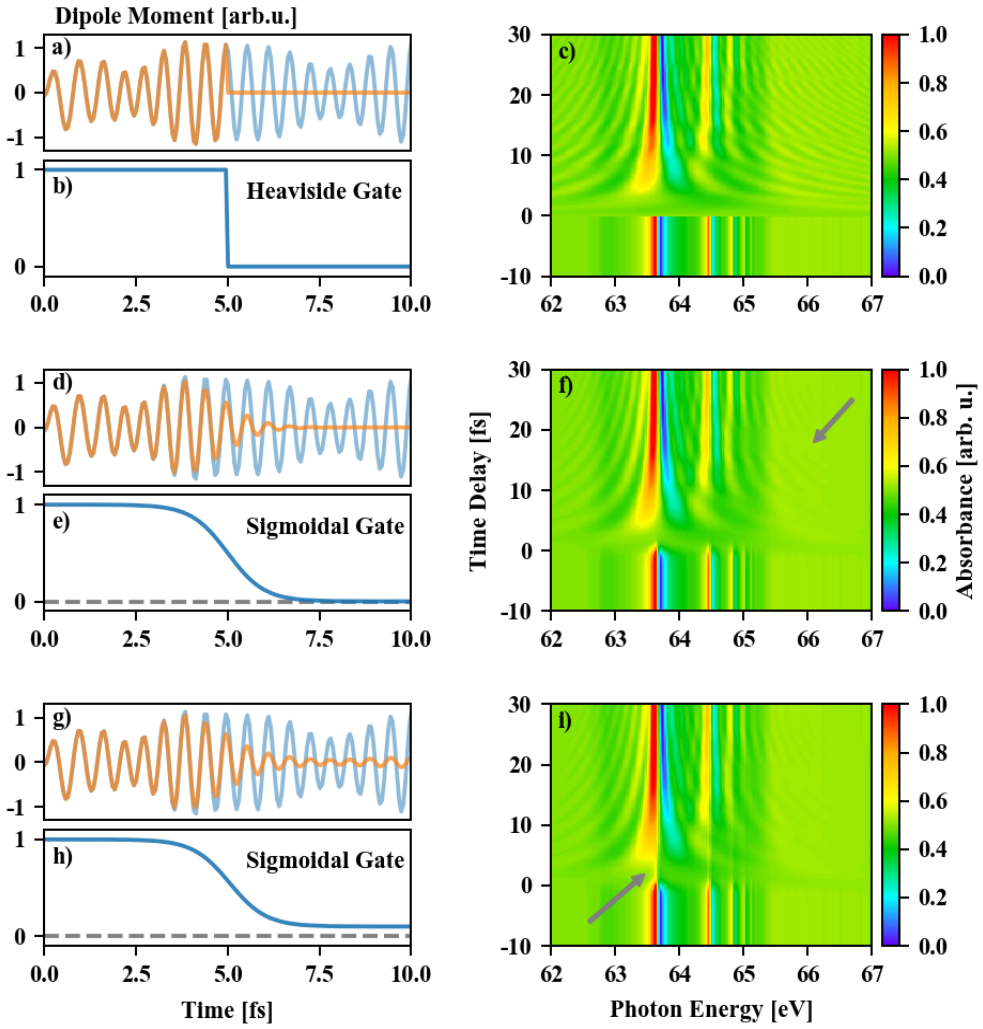

Figure 6.1: Ionization gating model. a) The unperturbed time-dependent dipole moment in blue is truncated at 5 fs (orange line). b) Heaviside gate function centered at 5 fs that is multiplied with the dipole moment. c) Absorbance spectra for different time delays using the Heaviside amplitude gate. Details of the visible features are discussed in the text. d) Unperturbed dipole moment (blue) and the moment which is gated by an sigmoidal gate function centered at 5 fs (orange). e) The sigmodal gate function used in subfigure d). f) Time-delay-dependent absorption spectra for the sigmoidal gate. The arrow indicates the decrease of the hyperbolic structures caused by the gating function is smooth in time. g) Unperturbed (blue) and gated dipole moment (orange) in the case of a sigmoidal gate which suppresses the dipole to 10% for long times. h) The sigmoidal gate with the maximal suppression of 10% for long delays . i) The resulting absorption spectra for the 10% sigmoidal gate. A weak residual absorption line is visible for time overlap due to the incomplete suppression.

compared to the features in the measured spectra due to the sharp gate given by the Heaviside function. To smooth out this effect, one can approximate the gate function by a sigmoidal function shown in figure 6.1 e), which is given by the equation:

$$G_{\mathrm{S}}(t) = 1 + \frac{1}{e^{\frac{t-\tau_{\mathrm{G}}}{\Sigma}} + \frac{1}{A_{\mathrm{G}}}} - \frac{1}{e^{\frac{-\tau_{\mathrm{G}}}{\Sigma}} + \frac{1}{A_{\mathrm{G}}}}. \qquad (6.2)$$

Here, τ_{G}, Σ, and A_{G} are the gate time position, the gate fall time, and the gate amplitude, respectively. In the equation, the middle term is an inverted sigmoidal function, and the other terms ensure that the gate starts for $t = 0$ at unity for every time position τ_{G}. The resulting dipole response, gated at 5 fs delay, is shown in orange in figure 6.1 d) again together with the unperturbed moment in blue. Instead of a sudden vanishing, here, the dipole moment decreases smoothly to zero around the gating time position. The resulting time-delay-dependent absorption spectra are depicted in figure 6.1 f). Utilizing the smoother gate suppresses the strength of the hyperbolic features, which is indicated by the grey arrow. Furthermore, the sharp step at zero time delay disappears compared to the spectra with the Heaviside gate function.

Under experimental conditions, the strong NIR may not completely ionize all target atoms. Thus, a more realistic gate would not suppress the dipole moment completely. Figure 6.1 h) shows a sigmoidal gate located at 5 fs, which falls only to 10% for longer times. The resulting dipole moment, shown in orange in figure 6.1 g), decreases around 5 fs but is not entirely suppressed. In the corresponding time-delay-dependent absorption spectra, figure 6.1 h), the small residual absorption series appears for short positive delays, which is indicated by the grey arrow in the figure. Although this residual absorption line signal is also visible in the measured absorption presented below, in the simulated absorption, the line shapes deviate from the experimentally observed ones. As in the chapters above described, the line shape is linked to the phase of the dipole moment.

A second laser-induced process is the energetic shift of the oscillating dipole moment due to either ponderomotive or ac-Stark shifts of the energies of the states in the Rydberg series. In first approximation, the short laser pulse effectively induces a phase step onto the dipole moment centered in time at the time delay of the pulse, see figure 6.2 b) for an example of a π phase step. The resulting time-dependent dipole is depicted in orange in figure 6.2 a) together with the unperturbed moment in blue, where the phase step is added (or subtracted depending on the definition of the Fourier transformation) to the phase of the dipole. This phase jump leads in the time-delay-dependent absorption spectra again to the hyperbolic features, see figure 6.2 c). In addition, the shapes of the absorption line are inverted for short positive delays and switch back to the unperturbed shapes for higher delays.

Now, in analogy to the gate model for the amplitude of the dipole moment, the continuous phase shift is introduced. One example is shown in figure 6.2 e). This laser-induced phase is calculated by a ponderomotive shift that a modeled laser pulse of $\sinh^2$-shape would induce with a central photon energy of 726 nm, FWHM pulse duration of 2 fs, and 20 TW/cm^2 peak intensity; see equation 4.9. The corresponding dipole moment and the absorption spectra are shown in figure d) and f), respectively.

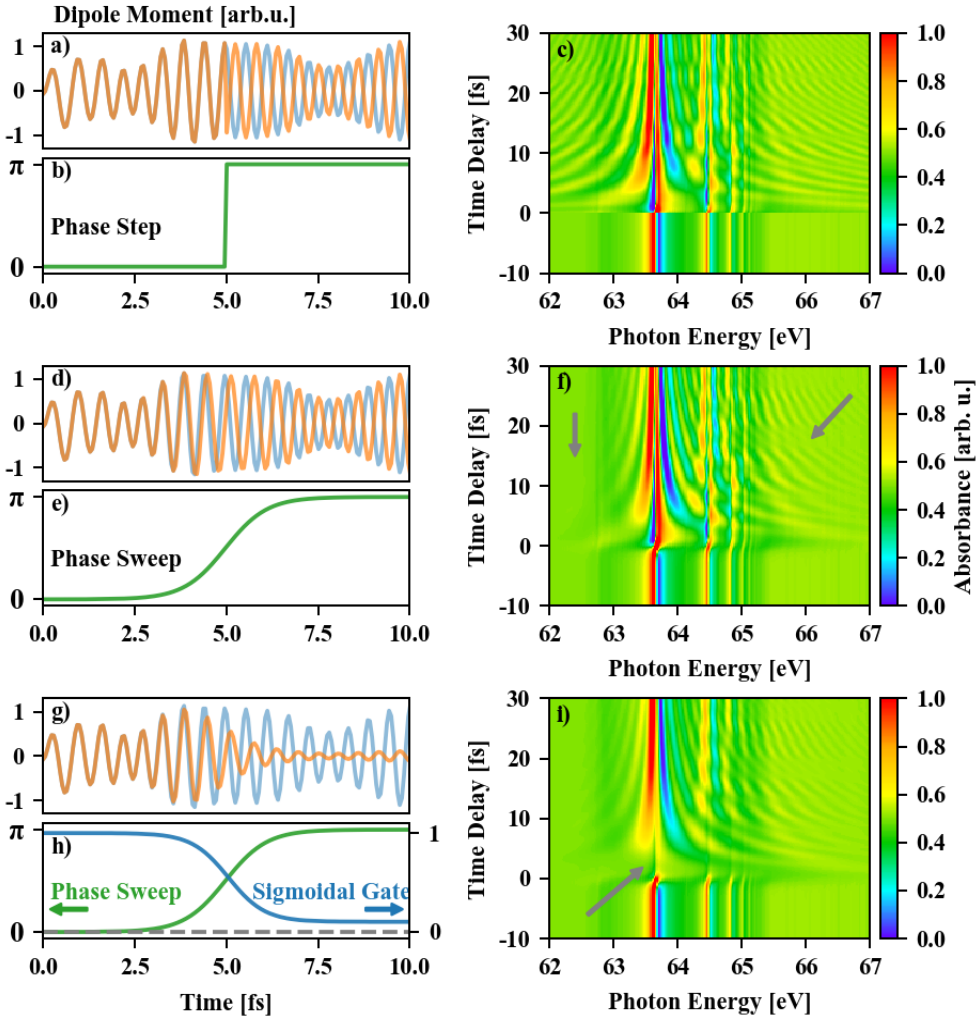

Figure 6.2: Laser-induced phase shift model. a) The unperturbed time-dependent dipole moment in blue is instantaneously shifted in phase at 5 fs (orange line). b) Phase step function centered at 5 fs that is used to shift the phase of the dipole moment. c) Absorbance spectra for different time delays of the phase step function. Details of the visible features are discussed in the text. d) Unperturbed dipole moment (blue) and the moment which is smoothly shifted in phase by ponderomotive shift using a $\sinh^2$-shape laser pulse (orange). e) The phase sweep function used in subfigure d). f) Time-delay-dependent absorption spectra with the phase sweep centered at different time delays. The arrows indicate the changes of the hyperbolic structures caused by the phase sweep. g) Unperturbed (blue) and gated and phase shifted dipole moment (orange) in the case of a sigmoidal gate and smooth phase sweep. h) The sigmoidal gate and phase sweep used for g). i) The resulting absorption spectra for the combination of the sigmoidal gate and phase sweep.

The inversion of the line shapes for short positive delays, and the convergence to the unperturbed shapes for longer delays persist with this phase sweep. However, as in the evaluation of the gate, the strength of the hyperbolic structure decreases, but in this case, the suppression is greater for the low energy side compared to the high energy indicated by the grey arrows in figure 6.2 f).

Both discussed laser-induced processes, i.e., the strong-field ionization and the energy shift, take place simultaneously. Figure 6.2 g) and i) show the time-dependent dipole and the corresponding time-delay-dependent absorption spectra of the response, which is gated by the sigmoidal function and the phase of which is shifted by the phase sweep, depicted in figure 6.2 h). For short positive delays, the absorption lines are broadened due to the ionization, and their shapes are modified due to the phase shift. The combination of both processes lets the absorption lines effectively appear to emerge from higher energies marked by the grey arrow figure 6.2 i), and they converge to the (lower) energy and shape of the unperturbed series for longer delays. Note that the formation of the series, in this case, is limited neither by the gate fall time nor by the phase sweep duration since the build-up of the absorption lines shows similar timescales as for the instantaneous step cases in figure 6.1 c) and 6.2 c). However, for longer durations of the intense laser pulse, the gate fall time or the phase sweep duration can dominate the timescale, such that information about the duration of the build-up can become blurred. Through evaluating the time-dependent dipole moment, one may characterize the gate fall time for different time delays, which will be demonstrated further below.

The two processes are generally not separable and are induced by the same intense laser pulse. Thus, by changing the pulse settings, both processes will change their strength in a correlated way. Furthermore, at some peak intensity of the pulse, the ionization process can saturate, meaning if most of the atoms in the target ensemble are ionized, no further ionization will be possible. This can also happen already at the tails of the pulse. To account for this ionization saturation, the gate acting on the dipole amplitude can be modeled with the help of a rate equation for the time-dependent number of atoms not yet ionized $N(t)$. This is possible since the strength of the dipole scales linearly with the number of excited – but not ionized – atoms in the target. The rate equation reads:

$$\dot{N}(t) = -\sigma\, \Phi(t) N(t). \qquad (6.3)$$

Here, σ is the single-photon ionization cross-section of the excited target and $\Phi(t)$ denotes the time-dependent photon flux of the ionizing laser pulse,

$$\Phi(t) = \frac{I(t)}{\hbar\omega}, \qquad (6.4)$$

where $I(t)$ is the time-dependent intensity of the pulse. In first approximation, only the central photon energy $\hbar\omega_c$ of the pulse is considered. Furthermore, the rate equation is given for single-photon ionization, but higher orders, i.e., multi-photon or

tunnel ionization, might be possible for a sufficiently intense pulse. The rate equation model leads to the time-dependent gate:

$$G(t) = e^{-\int_0^t \sigma \frac{I(\tilde{t},\tau_G)}{\hbar\omega_c} d\tilde{t}} \approx e^{-\sum_{\tilde{t}=0}^{t} \sigma \frac{I(\tilde{t},\tau_G)}{\hbar\omega_c} \Delta\tilde{t}}, \qquad (6.5)$$

where Δt is the numerical time step size of the model.

Figure 6.3 shows this gate calculated by a pulse with a $\sinh^2$-shaped intensity profile with peak intensity of 17 TW/cm^2, a central wavelength of 710 nm and a pulse duration of 5 fs FWHM, see the grey curve in figure part a). Here, the cross-section of $\sigma = 10$ Mb is taken. The lines of different colors depict the gate for different time delays. Coming from negative delays (-5 fs in blue), where the gate decreases the dipole amplitude to only about 90%, the gate drops very rapidly when the time delay is scanned across zero (from -2.5 fs in orange to overlap in green and +2.5 fs in red). The violet line shows the gate for 10 fs time delay, that is the time the depicted pulse is centered around. Note that this gate already drops to ~20% when the center of the pulse is passing, as is indicated by a vertical dashed line in the figure. Thus, the leading edge of the pulse is sufficiently intense to almost ionize all atoms in the target. However, despite this saturation effect, the gate does not drop to 0 when the pulse is gone for late times. Note, the gate fall time depends on the shape of the leading edge of the strong laser pulse and, in particular, it is less dependent on the total pulse duration. In the experiment, the pulse often consists of a central spike with satellite pulses; see the experimental setup chapter. Thus, one typically can achieve gate fall times shorter than the pulse duration used for the gate.

Figure 6.3 b) shows the phase for different time delays, which are induced by the ponderomotive potential of the laser pulse in grey. Unlike the gate, the laser-induced phase is time-symmetric with the pulse, i.e., its inflection point is at the center of the pulse. Thus, given a sufficiently intense pulse, line-shape changes of the absorption are retarded to the suppression of the line amplitude by the ionization gate.

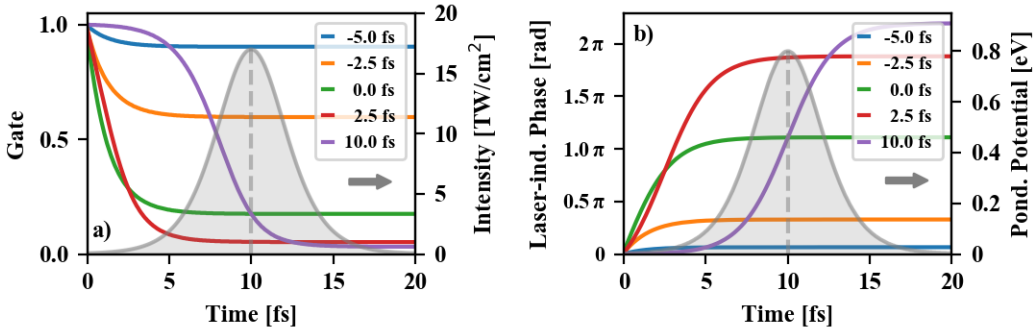

Figure 6.3: The ionization gate model using the ionization rate of the atoms within the laser field. a) Amplitude gate, which is multiplied with the time-dependent dipole moment for different time delays of the gate. The laser pulse used to calculate the gate by equation 6.5 is shown in grey. b) Phase shift which is introduced to the phase of the dipole for different time delays. The ponderomotive potential to calculate the laser-induced phase by equation 4.9 is shown in grey.

The Build-up of an Ionization Threshold and Doubly Excited Rydberg Series

Using the introduced ionization gate model, equation 4.9 and 6.5, one can obtain the time-dependent absorption spectra of the doubly excited Rydberg series, presented in figure 6.4 b), and quantitatively compare it with the experimentally observed spectra in figure 6.4 a). The unperturbed time-dependent dipole moment that is gated by the model and used to calculated the absorption spectra is obtained by reconstructing the dipole moment from a measured static absorption spectrum without NIR. The central wavelength of $\lambda = 726$ nm and pulse duration of $\tau = 5.5$ fs of the $\sinh^2$-shape pulse used for the gating model are experimentally measured. The peak intensity of $I = 12$ TW/cm^2 and the ionization cross-section $\sigma = 12$ Mb are estimated by the ponderomotive shift and the line suppression visible in the experiment, respectively.

The agreement between the measured and the modeled spectra is remarkable. All of the earlier discussed features, i.e., line broadening, energy shifting, line-shape changes, and hyperbolic structures, are well reproduced. It is worth to point out that the here presented modeled spectra are only obtained by the Fourier transform of the time-dependent dipole moment smoothly gated in the time domain. Despite the good agreement, some differences remain. In the experiment, a residual rippling of the absorption versus the time delay is present, in particular for the $sp_{2,3+}$ line. This is due to a two-NIR-photon coupling between the 2s2p (not shown) and the $sp_{2,3+}$ doubly-excited states, which is thoroughly discussed in reference [58].

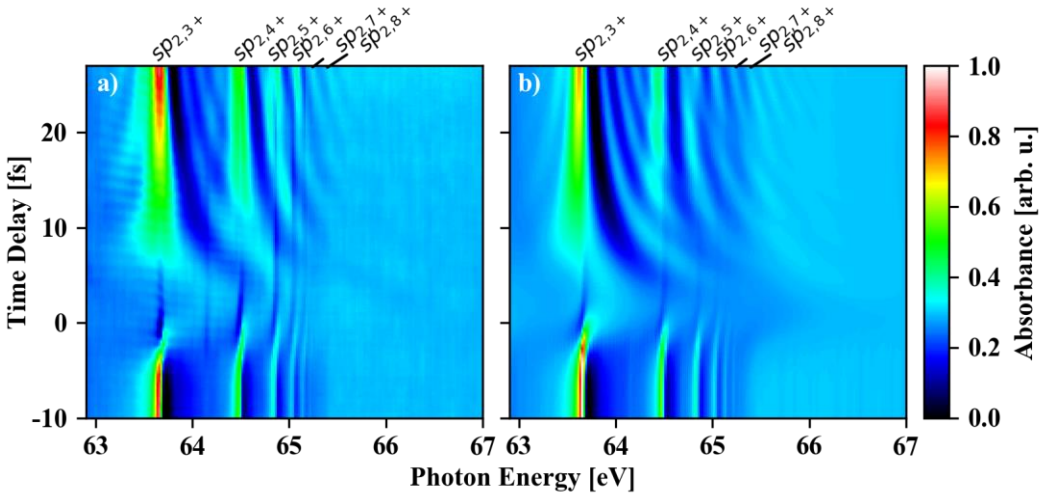

Figure 6.4: Time-delay-dependent absorption spectra of the doubly excited states in helium. Negative delays mean that the gating NIR proceeds the XUV-excitation a) The measured absorption spectra, where the absorption lines are suppressed and the shape of which is modified by the strong NIR pulse around the time overlap of the NIR and XUV-excitation. b) The simulated absorption spectra by the ionization-gating and phase-shift model.

For the higher-lying Rydberg states and the second ionization threshold, some deviations around the time overlap appear. However, due to the small experimental signal here, only little insight can be gained. To increase the visibility of the signal around these higher-lying states and the ionization threshold, figure 6.5 presents the measured and modeled time-delay-depended absorption spectra for the singly-excited Rydberg series in helium. Here, the measured absorption spectra are time-averaged around one NIR-electric-field-cycle in order to suppress sub-cycle oscillation due to resonant couplings, which is not included in the ionization gating model. The measured pulse parameters used for the model are $\lambda = 710$ nm and $\tau = 5$ fs. The peak intensity of $I = 17$ TW/cm^2, and the ionization cross-section of $\sigma = 10$ Mb are again estimated by comparison with the experimentally observed spectra. With the help of the higher XUV-absorption cross-section of the first ionization threshold, which results in a higher signal-to-noise ratio, in particular, for the steep increase of the absorbance across the ionization threshold (marked by the letter "a" in figure 6.5 a)), comparisons of the measured and model spectra become more fruitful.

By this comparison, one can see the gating of the dipole moment for photon energies in the absorption continuum, which is marked by the letter "b" in figure 6.5 a). Thus, by using the gating model, one can study the build-up of the ionization threshold similar to what is already done for the single 2s2p doubly-excited absorption line in helium [31]. At the time overlap, however, the measured absorption at the threshold drops less than in the model. This is possibly due to the strong shifting of the absorption lines of the Rydberg series into the ionization continuum, marked

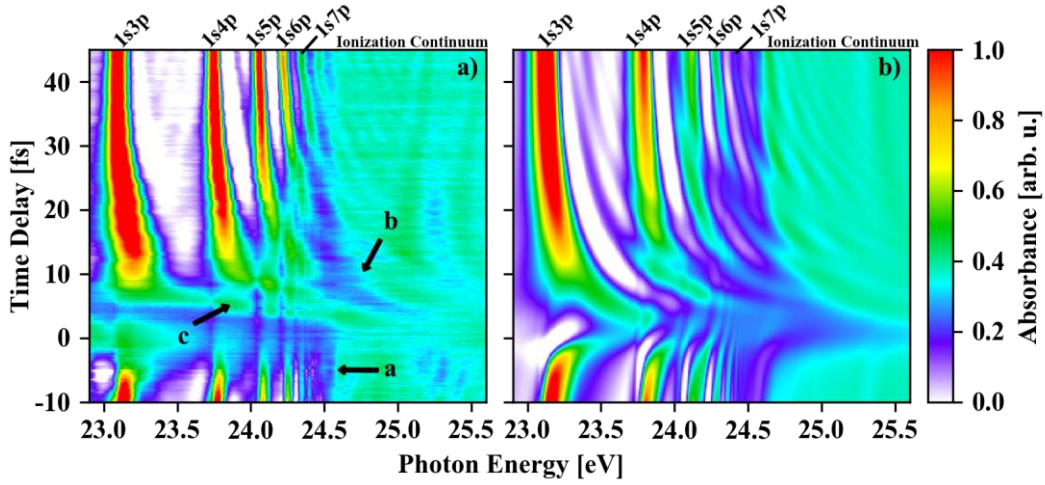

Figure 6.5: The build-up of the first ionization threshold in helium. a) The measured time-dependent absorption spectrum, where the response of the resonant states and the ionization threshold are gated and phase shifted in time by the strong NIR pulse. The "a" marks the almost unperturbed first ionization threshold of helium, "b" the trace of the strong-field gated build-up of the ionization threshold, and "c" marks the time-resolved appearance – emergence – of the Rydberg states from the ionization continuum. b) The simulated transient absorption spectra using the ionization gate model.

by letter c. The lines seem to emerge from the continuum, which is barely reproduced by the model. The assumption of a constant ionization cross-section for all dipole response frequencies might cause this deviation. Since the ionization cross-sections of the real atomic states are different, and since the intense laser does not have a flat spectral profile, the ionization of the target should be energy dependent. Thus, treating the cross-section to be dependent on the photon energy could improve the build-up model, which is, however, beyond the scope of the current thesis.

For better visibility of the absorbance gating at the ionization threshold, figure 6.6 depicts lineouts of the absorbance for different time delays. Subfigure a) shows the suppression of the ionization threshold measured across the time overlap. For negative delays (-15 fs), the threshold manifests in a step-like increase of the absorbance around the photon energy ~24.6 eV. As the ionization gate suppresses the dipole response a few femtoseconds after excitation (5 fs delay), the absorption spectrum becomes flat across the threshold. For later delays, the absorbance becomes

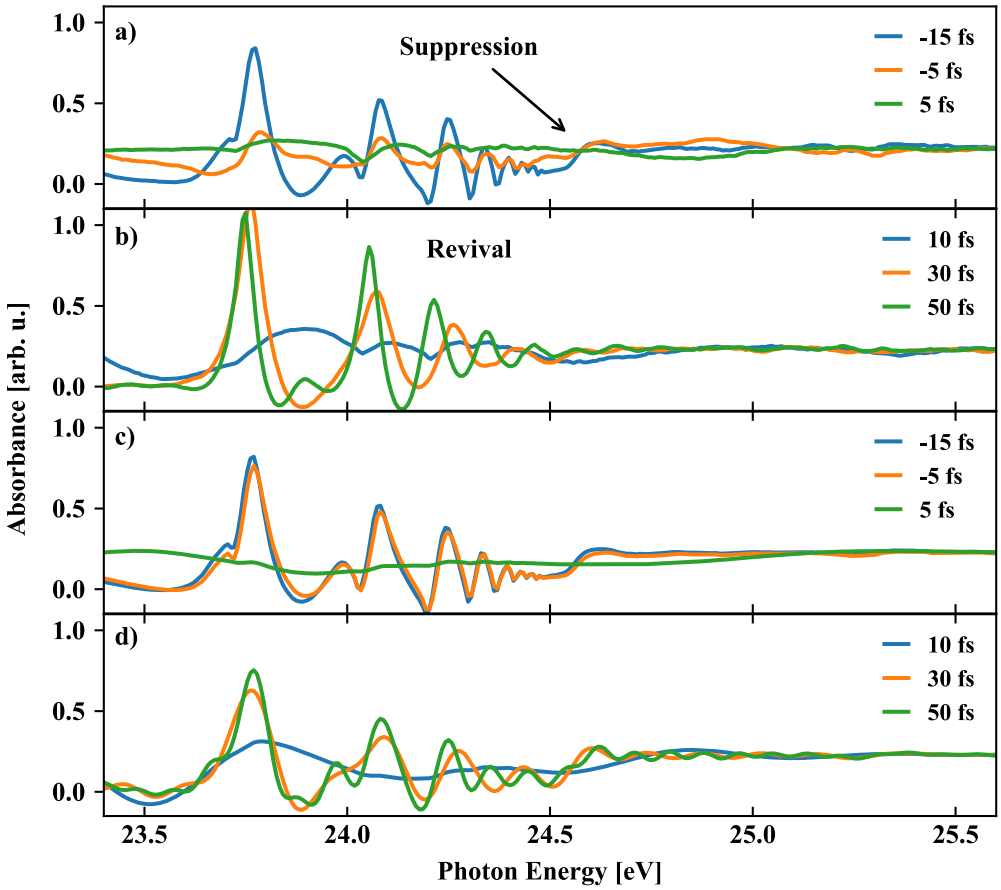

Figure 6.6: Lineouts of the absorbance measuring the build-up of the ionization threshold. a) and b) measured absorbance for different time delays of the NIR. The ionization threshold is suppressed around time overlap from a step-like increase of the absorbance across the threshold to a flat absorption spectrum. For later times the absorption lines and the threshold revive. c) and d) simulated absorbance using the gating model of the time-dependent dipole moment. The suppression and the revival of the absorption lines and the threshold are reproduced.

more modulated by the emergence of the resonance lines that become narrow and shift from high to lower energies, see figure 6.6 b). Subfigures c) and d) present the lineouts of the modeled spectra for the same time delays as in the measurement. The suppression at time overlap and the revival behavior for later delays are reproduced, which validate the picture that the response of the ionization threshold is gated in time by NIR-induced ionization.

Time-dependent Separation of Individual Rydberg Lines

As mentioned in the previous sections, the ionization of the target shortly after XUV-excitation results in the strong broadening of the absorption lines. If these lines are close in energy, they will start to overlap spectrally by the broadening. For later delays, the dipole moment has more time to evolve freely, which leads to separable absorption lines. In order to quantify this time-delay-dependent separation, the following energy-dependent function is used to fit lineouts of the NIR-ionization gated absorption spectra of the doubly excited states of helium for different time delays:

$$A(E) = B(E) + \sum_{j=1}^{n} A_j \frac{\left(q_{\mathrm{org},j}^2 + 1\right)}{\left(q_{\mathrm{mod},j}^2 + 1\right)} \left(\frac{\left(q_{\mathrm{mod},j} + \varepsilon_j\right)^2}{\varepsilon_j^2 + 1} - 1 \right). \qquad (6.6)$$

This function is an incoherent sum of modified Fano-shaped absorption lines. $q_{\mathrm{org},j}$ is the original predetermined asymmetry parameter of the *j*th doubly-excited Fano line, see equation 2.79. The free fit parameters A_j, $q_{\mathrm{mod},j}$, and ε_j are the amplitude, the modified asymmetry parameter, and the reduced energy of the *j*th line, respectively. The reduced energy is given by $\varepsilon_j = (E - E_j)/(\Gamma_j/2)$, where E_j is the energy position and Γ_j is the linewidth of line j. $B(E)$ denotes the energy-dependent non-resonant background given by

$$B(E) = c_0 + \alpha E + \beta E^2 + \gamma E^3 \qquad (6.7)$$

with the fit parameters c_0, α, β, and γ. In the fit, the function 6.6 is convolved by a Gaussian function $G(E)$ with a width of ~ 20 meV to account for the finite experimental spectrometer resolution. The total fit function $S(E)$ then reads:

$$S(E) = A(E) * G(E). \qquad (6.8)$$

Figure 6.7 a) shows the result of the energy position and linewidth versus the time delay of the $sp_{2,3+}$ up to the $sp_{2,6+}$ line in a different color. In the figure, the line position refers to the energy position E_j and the shaded area to the linewidth Γ_j of line j. All four fitted lines show, as expected, a narrowing and a shifting to lower energy for later delays approaching their unperturbed energy positions as they are less influenced by the NIR-induced energy shift. In subfigure 6.7 b), the reference absorption spectrum for negative delays (τ = -12 fs) is shown when the NIR passes

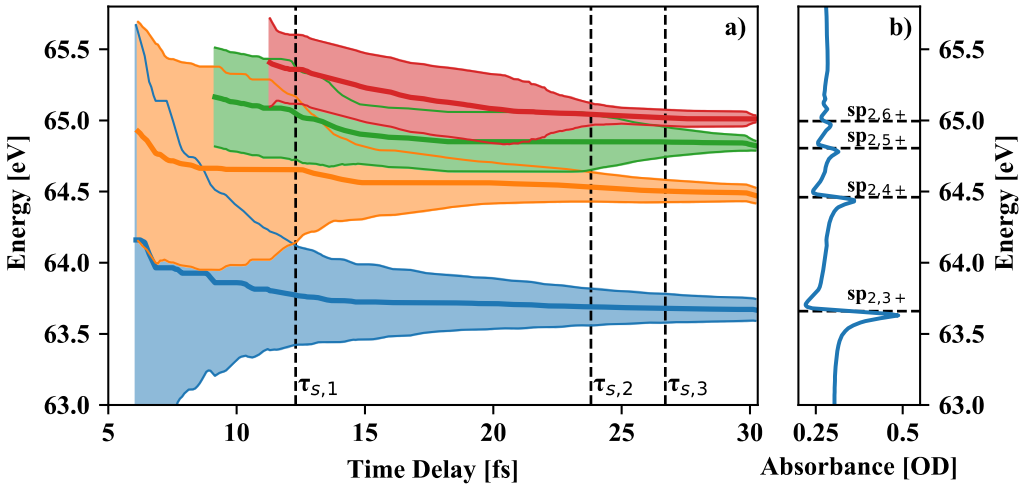

Figure 6.7: Ionization-gated resonance-energy position and linewidth of the $sp_{2,n+}$ Rydberg series in doubly excited helium. a) Results of the fit algorithm. Solid lines indicate the resonance position E_j, and the shaded areas indicate the resonance width Γ_j of state j. The times $\tau_{s,j}$ (vertical dashed lines) mark the delay when spectral lines are separable for the first time from each other during their build-up. b) Reference absorption spectrum measured at $\tau \approx -12.5$ fs.

the target prior to excitation and thus does not have any effect on the absorption lines. The fit routine incorporates a dynamical time-delay-dependent number of lines, i.e., n in equation 6.6 depends on the time-delay. With this, one can determine at which delay the individual absorption lines start to become discernible from the ionization background. In figure 6.7 a), this is indicated by the appearance of the color line for the fit results at a certain time delay. The fit, including lines energetically higher than the $sp_{2,6+}$, does not converge because their signal-to-noise ratio is too low. In the measurement, the signal is mostly limited by the spectrometer resolution of ~1500. Thus, by further enhancing the resolution, one might observe the line separation even for the higher-lying lines above the $sp_{2,6+}$ line.

With the help of the fit, one can observe the time when neighboring line pairs separate. This separation time τ_s can be defined as the time when the energy difference of the line pair is greater than the sum of the respective linewidths, i.e. when the shaded areas in figure 6.7 a) do not overlap anymore. This is indicated by dashed vertical lines in the figure. The fit results in the separation times $\tau_{s,1} = 12.2$ fs for the $sp_{2,3+}$ - $sp_{2,4+}$, $\tau_{s,2} = 23.8$ fs for the $sp_{2,4+}$ - $sp_{2,5+}$, and $\tau_{s,3} = 26.7$ fs for the $sp_{2,5+}$ - $sp_{2,6+}$ line pair. The energetically closer the lines are, the longer must be the delays in order to separate them. This can be intuitively explained as follows. If the lines are closer in energy, the respective dipole moments will need more time to freely evolve in order to generate absorption lines which can be separated.

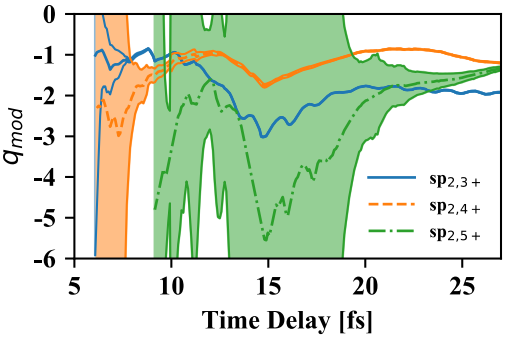

Figure 6.8: Fit results of the modified *q*-parameter of the $sp_{2,n+}$ Rydberg series in doubly excited helium with the shaded area indicating the standard error. The *q*-parameters show a common local minimum around time delay 15 fs, which might be connected to coherent wave-packet dynamics of the Rydberg series.

The fit routine also incorporates the NIR-induced modifications of the line shapes, which are captured by the modified asymmetry parameter $q_{\mathrm{mod,j}}$. This parameter quantifies, as discussed in the fundamentals chapter, the relation of the transition amplitudes for direct ionization and the ionization by configuration interaction of a doubly-excited state. Figure 6.8 presents $q_{\mathrm{mod,j}}$ for different time delays of the $sp_{2,3+}$, $sp_{2,4+}$ and $sp_{2,5+}$ lines. Here, the shaded areas show the fit error for this parameter, which becomes greater for lower delays due to the smaller amplitude of the line. Together with some modifications over the delay, a common minimum of the parameters at about 15 fs appears. This might link to wave-packet dynamics of the coherently excited states, which are imprinted in a common modification of the line shapes. Further investigation using ab initio model simulation could resolve the origin of this joint behavior, which is, however, beyond the scope of this thesis.

The Build-up in the Time Domain and Strong-field Ionization-Gate Characterization

With the dipole reconstruction method, the build-up process can be traced in real-time, and thereby one can capture the dynamics during the NIR strong-field ionization. Furthermore, the reconstruction method provides the possibility to select different energy regions of interest by applying different spectral filters on the absorption spectrum. Figure 6.9 a) presents the dipole amplitude with a window in the spectral region between 62.5 eV and 69.0 eV, i.e., on the wave packet with all Rydberg states starting from the $sp_{2,3+}$. For negative time delays, the beating of the amplitude in real time is visible, reflecting the unperturbed wave-packet dynamics of the coherently excited states. Close to the time overlap, the dipole amplitude decreases fast and recovers for longer delays following the time position of the NIR pulse.

The fast decrease after time overlap is due to the onset of the ionization gate. Thus, this gate is imprinted in the real-time and time-delay-dependent dipole amplitude and thereby can be characterized. For this purpose, the following function is applied to fit the time-dependent dipole amplitude for positive delays starting at 4 fs:

$$R(t) = A_{\mathrm{D}}(t) \cdot \left[\frac{1}{e^{\frac{t-\tau_{\mathrm{G}}}{\Sigma}} + \frac{1}{A_{\mathrm{G}}}} + (1 - A_{\mathrm{G}}) \right]. \qquad (6.9)$$

In this function, a sigmoidal gate within the bracket is multiplied with a reference response $A_{\mathrm{D}}(t)$. Here, τ_{G}, Σ, and A_{G} as above are the gate time position, the gate fall time, and the gate amplitude, respectively. The normalization with a sigmoidal function for $t = 0$ fs is, unlike to equation 6.2, not necessary here since only time positions longer than the expected fall time, $\tau_{\mathrm{G}} > \Sigma$, are considered, and therewith this gate function starts always approximately at unity for $t = 0$ fs. The reference dipole amplitude is obtained by averaging the time-dependent dipole for negative delays between -20 and -12 fs when no ionization gate is present.

The resulting dipole amplitude is shown in the inset of figure 6.9 b) and agrees well with the measured signal. The gate position and the gate fall time is presented in subfigure c). Here the linewidth represents the position error obtained by the standard error of the fitting results of three subsequently measured dipole amplitudes. As expected, the gate time position linearly follows the central position of the strong NIR pulse, and the gate fall time is almost constant. The light blue line is a linear fit of the gate position with a slope one and intercepts the ordinate at -3.4 fs time delay. Thus, the rising edge of the 5.5 fs NIR pulse is sufficiently strong to ionize the target almost completely and therewith gate the dipole response in time. The gate fall time is fitted by a constant function shown in red in subfigure c), which results in a fall time of only $\Sigma = 1.2$ fs. Therewith the ionization gate here is one of the fastest gates ever observed and, in particular, shorter than the pulse duration and the cycle of the light field (~2.5 fs) used for the gate.

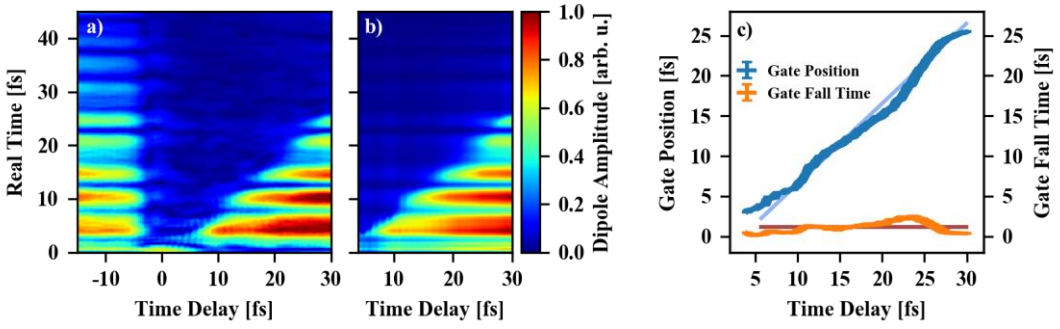

Figure 6.9: Gated time-dependent dipole response in doubly excited helium. a) Amplitude of the time-dependent dipole moment, reconstructed for the Rydberg series of the doubly excited states in helium starting from the $sp_{2,3+}$. b) Best fit on the time-dependent response given by equation 6.9. c) Results of the time-gate position (blue) and gate fall time (orange) from a fit to the reconstructed dipole moments. The line thickness indicates the statistical error over three separate time-delay scans with the same NIR intensity. Straight light blue and dark red lines are a linear and constant-value fit to the experimentally extracted gate position and fall time, respectively.

Although both the gate position and the fall time show the expected trends, a slight deviation of a position linearly following the NIR and constant fall time is observed. This could be linked to wave-packet dynamics of the excited states, which might influence the intra-pulse ionization rate yielding the gate. Further investigations, including comparisons with ab initio model simulations, might resolve the origin of these deviations and clarify possible contributions of wave-packet dynamics.

The reconstruction method can be applied as well on the energy region at the first ionization threshold in helium and thereby trace its build-up in the time domain. Here, one can again use the asymmetric super Gauss filter function $F(\omega)$, which has been introduced above and which is given by equation 5.1. Figure 6.10 shows in a) – c) the absorbance for negative delays in blue with three different filter settings in red, selecting the region of interest. In subfigure a), the filter selects both energy regions, while in b) the absorption lines by the bound Rydberg states and in c) the ionization continuum together with its threshold absorption are filtered. The respective time- and time-delay-dependent dipole amplitudes are presented in figure 6.10 d), e), and f). For the filter, which includes the absorption spectrum below and above the ionization threshold, the wave-packet beating is observed for negative delays, see subfigure d). This is similar to the observation for the doubly excited region in figure 6.9 a). Furthermore, the strong suppression of the dipole amplitude close to time overlap and the recovering of the dipole following the NIR pulse are reproduced. If now only the bound absorption lines are filtered, similar behavior of the dipole amplitude is observed, subfigure e). Thus, most of the signal in d), in particular for longer real times, is due to the wave packet of the coherently excited Rydberg states. If selecting only the energy region of the ionization continuum, the amplitude decreases very rapidly in real time due to the broad absorption spectrum of the continuum, subfigure f). However, a faint signal remains, which depends on the timing of the NIR pulse.

In this time-domain view, a clear indication appears that the continuum absorption is actually gated by the NIR-induced ionization. Shortly after pulse overlap, i.e., around 3 fs time delay, a drop of the dipole amplitude is observed. If the strong NIR would only contribute with a ponderomotive shift leading to an effective phase shift of the dipole moment, this drop would not be present. This is shown by the inset in subfigure f), where the phase shift model on the continuum response, as described above, is used without amplitude gating. As a result, the fall time of the strong-field-induced ionization gate is indeed fast enough to gate the ultrafast response of the ionization threshold. Since a presence of a continuum threshold is not limited to an atomic target, but rather it is a general property of different materials like molecules or, in particular, solid-state system, the here presented study of using an ultrafast

ionization gate allows many investigations on the build-up processes of responses in general.

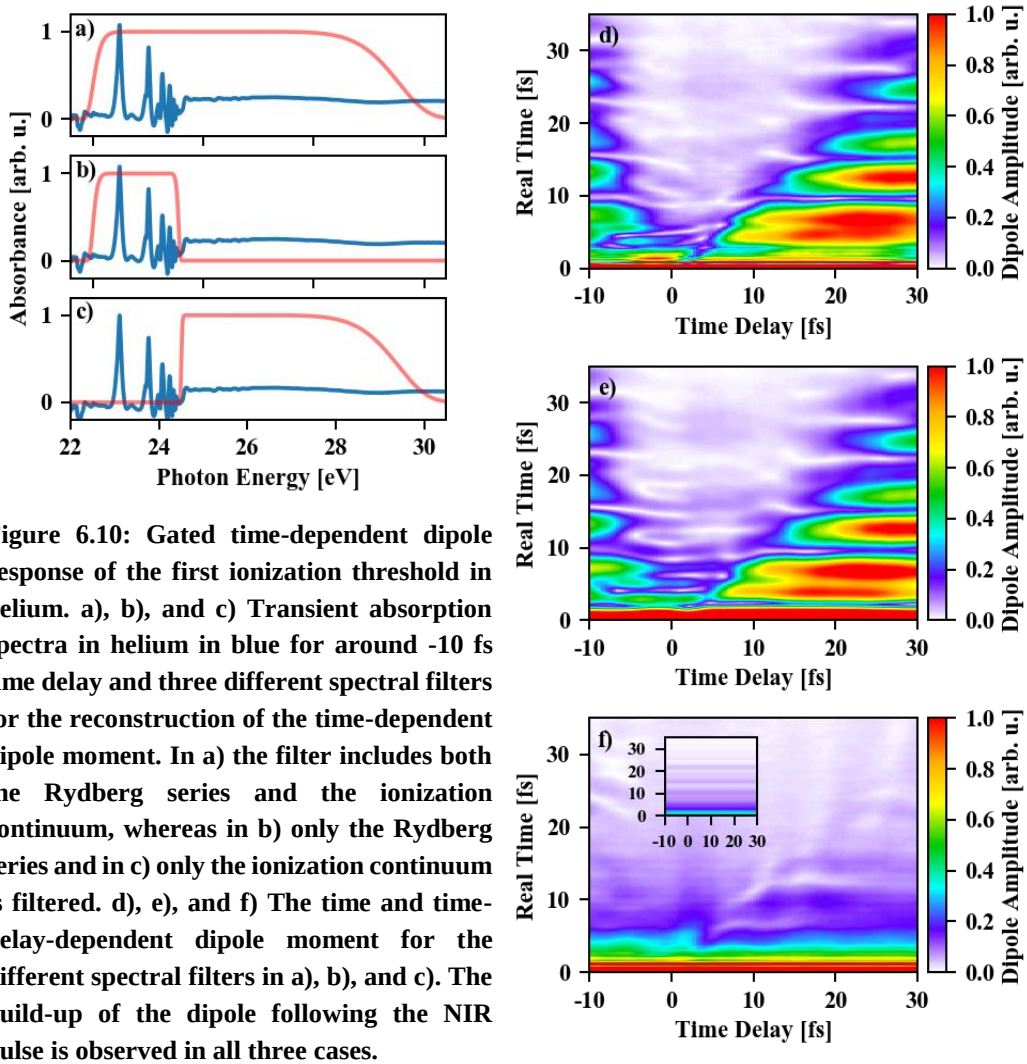

Figure 6.10: Gated time-dependent dipole response of the first ionization threshold in helium. a), b), and c) Transient absorption spectra in helium in blue for around -10 fs time delay and three different spectral filters for the reconstruction of the time-dependent dipole moment. In a) the filter includes both the Rydberg series and the ionization continuum, whereas in b) only the Rydberg series and in c) only the ionization continuum is filtered. d), e), and f) The time and time-delay-dependent dipole moment for the different spectral filters in a), b), and c). The build-up of the dipole following the NIR pulse is observed in all three cases.

7. Summary and Conclusion

The general subject of this thesis is the investigation of the quantum-mechanical dynamics of electrons excited in helium to states in the vicinity of the ionization threshold. The electrons are coherently excited by using an attosecond pulse in the extreme ultraviolet (XUV) spectral range, which generates an XUV dipole response driven by the dipole moment between the excited (continuum) states and the ground state of helium. The response interferes with the XUV excitation pulse, and the interference is measured by means of attosecond transient absorption spectroscopy across the ionization threshold. In this interferometric method, the dipole response is further manipulated by an ultrashort and strong near-infrared (NIR) laser pulse, and its changes are resolved in time by recording XUV transient absorption spectra for different time delays between the NIR interaction and the XUV excitation. Since the XUV dipole response is dominated by the overlap integral between the excited states and the ground-state wave functions, the investigated response above the ionization threshold is a measure of the dynamics of free electrons in close proximity of the parent ion. Thus, the laser-field-modified dipole response at an ionization threshold provides access to laser-driven electron dynamics in the vicinity of the Coulomb field singularity of an ion.

The transient absorption spectra are recorded by an attosecond beamline with high temporal (~ 85 as) and spectral ($E/\Delta E$ ~ 1500) resolution. In the course of the dissertation, the experimental setup has been upgraded by several components. A doubly differentially pumped hollow-core fiber was designed and implemented. It allows one to spectrally broaden the NIR laser pulse in order to shorten its pulse duration down to ~ 4 fs and simultaneously achieve high output pulse energies (~ 1.5 mJ) from the fiber. For reliable experimental laser conditions, an optical setup to measure and stabilize the carrier-envelope phase (CEP) of the ultrashort NIR pulse in front of the attosecond beamline has been installed, which provides access to control the CEP within a standard deviation of ~ 330 mrad. Furthermore, the attosecond beamline was extended by a variable filter setup to separate in time and space the XUV and NIR pulse, by an NIR spectrometer to measure *in situ* the blue shift of the NIR spectrum in the high harmonic generation process, and by an external beam path interferometer to access the field polarization of the NIR in a transient absorption experiment.

In the measured time-delay-dependent absorption spectra of helium presented here, several laser-induced spectro-temporal structures are observed both below and above the ionization threshold. The observations were facilitated by the development of a procedure for recording the XUV reference spectrum *in situ*. It allows to resolve

weak structures in the target's absorbance with a sensitivity of a few thousandths of an optical density unit. By comparing the measured transient absorption spectra with the results of different quantum-mechanical model simulations, it was possible to identify the underlying processes of light-matter interaction leading to the observed structures in the absorption.

First, a multi-level model simulation was conducted, which treats the bound and continuum states of the helium atom by discretized levels. Within this model, one can selectively switch on and off the continuum or the coupling between the continuum and the bound states. This flexibility helps to isolate the contributions of the ionization continuum to the observed transient absorption structures. It was found that the laser-driven response of the ionization threshold shows a similar—not a priori clear—time-resolved behavior as resonances of bound-bound transitions. The response spectrally imprints a hyperbolic-like structure above the ionization threshold, which can be linked to the NIR-induced energy shift of the photoelectron's kinetic energy in the vicinity of the atomic core.

Due to the interferometric principle of transient absorption spectroscopy, the measurement is sensitive to the amplitude and phase of the atomic dipole response. Thus, it can be reconstructed in real-time directly from the XUV absorption spectra by means of Fourier transformation. The real-time–time-delay analysis of the dipole response shows a revival of its amplitude following the timing position of the NIR pulse, which can be interpreted as an NIR-driven electron recollision into the parent ion after its XUV-ionization. Signatures of this revival have been reproduced by simulating the dipole response by a laser-driven electron wave packet model, which is defined on a numerical one-dimensional spatial grid. Here, the wave packet is subjected to a singly excited atomic core, and it shows an NIR-driven wiggling around the core in correlation with the increase of the dipole amplitude. In addition, these findings are supported by calculations of classical electron trajectories in an oscillating laser field, where it was found that the dynamics of the wave function's center of gravity can be described well. Furthermore, first measurements to probe the signature of electron recollisions in the dipole response are presented using linear and circular field polarization of the NIR pulse.

Regarding the presented transient absorption spectra with high NIR intensities, the observed structures at the ionization threshold in helium are not well described exclusively by an energy shift of the continuum states anymore. Here, the strong-field-ionization of the helium atoms leads to a non-negligible time-delay-dependent decrease of the dipole response. This process can be modeled by gating the dipole response in the time domain and calculating the resulting absorption spectra using Fourier transformation. In the course of this work, a strong-field-ionization gating model is introduced, which includes both the time-dependent decrease of the dipole response amplitude and the laser-induced phase shift beyond the impulsive limit, where amplitude gate and phase shift instantaneously act on the response. With this,

the build-up dynamics of complex spectral signatures can be understood, which consists of multiple asymmetric Fano resonances of the doubly excited Rydberg series close to the $N = 2$ ionization threshold in helium. As a result, the time-dependent separation of the partly overlapping Fano resonances and their laser-modified line-shape-asymmetry have been extracted quantitatively. In addition, the time-domain observation of the dipole response revealed the ionization gate position and the gating fall time to be as short as ~1.2 fs. Furthermore, this strong-field-ionization technique was applied to the first ionization threshold of helium, where its build-up in the time domain has been observed for the first time.

To conclude, attosecond transient absorption spectroscopy is a powerful tool to study light-matter interaction and laser-induced dynamics not only between bound states, but it can be extended to a continuum of states near an ionization threshold. Here, one is sensitive to the amplitude and the phase of the dipole response generated from coherently excited states, energetically lying in the transition region between the neutral and the ionized atom. Additionally, this dipole response can be controlled by using strong-field-ionization gating and laser-induced phase shifts via ponderomotive energy shifts of the continuum states, while its evolution is traced in time.

Resolving laser-induced energy shifts of slow photoelectrons in the vicinity of the parent ion might lead to a better understanding of the effects caused by the Coulomb potential during the ionization process. One could imagine that the magnitude of the laser-induced phase shift on the dipole response depends on the kinetic energy of the ionized electron, i.e., the excitation photon energy above the threshold. Slow electrons may stay longer in close proximity to the ionic core and are thereby are stronger influenced by the Coulomb potential, while faster electrons leave the ion earlier, and the observed phase shift could be purely described by the ponderomotive energy shift. The presented field-driven dynamics were already observed at moderate laser intensities. Thus, the here introduced phase-sensitive measurement procedure near an ionization threshold might be helpful for condensed phase targets, where damage thresholds typically set an upper limit to the allowed laser intensity [162].

The signature of the electron recollision into the ionic core can be further validated by model simulations, which solve the time-dependent Schrödinger equation of the helium atom on a two- or three-dimensional spatial grid. With this, one can directly compare the dipole response for circularly and linearly polarized NIR fields and thereby identify the evolution of the response that is caused by the recollision. Further insight might be gained by solving the trajectory of a spatial electron wave packet forced by the oscillatory NIR field beyond the strong-field approximation, i.e., in the presence of the Coulomb potential. This would directly consider the dispersion and the spreading of the wave packet resulting in a decrease of the dipole response and identify the influence of the Coulomb potential.

As mentioned in the introduction of this thesis, one ultimate goal in the field of time-resolved spectroscopy is to temporally and spatially resolve or even control the trajectories of electrons and nuclei during chemical reactions. Regarding this goal, the presented work shows a way to investigate the dynamics of liberated electrons in the vicinity of a parent ion within strong and ultrashort fields. They are probed by the induced dipole response at the ionization threshold in helium. Since owing an ionization threshold is a general property of media, this method can be extended to the molecular case. In particular, here, the response can even be site-selective within a molecule using time-resolved spectroscopy of transitions from deeply bound states of an atom in the molecule to a continuum of states closely above the ionization threshold.

8. Appendix

Atomic Units

The system of atomic units (a. u.) is often used in the field of atomic and molecular physics. It scales the physical dimensions by physical properties of the hydrogen atom such that it minimizes the quantities in many equations. Here the conventions are that the elementary charge, the electron mass, the reduced Planck constant, and the Coulomb's constant are unity

$$e = m_e = \hbar = \frac{1}{4\pi\varepsilon_0} = 1. \qquad (8.1)$$

The most famous unit system is the International System of Units (SI units), which is also used in this thesis. Table 1 presents some selected conversion factors from the atomic units system to the SI units taken from [46].

Dimension	**Value in SI units**
Electric charge	1.602×10^{-19} C
Electric dipole moment	8.478×10^{-30} C m
Mass	9.109×10^{-31} kg
Length	5.292×10^{-11} m
Momentum	1.993×10^{-24} kg m s^{-1}
Action	1.055×10^{-34} J s
Time	2.419×10^{-17} s
Energy	4.360×10^{-18} J = 27.211 eV
Electric Field	5.142×10^{11} V m^{-1}
Field Intensity	3.509×10^{16} W cm^{-2}

Table 1: Conversion factors from the atomic units system into the International System of Units (SI units) for up to the third decimal place. Taken from [46].

Singly Excited Bound States of Helium

The tabulated dipole moments are calculated using equation 5.10 from the oscillator strengths taken from the reference [63]. These values are used in the multi-level model simulation described in the main text.

	$1s^2$	1s2s	1s3s	1s4s
1s2p	0.729	5.057	1.870	0.656
1s3p	0.360	1.580	12.382	4.628
1s4p	0.227	0.801	2.671	22.714
1s5p	0.160	0.515	1.352	4.003
1s6p	0.121	0.371	0.874	2.001
1s7p	0.095	0.286	0.6333	1.287

Table 2: The dipole moments between the s and p states of the singly excited bound states of helium. The dipole moments are given in atomic units.

	1s2p	1s3p	1s4p	1s5p
1s3d	3.954	8.218	0.966	0.361
1s4d	1.397	6.389	16.648	2.272
1s5d	0.791	2.457	9.379	28.162
1s6d	0.535	1.431	3.656	12.962
1s7d	0.396	0.982	2.139	5.023
1s8d	0.311	0.736	1.473	2.934

Table 3: The dipole moments between the p and d states of the singly excited bound states of helium. The dipole moments are given in atomic units.

9. Bibliography

[1] Birk P, Stooß V, Hartmann M, Borisova G D, Blättermann A, Heldt T, Bartschat K, Ott C and Pfeifer T 2020 Attosecond transient absorption of a continuum threshold *J. Phys. B At. Mol. Opt. Phys.* **53** 124002

[2] Stooß V, Birk P, Blättermann A, Hartmann M, Borisova G D, Ott C and Pfeifer T 2020 Strong-field-gated buildup of a Rydberg series *Phys. Rev. Res.* **2** 032041

[3] Leone S R, McCurdy C W, Burgdörfer J, Cederbaum L S, Chang Z, Dudovich N, Feist J, Greene C H, Ivanov M, Kienberger R, Keller U, Kling M F, Loh Z-H, Pfeifer T, Pfeiffer A N, Santra R, Schafer K, Stolow A, Thumm U and Vrakking M J J 2014 What will it take to observe processes in "real time"? *Nat. Photonics* **8** 162–6

[4] Lépine F, Ivanov M Y and Vrakking M J J 2014 Attosecond molecular dynamics: fact or fiction? *Nat. Photonics* **8** 195–204

[5] Altshuler D L, Welch K C, Cho B H, Welch D B, Lin A F, Dickson W B and Dickinson M H 2010 Neuromuscular control of wingbeat kinematics in Anna's hummingbirds (Calypte anna) *J. Exp. Biol.* **213** 2507–14

[6] Humes L E, Busey T A, Craig J C and Kewley-Port D 2009 The effects of age on sensory thresholds and temporal gap detection in hearing, vision, and touch *Attention, Perception, Psychophys.* **71** 860–71

[7] Aghanim N, Akrami Y, Ashdown M, Aumont J, Baccigalupi C, Ballardini M, Banday A J, Barreiro R B, Bartolo N, Basak S, Battye R, Benabed K, Bernard J-P, Bersanelli M, Bielewicz P, Bock J J, Bond J R, Borrill J, Bouchet F R, Boulanger F, Bucher M, Burigana C, Butler R C, Calabrese E, Cardoso J-F, Carron J, Challinor A, Chiang H C, Chluba J, Colombo L P L, Combet C, Contreras D, Crill B P, Cuttaia F, de Bernardis P, de Zotti G, Delabrouille J, Delouis J-M, Di Valentino E, Diego J M, Doré O, Douspis M, Ducout A, Dupac X, Dusini S, Efstathiou G, Elsner F, Enßlin T A, Eriksen H K, Fantaye Y, Farhang M, Fergusson J, Fernandez-Cobos R, Finelli F, Forastieri F, Frailis M, Fraisse A A, Franceschi E, Frolov A, Galeotta S, Galli S, Ganga K, Génova-Santos R T, Gerbino M, Ghosh T, González-Nuevo J, Górski K M, Gratton S, Gruppuso A, Gudmundsson J E, Hamann J, Handley W, Hansen F K, Herranz D, Hildebrandt S R, Hivon E, Huang Z, Jaffe A H, Jones W C, Karakci A, Keihänen E, Keskitalo R, Kiiveri K, Kim J, Kisner T S, Knox L, Krachmalnicoff N, Kunz M, Kurki-Suonio H, Lagache G, Lamarre J-M, Lasenby A, Lattanzi M, Lawrence C R, Le Jeune M, Lemos P, Lesgourgues J, Levrier F, et al 2020 Planck 2018 results *Astron. Astrophys.* **641** A6

[8] Abbott B P, Abbott R, Abbott T D, Abernathy M R, Acernese F, Ackley K, Adams C, Adams T, Addesso P, Adhikari R X, Adya V B, Affeldt C, Agathos M, Agatsuma K, Aggarwal N, Aguiar O D, Aiello L, Ain A, Ajith P, Allen B, Allocca A, Altin P A, Anderson S B, Anderson W G, Arai K, Arain M A, Araya M C, Arceneaux C C, Areeda J S, Arnaud N, Arun K G, Ascenzi S,

Ashton G, Ast M, Aston S M, Astone P, Aufmuth P, Aulbert C, Babak S, Bacon P, Bader M K M, Baker P T, Baldaccini F, Ballardin G, Ballmer S W, Barayoga J C, Barclay S E, Barish B C, Barker D, Barone F, Barr B, Barsotti L, Barsuglia M, Barta D, Bartlett J, Barton M A, Bartos I, Bassiri R, Basti A, Batch J C, Baune C, Bavigadda V, Bazzan M, Behnke B, Bejger M, Belczynski C, Bell A S, Bell C J, Berger B K, Bergman J, Bergmann G, Berry C P L, Bersanetti D, Bertolini A, Betzwieser J, Bhagwat S, Bhandare R, Bilenko I A, Billingsley G, Birch J, Birney R, Birnholtz O, Biscans S, Bisht A, Bitossi M, Biwer C, Bizouard M A, Blackburn J K, Blair C D, Blair D G, Blair R M, Bloemen S, Bock O, Bodiya T P, Boer M, Bogaert G, Bogan C, Bohe A, et al 2016 Observation of Gravitational Waves from a Binary Black Hole Merger *Phys. Rev. Lett.* **116** 061102

[9] Zewail A H 2000 Femtochemistry: Atomic-Scale Dynamics of the Chemical Bond *J. Phys. Chem. A* **104** 5660–94

[10] DeMaria A J, Stetser D A and Heynau H 1966 Self Mode-Locking of Lasers with Saturable Absorbers *Appl. Phys. Lett.* **8** 174–6

[11] Dahlström L 1972 Passive mode-locking and Q-switching of high power lasers by means of the optical Kerr effect *Opt. Commun.* **5** 157–62

[12] Brabec T and Krausz F 2000 Intense few-cycle laser fields: Frontiers of nonlinear optics *Rev. Mod. Phys.* **72** 545–91

[13] Baltuška A, Udem T, Uiberacker M, Hentschel M, Goulielmakis E, Gohle C, Holzwarth R, Yakovlev V S, Scrinzi A, Hänsch T W and Krausz F 2003 Attosecond control of electronic processes by intense light fields *Nature* **421** 611–5

[14] Wirth A, Hassan M T, Grguras I, Gagnon J, Moulet A, Luu T T, Pabst S, Santra R, Alahmed Z A, Azzeer A M, Yakovlev V S, Pervak V, Krausz F and Goulielmakis E 2011 Synthesized light transients. *Science* **334** 195–200

[15] Goulielmakis E, Schultze M, Hofstetter M, Yakovlev V S, Gagnon J, Uiberacker M, Aquila A L, Gullikson E M, Attwood D T, Kienberger R, Krausz F and Kleineberg U 2008 Single-cycle nonlinear optics. *Science* **320** 1614–7

[16] McPherson A, Gibson G, Jara H, Johann U, Luk T S, McIntyre I A, Boyer K and Rhodes C K 1987 Studies of multiphoton production of vacuum-ultraviolet radiation in the rare gases *J. Opt. Soc. Am. B* **4** 595

[17] L'Huillier A and Balcou P 1993 High-order harmonic generation in rare gases with a 1-ps 1053-nm laser *Phys. Rev. Lett.* **70** 774–7

[18] Paul P M, Toma E S, Breger P, Mullot G, Auge F, Balcou P, Muller H G and Agostini P 2001 Observation of a train of attosecond pulses from high harmonic generation. *Science* **292** 1689–92

[19] Hentschel M, Kienberger R, Spielmann C, Reider G a, Milosevic N, Brabec T, Corkum P, Heinzmann U, Drescher M and Krausz F 2001 Attosecond metrology *Nature* **414** 509–13

[20] Gaumnitz T, Jain A, Pertot Y, Huppert M, Jordan I, Ardana-Lamas F and Wörner H J 2017 Streaking of 43-attosecond soft-X-ray pulses generated by a passively CEP-stable mid-infrared driver *Opt. Express* **25** 27506

[21] Drescher M, Hentschel M, Kienberger R, Uiberacker M, Yakovlev V, Scrinzi A, Westerwalbesloh T, Kleineberg U, Heinzmann U and Krausz F 2002 Time-resolved atomic inner-shell spectroscopy *Nature* **419** 803–7

[22] Uiberacker M, Uphues T, Schultze M, Verhoef A J, Yakovlev V, Kling M F, Rauschenberger J, Kabachnik N M, Schröder H, Lezius M, Kompa K L, Muller H-G, Vrakking M J J, Hendel S, Kleineberg U, Heinzmann U, Drescher M and Krausz F 2007 Attosecond real-time observation of electron tunnelling in atoms *Nature* **446** 627–32

[23] Goulielmakis E, Loh Z-H, Wirth A, Santra R, Rohringer N, Yakovlev V S, Zherebtsov S, Pfeifer T, Azzeer A M, Kling M F, Leone S R and Krausz F 2010 Real-time observation of valence electron motion *Nature* **466** 739–43

[24] Wang H, Chini M, Chen S, Zhang C-H, He F, Cheng Y, Wu Y, Thumm U and Chang Z 2010 Attosecond Time-Resolved Autoionization of Argon *Phys. Rev. Lett.* **105** 143002

[25] Reduzzi M, Feng C, Chu W-C, Dubrouil A, Calegari F, Nisoli M, Frassetto F, Poletto L, Lin C-D and Sansone G 2013 Attosecond Absorption Spectroscopy in Molecules *CLEO: 2013* (OSA) p QF2C.1

[26] Warrick E R, Cao W, Neumark D M and Leone S R 2016 Probing the Dynamics of Rydberg and Valence States of Molecular Nitrogen with Attosecond Transient Absorption Spectroscopy *J. Phys. Chem. A* **120** 3165–74

[27] Birk P 2016 *Time-dependent Strong-Field Effects in Atoms and Molecules observed by Attosecond Transient Absorption Spectroscopy* (Master Thesis Heidelberg University)

[28] Cavalieri A L, Müller N, Uphues T, Yakovlev V S, Baltuška A, Horvath B, Schmidt B, Blümel L, Holzwarth R, Hendel S, Drescher M, Kleineberg U, Echenique P M, Kienberger R, Krausz F and Heinzmann U 2007 Attosecond spectroscopy in condensed matter *Nature* **449** 1029–32

[29] Fraunhofer J 1817 Bestimmung des Brechungs- und des Farbenzerstreungs-Vermögens verschiedener Glasarten, in Bezug auf die Vervollkommnung achromatischer Fernröhre *Ann. Phys.* **56** 264–313

[30] Kirchhoff G and Bunsen R 1861 Chemische Analyse durch Spectralbeobachtungen *Ann. der Phys. und Chemie* **189** 337–81

[31] Kaldun A, Blättermann A, Stooß V, Donsa S, Wei H, Pazourek R, Nagele S, Ott C, Lin C D, Burgdörfer J and Pfeifer T 2016 Observing the ultrafast buildup of a Fano resonance in the time domain. *Science* **354** 738–41

[32] Chu W-C and Lin C D 2013 Absorption and emission of single attosecond light pulses in an autoionizing gaseous medium dressed by a time-delayed control field *Phys. Rev. A* **87** 013415

[33] Blättermann A, Ott C, Kaldun A, Ding T and Pfeifer T 2014 Two-dimensional spectral interpretation of time-dependent absorption near laser-coupled resonances *J. Phys. B At. Mol. Opt. Phys.* **47** 124008

[34] Kaldun A, Ott C, Blättermann A, Laux M, Meyer K, Ding T, Fischer A and Pfeifer T 2014 Extracting Phase and Amplitude Modifications of Laser-

Coupled Fano Resonances *Phys. Rev. Lett.* **112** 103001

[35] Ott C, Kaldun A, Raith P, Meyer K, Laux M, Evers J, Keitel C H, Greene C H and Pfeifer T 2013 Lorentz meets Fano in spectral line shapes: a universal phase and its laser control. *Science* **340** 716–20

[36] Heeg K P, Kaldun A, Strohm C, Reiser P, Ott C, Subramanian R, Lentrodt D, Haber J, Wille H-C, Goerttler S, Rüffer R, Keitel C H, Röhlsberger R, Pfeifer T and Evers J 2017 Spectral narrowing of x-ray pulses for precision spectroscopy with nuclear resonances. *Science* **357** 375–8

[37] Diels J-C and Rudolph W 2006 *Ultrashort Laser Pulse Phenomena* (Academic Press)

[38] Saleh B E A and Teich M C 2007 *Fundamentals of Photonics* (John Wiley & Sons, Inc.)

[39] Krausz F and Ivanov M 2009 Attosecond physics *Rev. Mod. Phys.* **81** 163–234

[40] Chang Z 2011 *Fundamentals of Attosecond Optics* (CRC Press)

[41] Leone S R and Neumark D M 2016 Attosecond science in atomic, molecular, and condensed matter physics *Faraday Discuss.* **194** 15–39

[42] Keldysh L V. 1965 Ionization in the field of a strong electromagnetic wave *Sov. Phys. Jetp* **20** 1307–14

[43] Dirac P A M 1981 *The Principles of Quantum Mechanics* (Clarendon Press)

[44] Jun John Sakurai 1993 *Modern Quantum Mechanics* (Prentice Hall)

[45] Fließbach T 2018 *Quantenmechanik* (Springer)

[46] B. H. Bransden and C. J. Joachain 2007 *Physics of atoms and molecules* (Prentice Hall)

[47] Hertel I V and Schulz C 2008 *Atome, Moleküle und optische Physik 1* (Srpinger)

[48] Rabi I I 1937 Space quantization in a gyrating magnetic field *Phys. Rev.* **51** 652–4

[49] Autler S H and Townes C H 1955 Stark Effect in Rapidly Varying Fields *Phys. Rev.* **100** 703–22

[50] Stooß V, Cavaletto S M, Donsa S, Blättermann A, Birk P, Keitel C H, Březinová I, Burgdörfer J, Ott C and Pfeifer T 2018 Real-Time Reconstruction of the Strong-Field-Driven Dipole Response *Phys. Rev. Lett.* **121** 173005

[51] Stooß V 2018 *Strong-Field Spectroscopy: From Absorption to Time-Resolved Dynamics in Strong Fields* (PhD Thesis Heidelberg University)

[52] R. de L. Kronig 1926 On the theory of the dispersion of X-rays *J. Opt. Soc. Am.* **12** 547–557

[53] H. A. Kramers 1927 La diffusion de la lumière par les atomes *Atti del Congr. Int. dei Fis.* **2** 545–57

[54] Gaarde M B, Buth C, Tate J L and Schafer K J 2011 Transient absorption and reshaping of ultrafast XUV light by laser-dressed helium *Phys. Rev. A* **83**

013419

[55] Chen S, Bell M J, Beck A R, Mashiko H, Wu M, Pfeiffer A N, Gaarde M B, Neumark D M, Leone S R and Schafer K J 2012 Light-induced states in attosecond transient absorption spectra of laser-dressed helium *Phys. Rev. A* **86** 063408

[56] Chini M, Zhao B, Wang H, Cheng Y, Hu S X and Chang Z 2012 Subcycle ac Stark Shift of Helium Excited States Probed with Isolated Attosecond Pulses *Phys. Rev. Lett.* **109** 073601

[57] Ott C, Kaldun A, Argenti L, Raith P, Meyer K, Laux M, Zhang Y, Blättermann A, Hagstotz S, Ding T, Heck R, Madroñero J, Martín F and Pfeifer T 2014 Reconstruction and control of a time-dependent two-electron wave packet *Nature* **516** 374–8

[58] Argenti L, Jiménez-Galán Á, Marante C, Ott C, Pfeifer T and Martín F 2015 Dressing effects in the attosecond transient absorption spectra of doubly excited states in helium *Phys. Rev. A* **91** 061403

[59] Madden R P and Codling K 1963 New Autoionizing Atomic Energy Levels in He, Ne, and Ar *Phys. Rev. Lett.* **10** 516–8

[60] Schulz K, Kaindl G, Domke M, Bozek J D, Heimann P A, Schlachter A S and Rost J M 1996 Observation of New Rydberg Series and Resonances in Doubly Excited Helium at Ultrahigh Resolution *Phys. Rev. Lett.* **77** 3086–9

[61] Domke M, Schulz K, Remmers G, Kaindl G and Wintgen D 1996 High-resolution study of 1Po double-excitation states in helium. *Phys. Rev. A* **53** 1424–38

[62] Morton D C, Wu Q and Drake G W 2006 Energy levels for the stable isotopes of atomic helium(4 He I and 3 He I) *Can. J. Phys.* **84** 83–105

[63] Drake G 2006 High Precision Calculations for Helium *Springer Handbook of Atomic, Molecular, and Optical Physics* (Springer) pp 199–219

[64] Pauli W 1925 Über den Zusammenhang des Abschlusses der Elektronengruppen im Atom mit der Komplexstruktur der Spektren *Zeitschrift für Phys.* **31** 765–83

[65] Beutler H 1935 Über Absorptionsserien von Argon, Krypton und Xenon zu Termen zwischen den beiden Ionisierungsgrenzen *Zeitschrift für Phys.* **93** 177–96

[66] Fano U 1961 Effects of Configuration Interaction on Intensities and Phase Shifts *Phys. Rev.* **124** 1866–78

[67] Agostini P and DiMauro L F 2004 The physics of attosecond light pulses *Reports Prog. Phys.* **67** 1563–1563

[68] Popmintchev T, Chen M-C, Popmintchev D, Arpin P, Brown S, Alisauskas S, Andriukaitis G, Balciunas T, Mücke O D, Pugzlys A, Baltuska A, Shim B, Schrauth S E, Gaeta A, Hernández-García C, Plaja L, Becker A, Jaron-Becker A, Murnane M M and Kapteyn H C 2012 Bright coherent ultrahigh harmonics in the keV x-ray regime from mid-infrared femtosecond lasers. *Science* **336** 1287–91

[69] Lewenstein M, Balcou P, Ivanov M Y, L'Huillier A and Corkum P B 1994

Theory of high-harmonic generation by low-frequency laser fields *Phys. Rev. A* **49** 2117–32

[70] Corkum P B 1993 Plasma perspective on strong field multiphoton ionization *Phys. Rev. Lett.* **71** 1994–7

[71] P. Jaegle 2006 *Coherent Sources of XUV Radiation* (Springer)

[72] Salières P, L'Huillier A and Lewenstein M 1995 Coherence Control of High-Order Harmonics *Phys. Rev. Lett.* **74** 3776–9

[73] Sansone G, Benedetti E, Calegari F, Vozzi C, Avaldi L, Flammini R, Poletto L, Villoresi P, Altucci C, Velotta R, Stagira S, De Silvestri S and Nisoli M 2006 Isolated single-cycle attosecond pulses. *Science* **314** 443–6

[74] Feng X, Gilbertson S, Mashiko H, Wang H, Khan S D, Chini M, Wu Y, Zhao K and Chang Z 2009 Generation of isolated attosecond pulses with 20 to 28 femtosecond lasers *Phys. Rev. Lett.* **103** 28–31

[75] Abel M J, Pfeifer T, Nagel P M, Boutu W, Bell M J, Steiner C P, Neumark D M and Leone S R 2009 Isolated attosecond pulses from ionization gating of high-harmonic emission *Chem. Phys.* **366** 9–14

[76] Ferrari F, Calegari F, Lucchini M, Vozzi C, Stagira S, Sansone G and Nisoli M 2010 High-energy isolated attosecond pulses generated by above-saturation few-cycle fields *Nat. Photonics* **4** 875–9

[77] Vincenti H and Quéré F 2012 Attosecond Lighthouses: How To Use Spatiotemporally Coupled Light Fields To Generate Isolated Attosecond Pulses *Phys. Rev. Lett.* **108** 113904

[78] DiMauro L F, Sistrunk E, DiChiara A D, Reis D A, Ghimire S and Agostini P 2010 Observation of high-order harmonic generation in a bulk crystal *Nat. Phys.* **7** 138–41

[79] Kurz H G, Steingrube D S, Ristau D, Lein M, Morgner U and Kovačev M 2013 High-order-harmonic generation from dense water microdroplets *Phys. Rev. A* **87** 063811

[80] Luu T T, Yin Z, Jain A, Gaumnitz T, Pertot Y, Ma J and Wörner H J 2018 Extreme–ultraviolet high–harmonic generation in liquids *Nat. Commun.* **9** 3723

[81] Shiner A D, Trallero-Herrero C, Kajumba N, Bandulet H-C, Comtois D, Légaré F, Giguère M, Kieffer J-C, Corkum P B and Villeneuve D M 2009 Wavelength Scaling of High Harmonic Generation Efficiency *Phys. Rev. Lett.* **103** 073902

[82] Ott C 2012 *Attosecond multidimensional interferometry of single and two correlated electrons in atoms* (PhD Thesis Heidelberg University)

[83] Kaldun A 2014 *Fano Resonances in the Time Domain - understanding and controlling the absorption and emission* (PhD Thesis Heidelberg University)

[84] Blättermann A 2016 *Impulsive control of the atomic dipole response in the time and frequency domain* (PhD Thesis Heidelberg University)

[85] Stooß V, Hartmann M, Birk P, Borisova G D, Ding T, Blättermann A, Ott C and Pfeifer T 2019 XUV-beamline for attosecond transient absorption

measurements featuring a broadband common beam-path time-delay unit and in situ reference spectrometer for high stability and sensitivity *Rev. Sci. Instrum.* **90** 053108

[86] Strickland D and Mourou G 1985 Compression of amplified chirped optical pulses *Opt. Commun.* **56** 219–21

[87] Nobel Media AB 2020 The Nobel Prize in Physics 2018

[88] Fuji T, Rauschenberger J, Apolonski A, Yakovlev V S, Tempea G, Udem T, Gohle C, Hänsch T W, Lehnert W, Scherer M and Krausz F 2005 Monolithic carrier-envelope phase-stabilization scheme *Opt. Lett.* **30** 332

[89] Lücking F, Assion A, Apolonski A, Krausz F and Steinmeyer G 2012 Long-term carrier-envelope-phase-stable few-cycle pulses by use of the feed-forward method *Opt. Lett.* **37** 2076

[90] McClung F J and Hellwarth R W 1962 Giant Optical Pulsations from Ruby *J. Appl. Phys.* **33** 828–9

[91] L'Huillier A, Balcou P, Candel S, Schafer K J and Kulander K C 1992 Calculations of high-order harmonic-generation processes in xenon at 1064 nm *Phys. Rev. A* **46** 2778–90

[92] Macklin J J, Kmetec J D and Gordon C L 1993 High-order harmonic generation using intense femtosecond pulses *Phys. Rev. Lett.* **70** 766–9

[93] Zheltikov A M 2002 Ultrashort light pulses in hollow waveguides *Physics-Uspekhi* **45** 687

[94] Chung J, Member S and Weiner A M 2001 Ambiguity of Ultrashort Pulse Shapes Retrieved From the Intensity Autocorrelation and the Power Spectrum **7** 656–66

[95] Kane D J and Trebino R 1993 Characterization of arbitrary femtosecond pulses using frequency-resolved optical gating *IEEE J. Quantum Electron.* **29** 571–9

[96] Iaconis C and Walmsley I A 1998 Spectral phase interferometry for direct electric-field reconstruction of ultrashort optical pulses *Opt. Lett.* **23** 792

[97] Miranda M, Fordell T, Arnold C, L'Huillier A and Crespo H 2012 Simultaneous compression and characterization of ultrashort laser pulses using chirped mirrors and glass wedges *Opt. Express* **20** 688

[98] Miranda M, Arnold C L, Fordell T, Silva F, Alonso B, Weigand R, L'Huillier A and Crespo H 2012 Characterization of broadband few-cycle laser pulses with the d-scan technique *Opt. Express* **20** 18732

[99] Hartmann M D 2016 *Characterization of Few-Cycle Laser Pulses* (Master Thesis Heidelberg University)

[100] Nelder J A and Mead R 1965 A Simplex Method for Function Minimization *Comput. J.* **7** 308–13

[101] Gao F and Han L 2012 Implementing the Nelder-Mead simplex algorithm with adaptive parameters *Comput. Optim. Appl.* **51** 259–77

[102] Silva F, Alonso B, Holgado W, Romero R, Román J S, Jarque E C, Koop H, Pervak V, Crespo H and Sola Í J 2018 Strategies for achieving intense single-

cycle pulses with in-line post-compression setups *Opt. Lett.* **43** 337

[103] Telle H R, Steinmeyer G, Dunlop A E, Stenger J, Sutter D H and Keller U 1999 Carrier-envelope offset phase control: A novel concept for absolute optical frequency measurement and ultrashort pulse generation *Appl. Phys. B* **69** 327–32

[104] Jones, Diddams, Ranka, Stentz, Windeler, Hall and Cundiff 2000 Carrier-envelope phase control of femtosecond mode-locked lasers and direct optical frequency synthesis *Science* **288** 635–40

[105] Kremer M, Hofrichter C, Fischer B, Sharma V, Camus N, Pfeifer T, Moshammer R and Ullrich J 2011 Minimizing dispersive distortions in carrier-envelope phase sweeping with glass wedges *Opt. Lett.* **36** 1455

[106] https://henke.lbl.gov/optical_constants/filter2.html

[107] French R H, Rodríguez-Parada J M, Yang M K, Derryberry R A and Pfeiffenberger N T 2011 Optical properties of polymeric materials for concentrator photovoltaic systems *Sol. Energy Mater. Sol. Cells* **95** 2077–86

[108] Corkum P B, Burnett N H and Ivanov M Y 1994 Subfemtosecond pulses *Opt. Lett.* **19** 1870

[109] Azoury D, Kneller O, Krüger M, Bruner B D, Cohen O, Mairesse Y and Dudovich N 2019 Interferometric attosecond lock-in measurement of extreme-ultraviolet circular dichroism *Nat. Photonics* **13** 198–204

[110] Heldt T V 2020 *Strong-Field-Driven Electron Dynamics near an Ionization Threshold* (Master Thesis Heidelberg University)

[111] Wood W M, Siders C W and Downer M C 1991 Measurement of femtosecond ionization dynamics of atmospheric density gases by spectral blueshifting *Phys. Rev. Lett.* **67** 3523–6

[112] Rae S C and Burnett K 1992 Detailed simulations of plasma-induced spectral blueshifting *Phys. Rev. A* **46** 1084–90

[113] Kaap F 2018 *Plasma-induzierte Blauverschiebung während der Erzeugung Hoher Harmonischer* (Bachelor Thesis Heidleberg University)

[114] Drescher L, Kornilov O, Witting T, Reitsma G, Monserud N, Rouzée A, Mikosch J, Vrakking M J J and Schütte B 2018 Extreme-ultraviolet refractive optics *Nature* **564** 91–4

[115] W.L. Wiese, M.W. Smith B M G 1966 *Atomic Transition Probailities: Hydogen Through Neon* (National Bureau of Standards)

[116] Samson J A R and Stolte W C 2002 Precision measurements of the total photoionization cross-sections of He, Ne, Ar, Kr, and Xe *J. Electron Spectros. Relat. Phenomena* **123** 265–76

[117] Sorensen S L, Åberg T, Tulkki J, Rachlew-Källne E, Sundström G and Kirm M 1994 Argon 3 s autoionization resonances *Phys. Rev. A* **50** 1218–30

[118] Hartmann M, Stooß V, Birk P, Borisova G, Ott C and Pfeifer T 2019 Attosecond precision in delay measurements using transient absorption spectroscopy *Opt. Lett.* **44** 4749

[119] Blättermann A, Ott C, Kaldun A, Ding T, Stooß V, Laux M, Rebholz M and

Pfeifer T 2015 In situ characterization of few-cycle laser pulses in transient absorption spectroscopy *Opt. Lett.* **40** 3464

[120] Itatani J, Quéré F, Yudin G L, Ivanov M Y, Krausz F and Corkum P B 2002 Attosecond Streak Camera *Phys. Rev. Lett.* **88** 173903

[121] Mairesse Y and Quéré F 2005 Frequency-resolved optical gating for complete reconstruction of attosecond bursts *Phys. Rev. A* **71** 011401

[122] Ullrich J, Moshammer R, Dorn A, Dörner R, Schmidt L P H and Schmidt-B cking H 2003 Recoil-ion and electron momentum spectroscopy: reaction-microscopes *Reports Prog. Phys.* **66** 1463–545

[123] Swoboda M, Fordell T, Klünder K, Dahlström J M, Miranda M, Buth C, Schafer K J, Mauritsson J, L'Huillier A and Gisselbrecht M 2010 Phase Measurement of Resonant Two-Photon Ionization in Helium *Phys. Rev. Lett.* **104** 103003

[124] Ranitovic P, Tong X M, Hogle C W, Zhou X, Liu Y, Toshima N, Murnane M M and Kapteyn H C 2011 Controlling the XUV Transparency of Helium Using Two-Pathway Quantum Interference *Phys. Rev. Lett.* **106** 193008

[125] Shivaram N, Timmers H, Tong X-M and Sandhu A 2012 Attosecond-Resolved Evolution of a Laser-Dressed Helium Atom: Interfering Excitation Paths and Quantum Phases *Phys. Rev. Lett.* **108** 193002

[126] Muller H G 2002 Reconstruction of attosecond harmonic beating by interference of two-photon transitions *Appl. Phys. B* **74** 17–21

[127] Schultze M, Fiess M, Karpowicz N, Gagnon J, Korbman M, Hofstetter M, Neppl S, Cavalieri A L, Komninos Y, Mercouris T, Nicolaides C A, Pazourek R, Nagele S, Feist J, Burgdörfer J, Azzeer A M, Ernstorfer R, Kienberger R, Kleineberg U, Goulielmakis E, Krausz F and Yakovlev V S 2010 Delay in photoemission. *Science* **328** 1658–62

[128] Klünder K, Dahlström J M, Gisselbrecht M, Fordell T, Swoboda M, Guénot D, Johnsson P, Caillat J, Mauritsson J, Maquet A, Taïeb R and L'Huillier A 2011 Probing Single-Photon Ionization on the Attosecond Time Scale *Phys. Rev. Lett.* **106** 143002

[129] Kheifets A S, Bray A W and Bray I 2016 Attosecond Time Delay in Photoemission and Electron Scattering near Threshold *Phys. Rev. Lett.* **117** 143202

[130] Blaga C I, Catoire F, Colosimo P, Paulus G G, Muller H G, Agostini P and DiMauro L F 2009 Strong-field photoionization revisited *Nat. Phys.* **5** 335–8

[131] Haessler S, Fabre B, Higuet J, Caillat J, Ruchon T, Breger P, Carré B, Constant E, Maquet A, Mével E, Salières P, Taïeb R and Mairesse Y 2009 Phase-resolved attosecond near-threshold photoionization of molecular nitrogen *Phys. Rev. A* **80** 011404

[132] Mauritsson J, Remetter T, Swoboda M, Klünder K, L'Huillier A, Schafer K J, Ghafur O, Kelkensberg F, Siu W, Johnsson P, Vrakking M J J, Znakovskaya I, Uphues T, Zherebtsov S, Kling M F, Lépine F, Benedetti E, Ferrari F, Sansone G and Nisoli M 2010 Attosecond Electron Spectroscopy Using a Novel Interferometric Pump-Probe Technique *Phys. Rev. Lett.* **105** 053001

[133] Lucchini M, Ludwig A, Zimmermann T, Kasmi L, Herrmann J, Scrinzi A, Landsman A S, Gallmann L and Keller U 2015 Anisotropic emission in quantum-beat spectroscopy of helium excited states *Phys. Rev. A* **91** 063406

[134] Pazourek R, Reduzzi M, Carpeggiani P A, Sansone G, Gaarde M and Schafer K 2016 Ionization delays in few-cycle-pulse multiphoton quantum-beat spectroscopy in helium *Phys. Rev. A* **93** 023420

[135] Kazansky A K, Bozhevolnov A V., Sazhina I P and Kabachnik N M 2014 Attosecond near-threshold photoionization in a strong laser field *Phys. Rev. A* **90** 033409

[136] Azoury D, Krüger M, Orenstein G, Larsson H R, Bauch S, Bruner B D and Dudovich N 2017 Self-probing spectroscopy of XUV photo-ionization dynamics in atoms subjected to a strong-field environment *Nat. Commun.* **8** 1453

[137] Dahlström J M, Pabst S and Lindroth E 2017 Attosecond transient absorption of a bound wave packet coupled to a smooth continuum *J. Opt.* **19** 114004

[138] Chini M, Wang X, Cheng Y, Wu Y, Zhao D, Telnov D a, Chu S-I and Chang Z 2013 Sub-cycle Oscillations in Virtual States Brought to Light *Sci. Rep.* **3** 1105

[139] Chen S, Wu M, Gaarde M B and Schafer K J 2013 Quantum interference in attosecond transient absorption of laser-dressed helium atoms *Phys. Rev. A* **87** 033408

[140] Lucchini M, Herrmann J, Ludwig A, Locher R, Sabbar M, Gallmann L and Keller U 2013 Role of electron wavepacket interference in the optical response of helium atoms *New J. Phys.* **15** 103010

[141] Wu M, Chen S, Camp S, Schafer K J and Gaarde M B 2016 Theory of strong-field attosecond transient absorption *J. Phys. B At. Mol. Opt. Phys.* **49** 062003

[142] Feit M ., Fleck J . and Steiger A 1982 Solution of the Schrödinger equation by a spectral method *J. Comput. Phys.* **47** 412–33

[143] Hilborn R C 1982 Einstein coefficients, cross sections, f values, dipole moments, and all that *Am. J. Phys.* **50** 982–6

[144] Sciences P 1956 Measurements of lifetimes of excited states of helium atoms *Proc. R. Soc. London. Ser. A. Math. Phys. Sci.* **234** 565–83

[145] Stobbe M 1930 Zur Quantenmechanik photoelektrischer Prozesse *Ann. Phys.* **399** 661–715

[146] Hill R 2006 Hydrogenic Wave Functions *Springer Handbook of Atomic, Molecular, and Optical Physics* (Springer) pp 153–71

[147] Su Q and Eberly J H 1991 Model atom for multiphoton physics *Phys. Rev. A* **44** 5997–6008

[148] Ossiander M, Siegrist F, Shirvanyan V, Pazourek R, Sommer A, Latka T, Guggenmos A, Nagele S, Feist J, Burgdörfer J, Kienberger R and Schultze M 2017 Attosecond correlation dynamics *Nat. Phys.* **13** 280–5

[149] Isinger M, Squibb R J, Busto D, Zhong S, Harth A, Kroon D, Nandi S, Arnold C L, Miranda M, Dahlström J M, Lindroth E, Feifel R, Gisselbrecht M and

L'Huillier A 2017 Photoionization in the time and frequency domain. *Science* **358** 893–6

[150] Nicolaides C A, Mercouris T and Komninos Y 2002 Attosecond dynamics of electron correlation in doubly excited atomic states *J. Phys. B At. Mol. Opt. Phys.* **35** L271–9

[151] Mercouris T, Komninos Y and Nicolaides C A 2004 Theory and computation of the attosecond dynamics of pairs of electrons excited by high-frequency short light pulses *Phys. Rev. A* **69** 032502

[152] Wickenhauser M, Burgdörfer J, Krausz F and Drescher M 2005 Time Resolved Fano Resonances *Phys. Rev. Lett.* **94** 023002

[153] Mercouris T, Komninos Y and Nicolaides C A 2007 Time-dependent formation of the profile of the He 2s2p Po1 state excited by a short laser pulse *Phys. Rev. A - At. Mol. Opt. Phys.* **75** 013407

[154] Chu W C and Lin C D 2010 Theory of ultrafast autoionization dynamics of Fano resonances *Phys. Rev. A - At. Mol. Opt. Phys.* **82** 53415

[155] Argenti L and Lindroth E 2010 Ionization branching ratio control with a resonance attosecond clock *Phys. Rev. Lett.* **105** 53002

[156] Gruson V, Barreau L, Jiménez-Galan Á, Risoud F, Caillat J, Maquet A, Carré B, Lepetit F, Hergott J-F, Ruchon T, Argenti L, Taïeb R, Martín F and Salières P 2016 Attosecond dynamics through a Fano resonance: Monitoring the birth of a photoelectron. *Science* **354** 734–8

[157] Ammosov M V., Delone N B and Krainov V P 1986 Tunnel Ionization Of Complex Atoms And Atomic Ions In Electromagnetic Field *Sov. Phys. Jetp* **64** 1191

[158] Lambropoulos P, Maragakis P and Zhang J 1998 Two-electron atoms in strong fields *Phys. Rep.* **305** 203–93

[159] Artemyev A N, Cederbaum L S and Demekhin P V. 2017 Impact of two-electron dynamics and correlations on high-order-harmonic generation in He *Phys. Rev. A* **95** 033402

[160] Jiang W-C, Chen S-G, Peng L-Y and Burgdörfer J 2020 Two-Electron Interference in Strong-Field Ionization of He by a Short Intense Extreme Ultraviolet Laser Pulse *Phys. Rev. Lett.* **124** 043203

[161] Borisova G D, Stooß V, Dingeldey A, Kaldun A, Ding T, Birk P, Hartmann M, Heldt T, Ott C and Pfeifer T 2020 Strong-field-induced single and double ionization dynamics from single and double excitations in a two-electron atom *J. Phys. Commun.* **4** 055012

[162] Schultze M, Ramasesha K, Pemmaraju C D, Sato S A, Whitmore D, Gandman A, Prell J S, Borja L J, Prendergast D, Yabana K, Neumark D M and Leone S R 2014 Attosecond band-gap dynamics in silicon. *Science* **346** 1348–52

Acknowledgments

Ich möchte allen aus der Gruppe für die netten, lustigen, lehrreichen und immer wieder unterhaltsamen Stunden, Tag, Wochen, Monate und Jahre während dieser Dissertation danken. Ein besonderer Dank geht an…

Prof. Dr. Thomas Pfeifer, der mir die Möglichkeit für diese Arbeit gegeben hat. Danke für Deine begeisternde, faszinierende Art über Physik zu reden. Danke, dass man bei jedem Gespräch mit Dir etwas lernen kann.

Prof. Dr. Selim Jochim, der sich freundlicherweise dazu bereit erklärt hat, diese Dissertation als Zweitgutachter zu betreuen.

Dr. Christian Ott, der sich für die vielen tiefgreifenden Erklärungen, Gespräche, und Hilfestellungen während dieser Arbeit immer viel Zeit genommen hat. Ich konnte wahnsinnig viel mitnehmen von Deinen Ratschlägen.

Prof. Dr. Klaus Bartschat, der mich mit theoretischem Wissen unterstützt und mir die Formel für das heuristische Heliumion-Potential mitsamt den Eigenenergien und Dipolmomenten zur Verfügung gestellt hat.

Dr. Veit Stooß, für die viele Zeit im Labor, im Büro und für Dein „Hä“ wenn mal etwas nicht so läuft wie Du denkst. Ich schätze Dich sehr.

Maximilian Hartmann, für die gemeinsame schöne Zeit privat als Freunde und auf der Arbeit in der gemeinsamen Arbeitsgruppe. Danke für Deinen fortwährenden Einsatz, wenn es darum geht, Optiken aufzubauen, Optiken abzureißen, Messungen zu machen, Labore umzuziehen, und über Leute zu lästern.

Gergana D. Borisova, für die vielen (kurzen) Fragen, das Engagement im Labor und am Kickertisch. Danke für Deinen extrem kritischen Blick auf die Texte und Bilder, die man im Laufe seiner eigenen Arbeit schreibt und erstellt.

Dr. Alexander Blättermann, für seinen atemberaubenden Charme und seine erhabene Präsens. Du bleibst in Erinnerung.

Dr. Martin Laux, für die vielen lustigen Unterhaltungen die wir miteinander führen konnten.

Dr. Kristina Meyer, die am Anfang meiner Arbeit immer ein offenes Ohr für mich hatte.

Dr. Thomas Ding, für seine „dicke durch“ Art. Danke, dass Du immer aussprichst was Du denkst und für die Bandentore in der Verteidigung am Kickertisch.

Marc Rebholz, für die Ruhe, den Kaffee und den exzellenten Geschmack.

Fabian Kaap, für seine lustige Art. Ich habe sehr gerne mit Dir gearbeitet.

Arso Ivanovic, für seine Eloquenz und die zeitlosen Sprüche.

Sabine Rockenstein, für ihr Anschleichen am Bürotisch und im Labor. Dadurch bin ich aufmerksamer geworden.

Tobias Heldt, für seine Art auf die Dinge genau hinzusehen. Es hat mir viel Spaß gemacht mit Dir über Physik zu diskutieren.

die Kollegen: Shuyuan Hu, Carina da Costa Castanheira, Lennart Aufleger, Patrick Ruprecht und Alexander Magunia für die entspannte Atmosphäre mit Euch und die guten Gespräche.

Nikola Mollov und **Alexander von der Dellen,** für die technische Unterstützung am Laser und im Labor.

Philipp Gernandt und **Janko Nauta** für das teilweise Korrekturlesen dieser Arbeit.

Einen besonderen Dank geht an:

Lenja Birk, für ihre begeisternde Art, die mich sehr oft motiviert. Danke für Deine niedliche Ausdrucksweise.

Juna Birk, für Deine Art wenn Du etwas haben möchtest und dass Du nach dem Frühstück, Mittagessen und Abendessen immer mit mir tanzen möchtest.

Und einen ganz speziellen Dank an meine Frau **Judith**, Du bist die Beste. Wenn ich daran denke, was wir in dieser Zeit der Doktorarbeit alles geschafft haben. Danke, dass ich glücklich bin wenn ich nach Hause komme. Danke, dass Du bei mir bist und ich Dich lieben darf.